InAs/GaAs Quantum-Dot Light Emitting Sources Monolithically Grown on Silicon Substrates

Mingchu Tang

A thesis submitted to University College London for the degree of
Doctor of Philosophy (PhD)

Department of Electronic & Electrical Engineering
University College London

July 2016

Declaration

I, Mingchu Tang, confirm that the work presented in this thesis in my own. Where information has been derived from other sources, I confirm that it has been indicated in the thesis.

Abstract

Si-based light emitting sources are highly demanded for applications in optoelectronic integration circuits. Unfortunately, Si has an indirect bandgap and thus a low efficiency in photon emission. On the other hand, III–V semiconductors have superior optical properties and are considered as strong candidates to achieve efficient light emitting sources on Si platforms via wafer bonding or monolithically epitaxy growth. III–V materials monolithically grown on Si substrate could introduce various types of defects including antiphase domain, threading dislocation, misfit dislocation. These defects must be dealt with satisfactorily in order to fulfill the potential of III–V/Si integration. In this thesis, buffer layers for InAs/GaAs quantum dots (QDs) monolithically grown Si substrate have been investigated. The buffer layer study is mainly focused on the different types of defect filter layers (DFLs). The measurements of atomic force microscopy, photoluminescence and transmission electron microscopy are carried out to investigate the effectiveness of each type of DFLs. The results of lasers and superluminescent diodes (SLDs) have been presented based on the studies of DFLs.

In order to improve the performance of InAs/GaAs QDs grown on Si substrates, a GaAs buffer layer and DFLs have been used to reduce the defect density from ~10^{10} to 10^{6} cm^{-2} after three sets of DFLs, which consists of strained layer superlattices (SLSs). In the thesis, the optimisation of DFLs has been carried out. Different types of DFLs are investigated in the Chapter 3, including InAs/GaAs QDs, InGaAs submonolayer QDs, InGaAs/GaAs SLSs and InAlAs/GaAs SLSs. DFLs made of InAlAs/GaAs SLSs show the strongest performance, based on the measurements of atomic force microscopy, photoluminescence and transmission electron microscopy. The high performance InAs/GaAs QDs lasers with low threshold current density (194 A/cm^2) and high operating temperature (85˚C) has been obtained for the samples with optimised DFLs.

In addition to III–V/Si lasers, III–V SLDs monolithically grown on silicon substrates would further enrich the silicon photonics toolbox, enabling low-cost, highly scalable, high-functional, and streamlined on-chip light sources. In this thesis, the first InAs/GaAs QD SLDs monolithically grown on a Si substrate have been demonstrated based on the similar growth structure of laser devices. The fabricated two-section InAs/GaAs QD SLD produces a close-

to-Gaussian emission spectrum of 114 nm centred at ~1255 nm wavelength, with a maximum output power of 2.6 mW at room temperature.

The optimisation of InGaAs/GaAs SLSs DFLs has been carried out in the Chapter 5. The optimisation includes introducing different growth methods into GaAs spacer layer between each set of DFL, indium composition and GaAs thickness in InGaAs/GaAs SLSs. The optimisation is examined by atomic force microscopy, photoluminescence and transmission electron microscopy. The laser device with optimised InGaAs/GaAs SLSs DFLs has a lower threshold current density, higher operating temperature and characteristic temperature.

In conclusion, InAs/GaAs QDs lasers with low threshold current density and the first QDs SLDs monolithically grown on Si substrates have been demonstrated. InAlAs/GaAs SLSs DFLs have been proved that as considerable solution to reduce the threading dislocation density significantly. The optimisations of InGaAs/GaAs SLSs DFLs successfully improve the QDs laser performance which could also be used in III–V/Si monolithically integration. The III–V QDs lasers and SLDs monolithically grown on Si substrate are essential steps for Si photonics integration, which will fill the “holy grail” of opto-electronic integration circuits.

Acknowledgment

I would like to thank to my supervisor Professor Huiyun Liu for his support on my study and work. He gave me the excellent opportunity to work with our molecular beam epitaxy system. I also want to thank my second supervisor, Professor Karl Woodbridge, with his support.

I would like to express my gratitude towards my families, my parents Mr Yukuan Tang and Mrs Shuxian Liu, and my wife Tianyao Zhang. Without their understanding and support, I could not focus on my research. I really appreciate their encouragement when I feel depressed about my research.

I would like to give special thanks to my colleagues and former colleagues, Dr. Jiang Wu, Dr. Peter Carrington, Dr. Siming Chen, Dr. Sabina Hatch, Dr. Qi Jiang, Miss Pamela Jurczak, Mr Dongyoung Kim, Mr Winson Phu Lam, Dr. Andrew Lee, Mr Kevin Lee, Miss Mengya Liao, Mr Arthur Onno, Mr Hota Tei, Dr. Ting Wang, Dr. Frank Tutu, Mr Hao Xu, Dr. Yunyan Zhang, and Dr. Steve Hudziak. Thanks for their help during my research. Especially, Jiang, Qi and Siming guided me on the MBE growth and semiconductor processing, Steve trained me how to use the atomic force microscopy, and Ting, Andrew, Qi, Siming and Jiang taught me how to use the PL and EL characteristic measurement system. I would like to express my gratitude to Dr. Richard Beanland from University of Warwick, Dr. Vitaliy G Dorogan, Dr. Mourad Benamara, Dr. Yuriy I Mazur, and Dr. Gregory J Salamo from University of Arkansas for the help with TEM measurements.

Publications

Thesis Related Publications

1. Mingchu Tang, Siming Chen, Jiang Wu, Qi Jiang, Vitaliy G Dorogan, Mourad Benamara, Yuriy I Mazur, Gregory J Salamo, Alwyn Seeds, Huiyun Liu, "1.3-μm InAs/GaAs quantum-dot lasers monolithically grown on Si substrates using InAlAs/GaAs defect filter layers", *Optics Express* vol. 22, no. 10, pp. 11528-11535, 2014
2. M Tang, S Chen, Q Jiang, J Wu, VG Dorogan, M Benamara, YI Mazur, Gregory J Salamo, Alwyn Seeds, "Huiyun Liu, InAs/GaAs quantum-dot superluminescent light-emitting diode monolithically grown on a Si substrate", *ACS Photonics*, vol. 1, no. 7, 638-642, 2014
3. M Tang, S Chen, J Wu, Q Jiang, D Kim, A Seeds, H Liu, "Optimisation of 1.3-μm InAs/GaAs Quantum-Dot Lasers Monolithically Grown on Si Substrates", *Journal of Physics: Conference Series*, vol. 619, no. 1, pp. 012011, 2015
4. Mingchu Tang, Jiang Wu, Siming Chen, Qi Jiang, Alwyn J. Seeds, Huiyun Liu, Vitaliy G. Dorogan, Mourad Benamara, Yuriy Mazur, and Gregory Salamo. "Optimisation of the defect filter layers in 1.3-μm InAs/GaAs quantum-dot lasers monolithically grown on Si substrates." *IET Optoelectronics*, vol. 9, no. 2, pp. 61-64, 2015
5. Mingchu Tang, Siming Chen, iang Wu, Qi Jiang, Ken, Kennedy, Pamela Jurczak, Mengya Liao, Richard Beanland, Alwyn Seeds and Huiyun Liu, "Optimizations of Defect Filter Layers for 1.3-μm InAs/GaAs Quantum-Dot Lasers Monolithically Grown on Si substrates", *IEEE Journal of Selected Topics in Quantum Electronics*, Just Accpeted.
6. A Lee, Q Jiang, M Tang, A Seeds, H Liu, "Continuous-wave InAs/GaAs quantum-dot laser diodes monolithically grown on Si substrate with low threshold current densities" *Optics express*, vol. 20, no. 20, pp. 22181-22187, 2012
7. A Lee, Q Jiang, M Tang, Y Zhang, A Seeds, H Liu, "InAs/GaAs quantum-dot lasers monolithically grown on si, ge, and ge-on-si substrates", *IEEE Journal of Selected Topics in Quantum Electronics*, vol. 19, no. 4, pp. 1901107-1901107, 2013
8. Siming Chen, Mingchu Tang, Jiang Wu, Qi Jiang, Vitaliy Dorogan, Mourad Benamara, Yuriy I. Mazur, Gregory J. Salamo, and Huiyun Liu. "Long-wavelength InAs/GaAs quantum-dot light emitting sources monolithically grown on Si substrate." *In Photonics*, vol. 2, no. 2, pp. 646-658, 2015.
9. Jonathan R. Orchard, Samuel Shutts, Angela Sobiesierski, Jiang Wu, Mingchu Tang, Siming Chen, Qi Jiang, Stella Elliott, Richard Beanland, Huiyun Liu, Peter M. Smowton, and David J. Mowbray, "In situ annealing enhancement of the optical properties and laser

device performance of InAs quantum dots grown on Si substrates." *Optics Express*, vol. 24, no. 6, pp. 6196-6202, 2016

10. M. Liao, S. Chen, M. Tang, J. Wu, Q. Jiang, A. Seeds, and H. Liu. "InAs/GaAs quantum-dot light emitters monolithically grown on Si substrate." *In SPIE OPTO*, pp. 975803-975803. International Society for Optics and Photonics, 2016.
11. Siming Chen, Wei Li, Jiang Wu, Qi Jiang, Mingchu Tang, Samuel Shutts, Stella N. Elliott Angela Sobiesierski, Alwyn J. Seeds, Ian Ross, Peter M. Smowton and Huiyun Liu "Electrically pumped continuous-wave III–V quantum dot lasers on silicon." *Nature Photonics*, doi:10.1038/nphoton.2016.21, 2016
12. Wu, Jiang, Andrew Lee, Qi Jiang, Mingchu Tang, Alwyn J. Seeds, and Huiyun Liu. "Electrically pumped continuous-wave 1.3-μm InAs/GaAs quantum dot lasers monolithically grown on Si substrates." *IET Optoelectronics*, vol. 8, no. 2, pp. 20-24. 2014
13. SM Chen, MC Tang, J Wu, Q Jiang, VG Dorogan, M Benamara, YI Mazur, GJ Salamo, AJ Seeds, H Liu, "1.3 μm InAs/GaAs quantum-dot laser monolithically grown on Si substrates operating over 100 C", *Electronics Letters*, vol. 50, no. 20, pp. 1467-1468, 2014

Other Publications

14. FK Tutu, J Wu, P Lam, M Tang, N Miyashita, Y Okada, J Wilson, R Allison, H Liu, "Antimony mediated growth of high-density InAs quantum dots for photovoltaic cells", *Applied Physics Letters*, vol. 103, no. 4, pp. 043901, 2013
15. Y Zhang, J Wu, M Aagesen, J Holm, S Hatch, M Tang, S Huo, H Liu, "Self-Catalyzed Ternary Core–Shell GaAsP Nanowire Arrays Grown on Patterned Si Substrates by Molecular Beam Epitaxy", *Nano letters*, vol. 14, no. 8, pp. 4542-4547, 2014
16. Jiang Wu, Yanbo Li, Jun Kubota, Kazunari Domen, Martin Aagesen, Thomas Ward, Ana Sanchez, Richard Beanland, Yunyan Zhang, Mingchu Tang, Sabina Hatch, Alwyn Seeds, Huiyun Liu, Wafer-Scale Fabrication of Self-Catalyzed 1.7 eV GaAsP Core–Shell Nanowire Photocathode on Silicon Substrates, *Nano letters*, vol. 14, no. 4, pp. 2013-2018, 2014
17. P Lam, S Hatch, J Wu, M Tang, VG Dorogan, YI Mazur, Gregory J Salamo, Iñigo Ramiro, Alwyn Seeds, Huiyun Liu, "Voltage recovery in charged InAs/GaAs quantum dot solar cells", *Nano Energy*, vol. 6, 159-166, 2014
18. S Hatch, J Wu, K Sablon, P Lam, M Tang, Q Jiang, H Liu, "InAs/GaAsSb quantum dot solar cells", *Optics Express*, vol. 22, no. S3, A679-A685, 2014

19. Q Jiang, M Tang, S Chen, J Wu, A Seeds, H Liu, "InAs/GaAs quantum-dot superluminescent diodes monolithically grown on a Ge substrate", *Optics Express*, vol. 22, no. 19, pp. 23242-23248, 2014
20. T Ward, AM Sánchez, M Tang, J Wu, H Liu, DJ Dunstan, R Beanland, "Design rules for defect filters", *Journal of Applied Physics*, vol. 116, no.6, pp. 063508, 2014
21. P Lam, J Wu, M Tang, Q Jiang, S Hatch, R Beanland, J Wilson, R Allison, H. Liu, "Submonolayer InGaAs/GaAs quantum dot solar cells", *Solar Energy Materials and Solar Cells*, vol. 126, pp. 83-87, 2014
22. PM Lam, J Wu, S Hatch, D Kim, M Tang, H Liu, J Wilson, R Allison, Effect of rapid thermal annealing on InAs/GaAs quantum dot solar cells, *IET Optoelectronics*, vol. 9, no. 2, pp. 65-68, 2015
23. I George, F Becagli, HY Liu, J Wu, M Tang, R Beanland, "Defect filters in GaAs on Si", *Semiconductor Science and Technology*, vol. 30 no. 11, pp. 114004, 2015
24. P. Lam, J. Wu, M. Tang, D. Kim, S. Hatch, I. Ramiro, V. G. Dorogan *et al*. "InAs/InGaP quantum dot solar cells with an AlGaAs interlayer." *Solar Energy Materials and Solar Cells*, vol. 144, pp. 96-101, 2016
25. Arthur Onno ; Jiang Wu ; Qi Jiang ; Siming Chen ; Mingchu Tang ; Yurii Maidaniuk ; Mourad Benamara ; Yuriy I. Mazur ; Gregory J. Salamo ; Nils-Peter Harder ; Lars Oberbeck ; Huiyin Liu, "1.7 eV Al0. 2Ga0. 8As solar cells epitaxially grown on silicon by SSMBE using a superlattice and dislocation filters." *In SPIE OPTO*, pp. 974310-974310. International Society for Optics and Photonics, 2016.
26. Dongyoung Kim, Mingchu Tang, Jiang Wu, Sabina Hatch, Yurii Maidaniuk, Vitaliy Dorogan,Yuriy I. Mazur, Gregory J. Salamo, Huiyun Liu, "Si-doped InAs/GaAs quantum dot solar cell with AlAs cap layers", *IEEE, Journal of Photovoltaics,* Just accepted, 2016

Conferences

1. M Tang, S Chen, Q Jiang, J Wu, A Seeds, H Liu, High Performance of InAs/GaAs Quantum Dot Lasers Monolithically Grown on Si substrate with InAlAs/GaAs Defect filter Layers Introducing, The European Conference on Lasers and Electro-Optics, CB_9_2
2. Q Jiang, A Lee, M Tang, A Seeds, H Liu, Silicon-based long-wavelength III–V quantum-

dot lasers, Indium Phosphide and Related Materials (IPRM), 2012 International Conference on, 2012

3. Jiang Wu, Phu Lam, Yunyan Zhang, Mingchu Tang, Sabina Hatch and Huiyun Liu, III–V Nanostructures Grown by Molecular Beam Epitaxy for High Efficiency Solar Cells, ECS meeting abstract, MA2014-02 2013
4. Q Jiang, A Lee, M Tang, A Seeds, H Liu, Long-wavelength III–V quantum-dot lasers monolithically grown on Si substrates, Nanoelectronics Conference (INEC), 2013 IEEE 5th International, 333-335, 2013
5. A Lee, Q Jiang, T Wang, M Tang, A Seeds, H Liu, III–V Quantum Dot Laser Growth on Silicon and Germanium, Optical Fiber Communication Conference, 2013
6. Chen, S., M. Tang, Junyong Wu, Qimeng Jiang, A. Seeds, H. Liu, V. G. Dorogan, M. Benamara, Y. I. Mazur, and G. J. Salamo. "1.3 μm InAs/GaAs quantum-dot laser monolithically grown on Si substrates using InAlAs/GaAs defect filter layers." In Conference Digest-IEEE International Semiconductor Laser Conference, pp. 88-89. 2014.
7. Chen, Siming, Tang, Mingchu, Qi Jiang, Jiang Wu, Vitaliy Dorogan, Mourad Benamara, Yuriy Mazur, Gregory Salamo, Alwyn Seeds, and Huiyun Liu. "Electrically Pumped 1.3-μm InAs/GaAs Quantum Dot Laser Monolithically Grown on Si Substrate Lasing up to 111° C." In CLEO: Science and Innovations, pp. SW3F-1. Optical Society of America, 2015.
8. Qi Jiang, Siming Chen, Mingchu Tang, Jiang Wu, Alywn Seeds, Huiyun Liu, "Monolithically Grown Superluminescent Diodes on Germanium and Silicon substrates", In CLEO: Science and Innovations, pp. SM3G. 6. Optical Society of America, 2015.
9. S Shutts, SN Elliott, PM Smowton, A Sobieserski, J Wu, M Tang, H Liu, R. Beanland, "Continuous-wave emission of III–V quantum dot lasers grown directly on Si substrates", Photonics Conference (IPC), 2015, 595-596
10. A Lee, M Tang, Q Jiang, J Wu, A Seeds, H Liu, "InAs/GaAs quantum-dot lasers and detectors on silicon substrates for silicon photonics", Phys. Lett, vol. 100, no. 052113, 2012

Table of Contents

List of Abbreviation

AFM	Atomic force microscopy
ALD	Atomic layer deposition
APD	Antiphase domain
CAR	Continuous azimuthal rotation
CVD	Chemical vapour deposition
CW	Continuous-wave
DFB	Distributed feedback laser
DFL	Defects filter layer
DH	Double-heterostructure
DoS	Density of states
DWELL	Dot-in-well
EL	Electroluminescence
FB	Fabry-Perot
FWHM	Full width at half maximum
HEMT	High-electron-mobility transistor
IPA	Isopropyl alcohol
LED	Light emitting diode
LN2	Liquid nitrogen
MBE	Molecular beam epitaxy
MEE	Migration enhanced epitaxy
ML	Monolayer
MOCVD	Metal-organic chemical vapour deposition
MOSFET	
OE	Optoelectronic
PID	Proportional-integral-derivative
PL	Photoluminescence
QD	Quantum dot
QW	Quantum well
RGA	Residual gas analyzer
RHEED	Reflection high-energy electron diffraction
RTP	Rapid thermal processing

SLD	Superluminescent light-emitting diode
SLS	Strained-layer supperlattice
S-K	Stranski-Krastanov
SML	Submonolayer
SOI	Silicon-on-insulator
TAE	Thermal activation energies
TEM	Transmission electron microscopy
TD	Threading dislocation
TSP	Titanium sublimation pump
UHV	Ultra-high vacuum
VCSEL	Vertical-cavity-surface-emitting-laser
VLSI	Very-large-scale-integraion
VPE	Vapour phase epitaxy
XRD	X-ray diffraction

List of Figures

List of Symbols

E	Energy
E_a	Thermal activation energy
E_c	Conduction band edge energy
E_g	Bandgap energy
E_v	Valence band edge energy
k_b	Boltzmann's constant
m^*	Effective mass
n	Carriers density
J_{th}	Threshold current density
T	Temperature
T_0	Characteristic temperature
υ	Frequency of light
λ	Wavelength of light in medium of index n
ΔS	Change in entropy associated with the reaction,
ΔH	The entropy of the reaction
h	Plank constant

Chapter 1

Introduction

1.1 Introduction

1.1.1 Si Photonics

The demonstrations of Si microelectronic devices including transistors, amplifiers, modulators have brought an incredible impact to the world for the last 50 years. About 95% of all semiconductor devices are fabricated on Si substrates [1]. Moore's law predicted the number of transistors on a single chip would be doubled every 2 years (or 18 months), which have been right for the last 50 years, as shown in Figure 1.1. However, copper connection is limiting the development of transistor integration on the Si platforms [2]. The major limitation of copper interconnections in the chip-to-chip system is the loss introduced at high frequency. For example, the common copper trace material losses of ~0.15 – 1.5 dB/inch and ~2.0~3.0 dB/inch are incurred at 5 and 12.5 GHz, respectively. Insertion loss, return loss and cross talk all can be significantly enhanced in the higher frequency and the loss is difficult to be coped with due to the electromagnetic interaction between components of circuits [3]. In addition, the lower energy consumption and the higher speed of transmission are the advantages of using optical signals [4]. The Si photonics could provide the driving force in the next stage of intra-chip connection [5, 6] due to the high possibility of compatibility of current CMOS technique and photonics integration circuits on Si platform. Indeed, Si photonics has attracted much attention over the last 30 and extensive support from the industry.

Optoelectronic integration could be a promising solution to overcome the high loss on Si microelectronic circuits with the high speed of photon transmission and low energy consumption in devices. Very-large-scale-integration (VLSI), especially the optoelectronic

(OE-VLSI) technique on Si platform is proposed as a future technique which can be applied in electronic devices. The photonic devices integrated on Si substrates could be operated at different wavelengths, which include emitter, modulator, wave-guide, and detector. The important advantages of the Si platform are the low cost and potentially industrial integration. The strong foundation of Si industry has provided huge motivation to researchers into developing Si photonics.

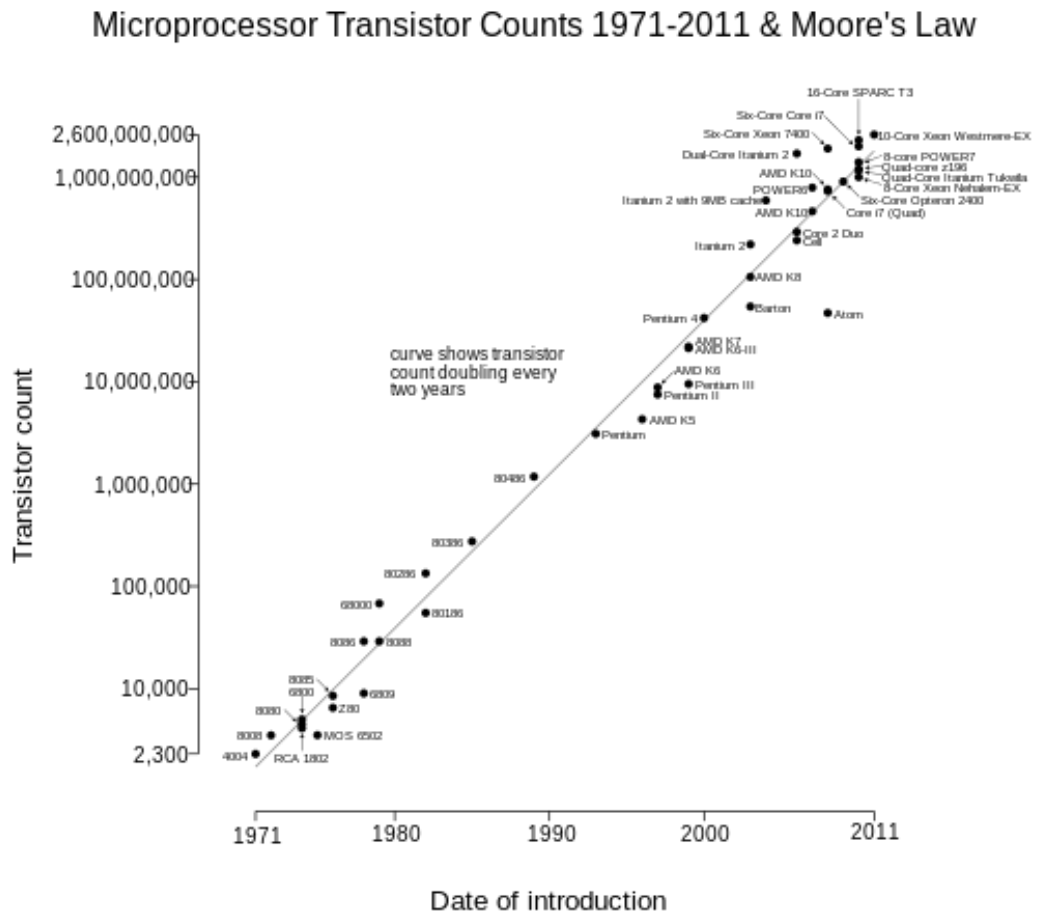

Figure 1.1 Moore's law proves the development of numbers of transistor in unit area [7]. The number of transistor in the microprocessor doubles every 2 years since 1970s.

Not only Si, but also the rest of group IV materials also provide the possibility for OE-VLSI. Ge-Si alloy has direct bandgap and it also can be fabricated as complementary metal–oxide–semiconductor (CMOS). Compound III–V materials also have suitable bandgap and high electron mobility to produce high performance devices including metal–oxide–semiconductor field-effect transistor (MOSFET), CMOS, lasers, amplifiers and detectors. Therefor,

Integration of III–V materials and optoelectronic devices on the silicon platform will bring the advantages of III–V materials to Si platforms.

1.1.2 The Challenges in Si Photonics

The light emitter on silicon is considered as the "holy grail" to Si photonics, due to the indirect bandgap of Si materials. Figure 1.2 presents the energy bandgap of InP and Si bulk material in k-space, which indicates the indirect bandgap property of Si bulk material. In the direct bandgap structure, the electrons recombine with holes and photons emit if the momentum is same between electrons and holes and vice versa. Si bulk material cannot produce photons efficiently due to the high ratio of Auger recombination. However, as a well-established semiconductor material, Si-based light emitting devices are unmissable for Si photonics.

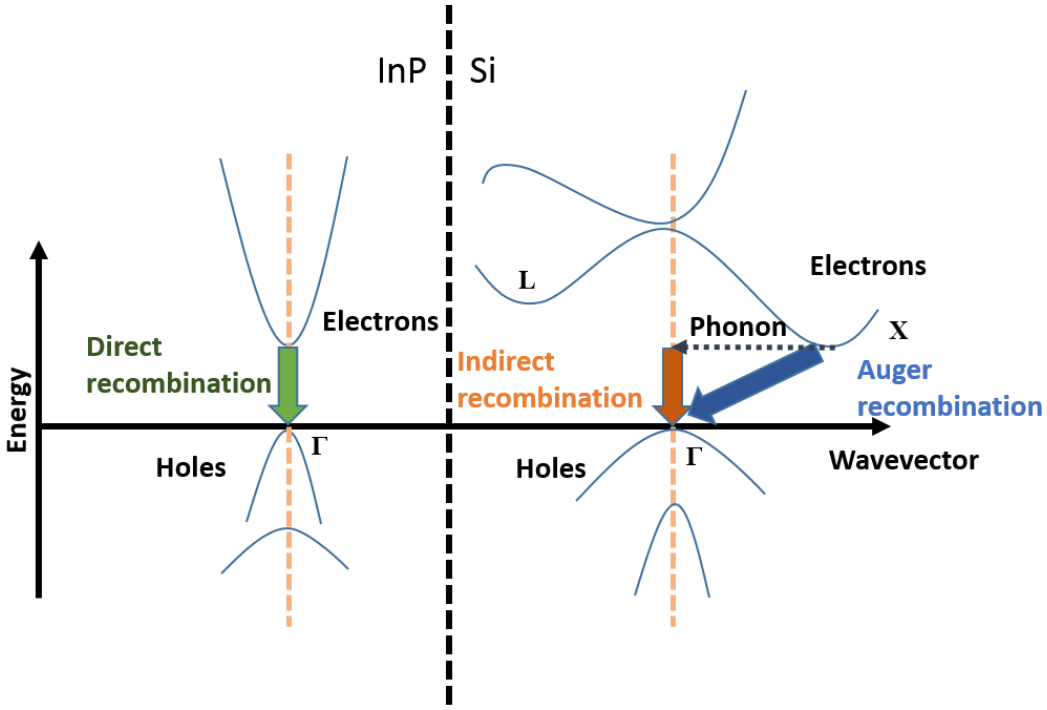

Figure 1.2 K-space energy bandgap structures of InP and Si bulk material with direct and in-direct bandgap. In the Si bulk material, high ratio of Auger recombination is the main issue of low efficiency of photon emitting from Silicon [8].

Until now, Si-based amplifiers, modulators, waveguides, and photodetectors have been well established and some of them are even commercially manufactured. However, high performance on-chip light-emitting devices are still missing in the optoelectronic integrated circuits toolkit. The indirect bandgap of Si and Ge will significantly reduce the radiative recombination, which means the low efficiency of photon emission in Si and Ge bulk material.

One of the solution is to use Ge-Si alloys, which could achieve a direct bandgap due to strain shrinks the bandgap to become direct and a Ge-Si based laser has been reported [9]. In addition, there are also other solutions to the Si-based light emitting sources, including Si Raman lasers, Si hybrid lasers and III–V lasers monolithically grown on Si platforms. The introduction of these approaches and also other types of silicon-based lasers will be presented and discussed later in this chapter.

1.2 Semiconductor Material Properties

1.2.1 Introduction to III–V Semiconductors

The reasons that III–V semiconductor materials are one of the main driving forces of new semiconductor materials are their superior electronic and optical properties. High-electron-mobility transistor (HEMT) [10, 11], high-performance semiconductor light emitters and other electronic and optoelectronic devices have been realised on GaAs, GaSb, InP substrates [12, 13]. Commercial semiconductor lasers, which have been applied in telecommunication, are well established on InP and GaAs substrates. The HEMTs on GaAs [14, 15] and InP [16] substrates also have been widely used in mobile phones. In principle, most of III–V materials have direct energy bandgaps and high carrier mobility, which are attractive to both electronic and optoelectronic devices.

In comparison with III–V materials, II-VI materials are also able to have bandgap spanning over a wide energy range and covers from ultra-violet (ZnS) to mid-infared (HgTe) as shown in Figure 1.4 [17, 18]. However, the highly toxiciy of II-VI materials brings the concerns to the research and application. Moreover, III-V materials provide better light-emitting devices performance on infrared light emitting. The growth methods used for producing of III–V materials include chemical and physical methods. III–V materials can be grown by molecular beam epitaxy (MBE), chemical vapour deposition (CVD) or vapour phase epitaxy (VPE) methods. MBE growth brings high-purity and precise control of materials, however the growth rate is relatively lower than CVD and VPE. The details of MBE growth will be presented in chapter 2.

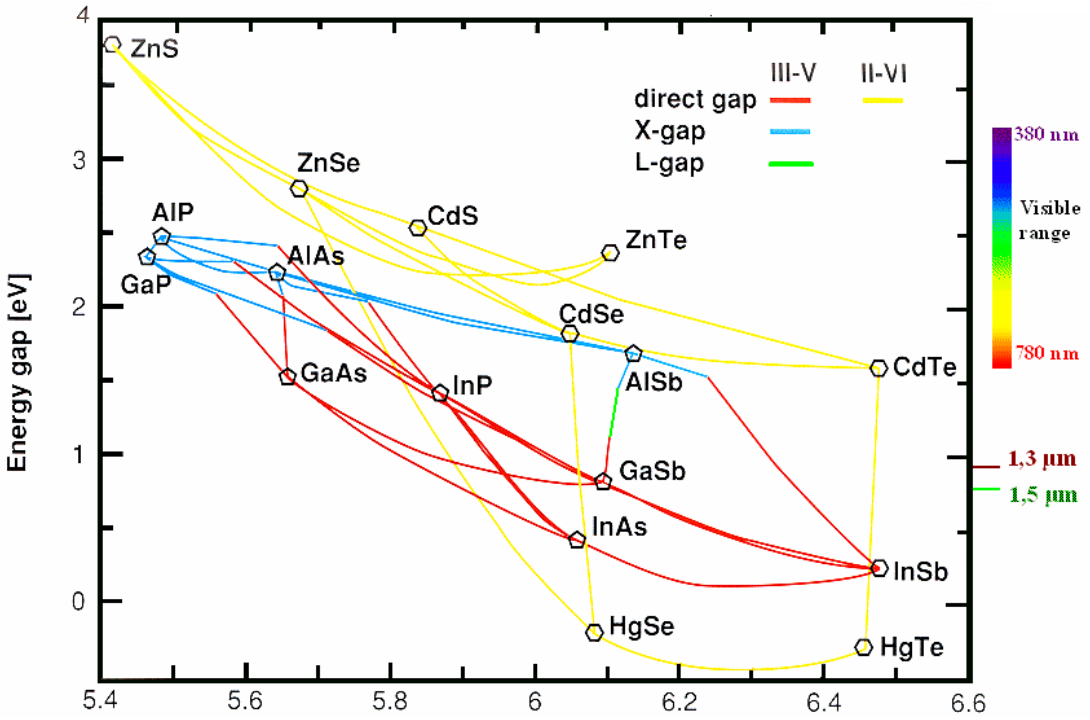

Figure 1.4 Lattice constant (x-axis) with units of nanometre versus energy gap (left) and wavelength (right) of different III–V and II-VI materials [19]. III-V semiconductor compounds have wavelength range from visible to mid-infrared and II-VI materials have longer range from UV to mid-infrared.

The bandgaps and the relations to lattice constants of III–V materials have been introduced in table 1.1 and Figure 1.4, which show that III–V alloys with arsenic allow infrared emission. Arsenic is an excellent material for infrared devices and its epitaxial growth has been well-studied. The 7% lattice mismatch between InAs and GaAs could be used to form InAs/GaAs quantum dots (QDs), which could give emission at 1.3 µm, a silicon absorption window and telecommunication wavelength. Also by introducing the phosphorus and antimony to GaAs, the InAs/GaAs quantum dots could able to emit 1.5 µm by lowering the strain of GaAs and InAs interface [20]. GaAs has been proved as a great buffer material on Si substrate [21]. However, the 4% lattice mismatch of GaAs and Si will introduce dislocations and it can be dealt with dislocation filter layers. The lattice constant of GaP (5.4505 Å) and AlP (5.451 Å) are close to Si (5.431), which makes them suitable candidates for a III-V buffer on Si substrate [22]. InP based opto-electronic devices are well-established for commercial lasera, detectors and optical transceivers working on 1.5 µm wavelength. InSb material is mainly used in mid-infrared application, especially detectors, and its high electron mobility attracts researchers to work on HEMT. GaSb can also be used as III-V buffer on Si substrate [23].

Physical Properties at 300 K/Materials	Si	Ge	GaAs	InAs	GaP	InP	GaSb	AlSb	InSb
Bandgap Energy (eV)	1.12	0.661	1.424	0.354	2.26	1.344	0.726	1.6	0.17
Lattice Constant (A)	5.431	5.658	5.653	6.058	5.4505	5.869	6.096	6.135	6.479
Electron Mobility ($cm^2/V/s$)	1400	3900	8500	40000	250	5400	3000	200	77000
Hole Mobility ($cm^2/V/s$)	450	1900	400	500	150	200	1000	400	850
Melting Point(°C)	1412	937	1240	942	1457	1060	712	1080	527
Thermal Conductivity ($Wcm^{-1}°C^{-1}$)	1.3	0.58	0.55	0.27	1.1	0.68	0.32	N/A	0.18
Thermal Expansion Coefficient ($10^{-6}°C^{-1}$)	2.6	5.9	5.73	4.52	4.65	4.6	7.75	N/A	5.37

Table 1.1, table of different semiconductor materials' physical properties, which are all important factors to semiconductor device epitaxial growth, processing and performance.

1.2.2 Basic Quantum Mechanics of Semiconductor

As a solid-state material, a semiconductor is able to emit photons by recombination of electrons from the conduction band with holes from the valence band to produce photons with energy

$$E = h\upsilon \qquad \text{Equation 1.1}$$

Where E is the energy between conduction band and valence band, h is Planck constant and υ is the frequency of photons. If the electron is confined in an infinite potential well along z-

dimension, then it is free to travel among the x and y-dimensions. The energy for a continuum of states could be expressed as

$$\frac{\hbar^2}{2m}\ (k_x^2 + k_y^2) \qquad \text{Equation 1.2}$$

Where m is the effective mass of the particle, $\hbar$ is reduced Planck constant, k is the wavevector components in x and y directions.

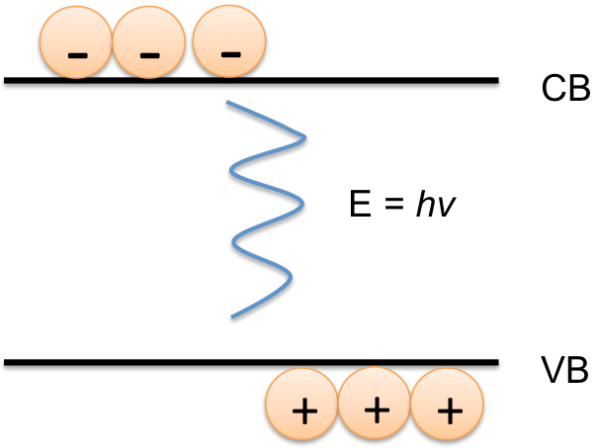

Figure 1.3 Photon emissions with electrons decay from conduction band (CB) to valence band (VB). The photon in the term of energy is related to its wavelength. Shorter wavelength can be obtained from a higher energy separation.

1.2.3 Quantum Confinement of Materials in Different Dimension.

QDs are zero-dimensional material structures with three-dimensional quantum confinement. The densities of states of bulk, quantum well, quantum wires and quantum dots materials, are presented in Figure 1.5. The particle will be quantum confined when the size of particle movement is limited by its own de Broglie wavelength $\lambda \cong h/p$, where p is the momentum of the particle equal to the mass of particle multiple velocities. The densities of states (DoS) will be modified from that of bulk condition if quantum confinement applied. For the bulk materials, the DoS are continuously due to their being no quantised levels for electrons. The equation of energy for a continuum of state bandgap should be

$$\mathrm{E} = \left(\frac{\hbar^2}{2m}\right)(k_x + k_y + k_z) \qquad \text{Equation 1.4}$$

where m is the mass for electron; *k* is the wavevector component in the x, y, z three direction. Consider an infinite boundary along z-dimension, a potential well to confine the particle between the distances L, the wavefunction of particle must be

$$\Psi = \begin{Bmatrix} 0 \\ A \sin \frac{n\pi}{L_z} \end{Bmatrix}, E_n = \frac{\hbar^2}{2m} \left(\frac{n\pi}{L_z}\right)^2$$

$$k = \frac{n\pi}{L}, n = 1, 2, 3, \ldots \qquad \text{Equation 1.5}$$

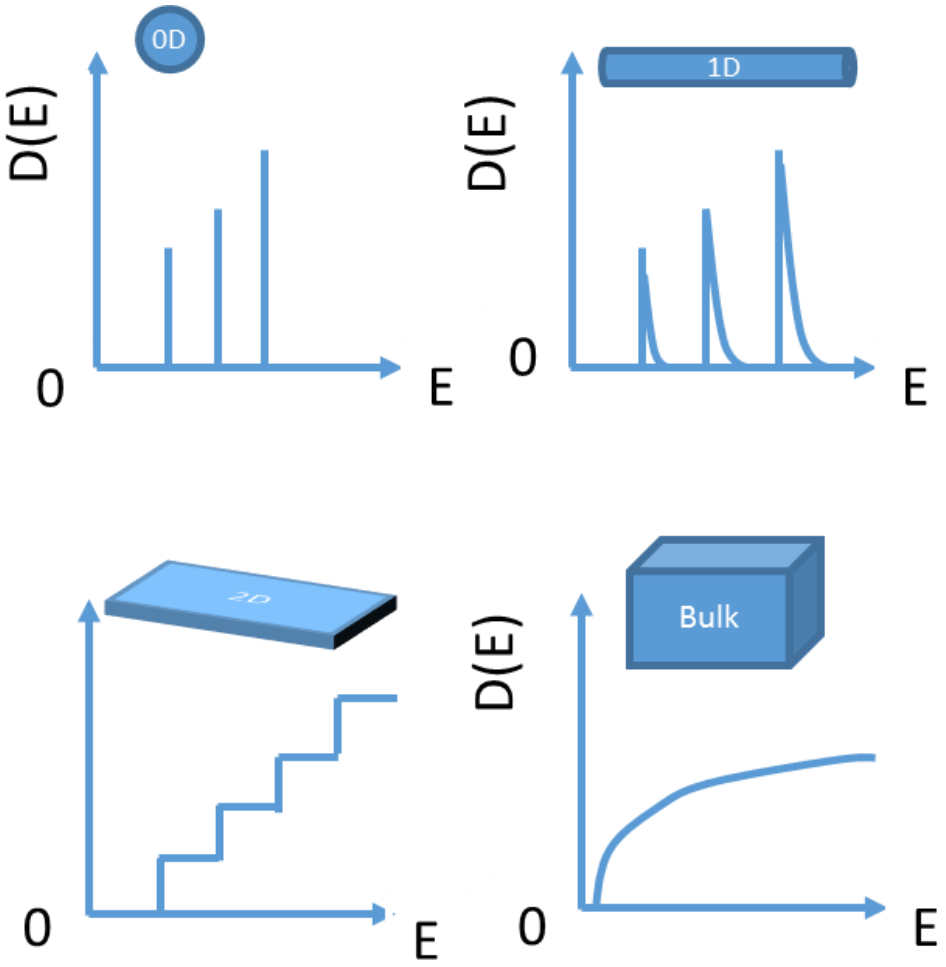

Figure 1.5 Density of states (DoS) with different dimensions of quantum confinement. In the 0D material, the DoS is discrete for QDs.

1.2.4 Quantum Dots

As a 0-D material, the energy levels of a QD are quantised due to the 3-D quantum confinement, so the DoS are discrete as Figure 1.5. A QD is a nanocrystal made of semiconductor materials that is small enough to exhibit quantum mechanical properties. Consider the quantum confinement at three dimensions is

$$E_{a,b,c} = \frac{h^2a^2}{8m^*L_x^2} + \frac{h^2b^2}{8m^*L_y^2} + \frac{h^2c^2}{8m^*L_z^2} \quad \text{Equation 1.6}$$

where (a, b, c) = 1, 2, 3, 4…. The spatial sizes of QDs defined by L_x, L_y and L_z, which ensure that it is confined in three dimensions and no continuous energy term in QD. m^* is effective mass. The separated energy levels of QDs help to trap the carriers in the structure so that thermal escape is reduced compared with QW. Another advantage of QD material is the low threshold current density of laser devices due to the carriers being confined stronger in the dots structure [24, 25]. Moreover QD is a promising solution to handle the high temperature operation due to its delta function like DoS [26]. Also the insensitivity to defects is enhanced in QD compare with QW. The dislocations including threading dislocation and misfit dislocations could easily damage the carrier transmission in the laser device, which in turn leads to significant degradation of lasing performances III–V on Si platform epitaxial growth will introduce a huge amount of threading dislocations (~10^{10} cm^{-2}). In the QW laser structure, a large portion of non-recombination centres are created due to the propagation of dislocations through the active region. However, for a laser diode with QD active region, the influence of the as only QDs directly affected by the propagation of dislocations are destoryed and the rest could still remain functional normally. Nonetheless, the effects of the dislocations on optical loss are same in both QDs and QWs

1.3 The Background of Semiconductor Lasers

As a high-power and high-efficiency light-emitting source, lasers have been studied and developed a number of years. Albert Einstein, the most famous scientist in last century, developed the theory of laser in 1930s, and defined the possibility of absorption, spontaneous emission and stimulated emission. In 1953 the first laser was established by N. Basov and Aleksandr Prokhorov from Soviet Union. Meanwhile, American scientist Charles Hard Townes and his students developed the first microwave operation but without continuous output. In 1957, Townes and Arthur Leonard Schawlow, from Bell Labs, achieved the infrared laser.

Lasers have a wide range of applications, depending on the power output and operating wavelength. For the medical usage, a suitable power of laser could kill bacteria without destroying the human issues. Semiconductor is considered as an ideal material which can form different types of structures by doping: and most commonly, laser is achieved in the p-i-n structure.

1.3.1 Basic Theory of Semiconductor Light Emitting Devices

As a mature technology of light emitting devices,Tthe operation principle of light emitting diodes (LED) is illustrated with the band diagram shown in figure 1.6. Without bias voltage, as figure 1.6 (a) shows, the depletion region is formed without hole and electron, which means that no recombination happens within the depletion region. The depletion region will shrink when bias voltage is applied $V_0 \sim E_g/e$, which allows the electrons in the n-regions to recombine with holes in the p-region as shown in figure 1.6 (b). The photon emission energy is E_g, with the interband transition of electrons and holes.

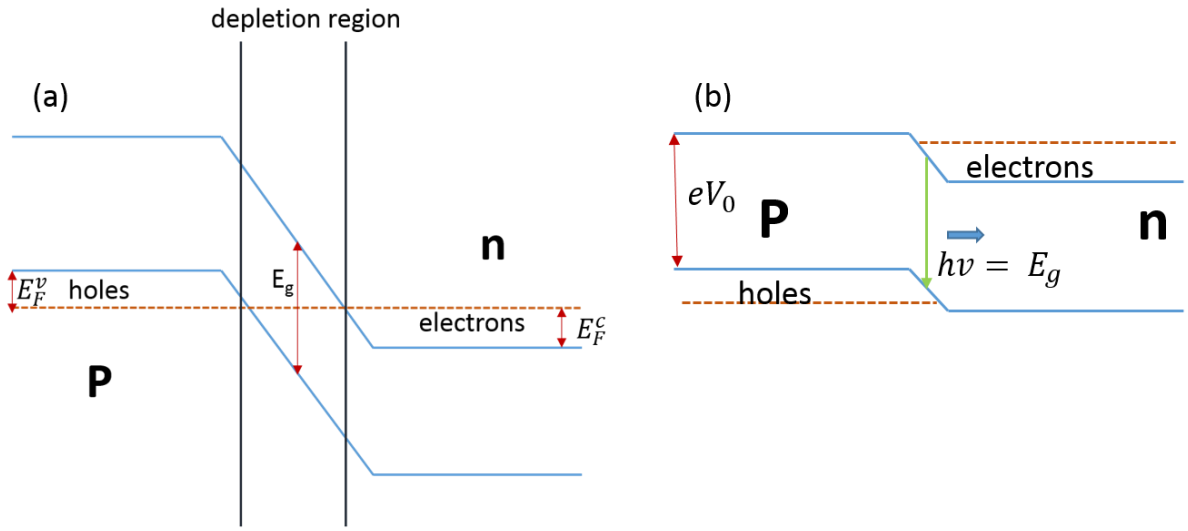

Figure 1.6 Band diagram of a LED at (a) zero bias, and (b) forward bias E_g

The acronym ‘laser’ stands for ‘Light Amplification by Stimulated Emission of Radiation’. The laser operation involves quantum mechanics of stimulated emission. Stimulated emission will increase the photon numbers by interacting photons with atoms of the medium, which cause optical amplification (gain).

Three requirements for any lasing system are

1. The gain medium
2. Population inversion
3. Pumping energy

For an incoming beam, the absorption process causes beam attenuation, in contrast, stimulated emission causes amplification. In the thermal equilibrium, as presented in the Figure 1.7, the occupation of populations will follow the Boltzmann equation

$$\frac{N_2}{N_1} = \frac{g_2}{g_1}\exp(-\frac{h\nu}{k_B T}) \qquad \text{Equation 1.7}$$

where g_1 and g_2 are the degeneracies of levels 1 and 2 respectively, k_B is Boltzmann constant. During thermal equilibrium, the stimulated emission rate (N_2) is lower than the absorption rate (N_1), which causes net beam attenuation. With the injection of pumping energy, the stimulated emission rate will be higher than the absorption rate which will cause net beam amplification. When there are enough injection of carriers, the population condition ($N_2 > N_1$) is achieved. Once the system achieves population inversion, the carriers will begin to oscillate.

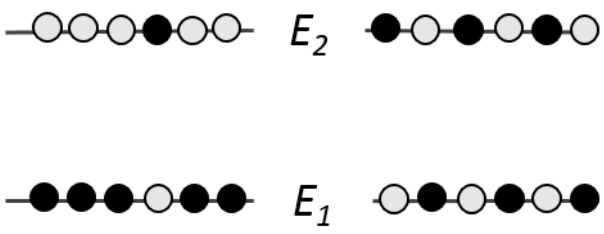

Figure 1.7 Diagram illustrating the occupation of states in a system with two levels at E_1 and E_2 in left the thermal equilibrium and right the population is inverted ($N_2 > N_1$).

1.3.2 Basic Semiconductor Lasers

There are few types of semiconductor lasers, of which some have been commercialised, including the quantum cascade laser [27, 28], and vertical-cavity surface-emitting laser,

1.3.2.1 Si Raman Laser

The Si-based lasers that implanted with the Raman Effect have been developed by Intel. A continuous-wave (CW) operation mode has been achieved by S. Rong *et al* from Intel in 2005 [29]. From the report by Rong, a CW emission around 1670 nm with slope efficiency 9.4% is achieved. The CW emission is operated with optical pumping at 1536 nm. The first cascaded Si Raman laser has been established in 2008 by the same group who created first CW operation Si Raman laser [30]. The second order emission of the cascaded laser is around 1880 nm and

output power exceeds 5 mw with optical pumping 1536 nm. The optical pumping limits the integration Raman lasers on Si platform.

1.3.2.2 Edge-emitting III–V Semiconductor Laser Diode

Regards to the excellent physical properties of III–V materials, GaAs, InP and GaN based laser diodes, which cover the emitting wavelength from visible to infrared regions, are well established. In 1960s, scientists from United States used GaAs and GaAsP as the gain medium to create a laser working that operates at 77 K with threshold current density of 50000 A/cm^{-2} [31-34]. Kroemer, the Nobel prize winner in Physics in 2000, believed the injected carriers diffuse out at the opposite side too quickly, which means the amplification process cannot occur at high temperature [35]. Then Kroemer proposed using two different semiconductor materials to create barriers to prevent electrons and holes diffusion between narrow-gap layer and wide-bandgap as shown in Figure 1.8. The first double-heterostructure (DH) laser model is developed by Alferov in 1970 [36]

In the mid- 1970s, it was discovered that quantum confinement, which can be achieved by controlling the thickness of semiconductor material, can change the wavelength of photon emitting. In this matter, the potential well plays two roles, namely, slab waveguide and confine electrons. In 1974, Dingle and his colleagues have observed the quantum confinement of states and then applied it to laser diode [37], the first optical pump quantum well laser was demonstrated by Ziel *et al* at 1975 [38], and then the electrical pumping operation was realised at 1978 by Holonyak *et al* [39]. However, the disadvantage of QW is the high sensitivity to dislocations which are emerged by lattice mismatched semiconductor materials.

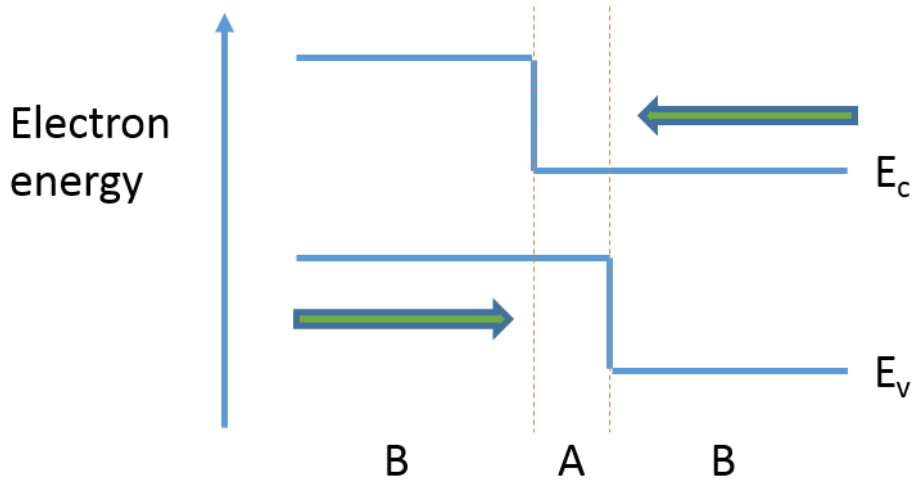

Figure 1.8 Energy band diagram of DH laser. The narrow-gap material A prevents onward diffusion of carriers which will contribute to population inversion.

The concept of three-dimensional quantum confinement laser, QD laser, was first proposed by Arakawa and Sakaki in 1982 and then developed by Asada in 1986. Compared with QW laser, QD laser has the properties of a lower threshold current density and stronger performance at higher temperature range due to its delta-function like density of states. QD laser has been widely studied by scientists since the development of self-assembled QD growth by Stranski-Krastanow mode [40, 41].

1.3.2.3 Fabry-Perot Laser and Distributed Feedback Laser

The two major types of laser diode, Fabry-Perot laser and distributed feedback (DFB) laser are fabricated as single output edge-emitting laser by applying different high-reflection mirror coatings. The outputs photons will be emitted from the smaller reflective index mirror coating.

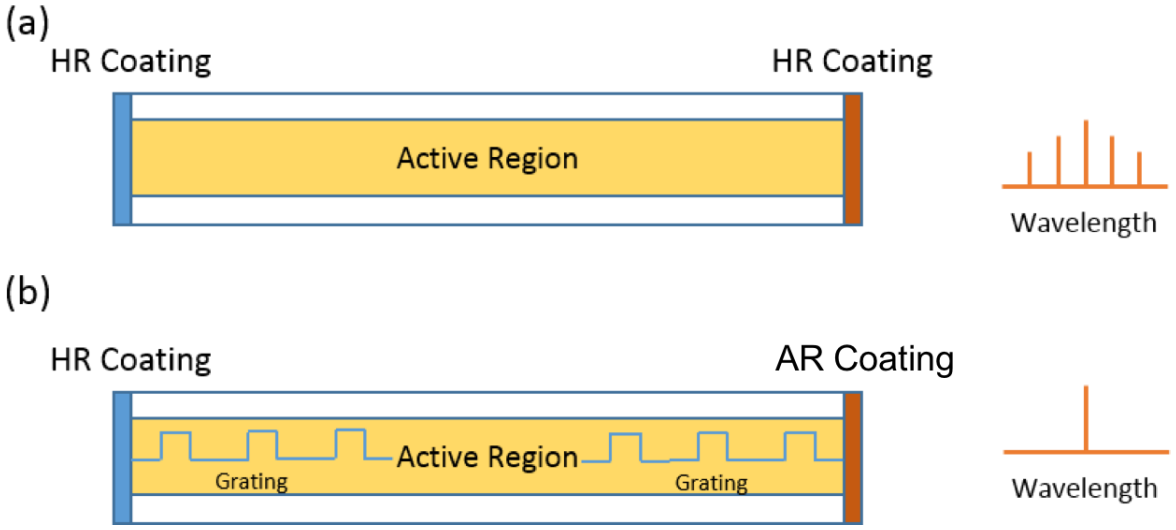

Figure 1.9 Schematic diagrams of (a) Fabry-Perot laser and (b) Distributed Feedback Laser. The emitting spectrum has been presented on the right of diagram. As seen, DFB laser has narrower bandwidth than Fabry-Perot laser on lasing spectrum.

Fabry-Perot (F-P) laser is the most common communication laser. The spectrum of laser emission will be presented as multi-mode as shown in Figure 1.9. To obtain the single mode laser, DFB laser uses optical grating to narrow the bandwidth of lasing spectrum. Bragg grating has been used commonly in DFB laser. The wavelength of lasing is filtered by the Bragg scatting. The schematics of F-P laser and DFB laser structure are presented in Figure 1.9. The coating of F-P laser is optional but DFB laser uses HR and AR coating on each of facet.

1.3.2.4 Vertical-Cavity Surface-Emitting Laser

Vertical-cavity surface-emitting lasers (VCSEL) have been widely used in the industry including in optical fibre transmission, computer mouse, and laser printing. VCSEL, represents one of the highest market shares in commercialised semiconductor laser. As shown in Figure 1.10, a VCSEL has a number of layers of quantum wells stacked in the active region and a pair of distributed Bregg Reflectors (DBR) located parallel to the active laser medium. Generally, most of VCSEL devices are based on the GaAs platform and grow by MBE, MOVPE and MOCVD. The AlGaAs/GaAs DBR are suitable for the VCSEL system due to their lattice constant are similar with different composition. The emitting wavelength of VCSEL could cover from 650 nm to 1300 nm.

The first surface-emitting laser was reported by Haruhisa Soda, Kenichi Iga, Chiyuki Kitahara and Yasuharu Suematsu in 1979 [42], and the first CW laser operating at on room temperature was achieved by Fumio Koyama, Susumu Kinoshita, and Kenichi Iga in 1988 [43]. Axel Scherer and Jack Jewell patented the first semiconductor VCSEL in 1989 [44].

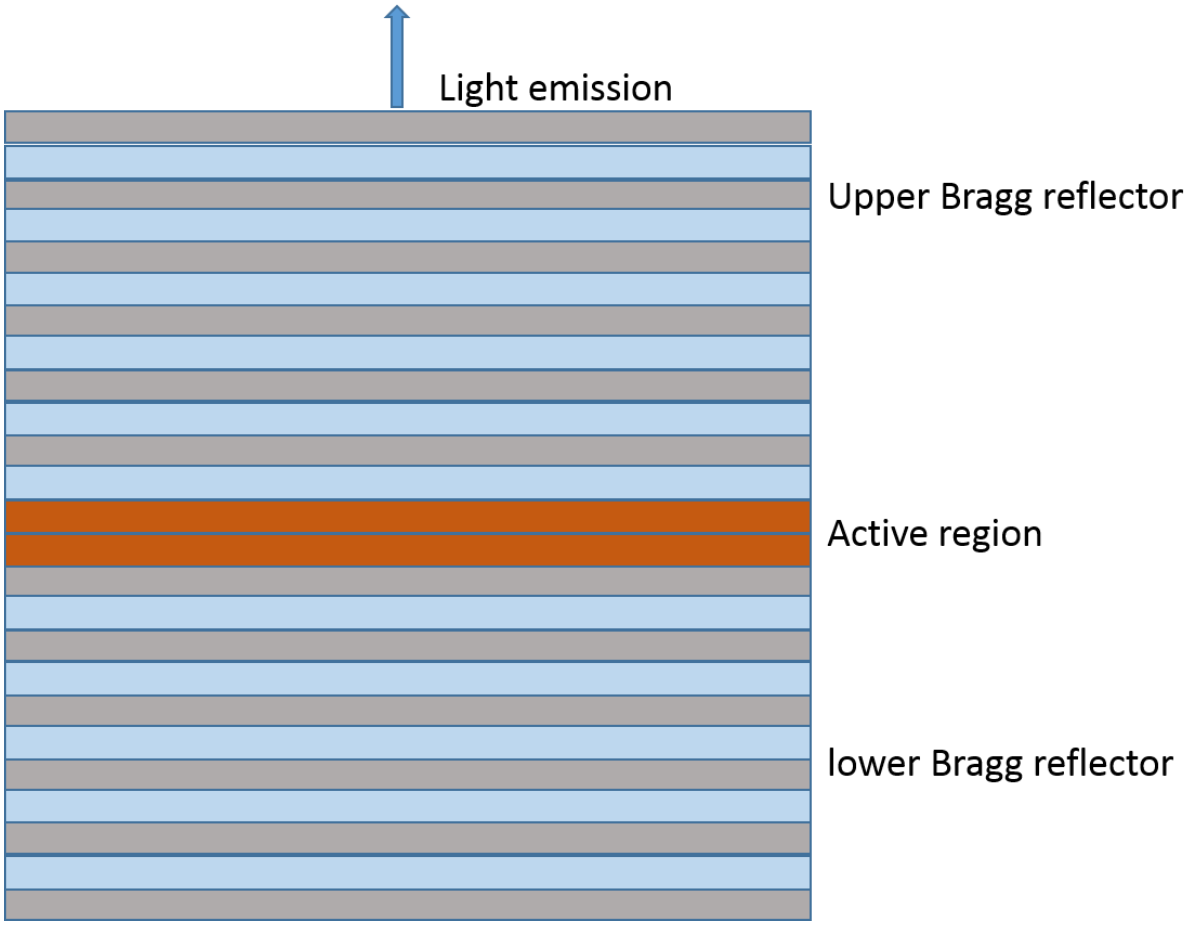

Figure 1.10 Schematic diagram of VCSEL. The active region is located between upper and lower Bragg reflector.

To obtain higher refractive index contrast from an AlGaAs/GaAs DBR, higher concentration of Al is needed, but it will cause oxidation issues if there is too much Al. In order to obtain lower threshold current density, current is restricted so that two types of VCSEL have been developed, ion-implanted VCSELs and oxide-aperture VCSELs. Ion-implanted VCSEL introduces ion (normally H+) to implant into the VCSEL all the part of structure except the aperture, which could destroy the lattice structure around the aperture, and restrict the current. Another type of VCSEL is the oxide-aperture VCSEL, where aperture is covered by oxidised metal (for example oxidised Al), and thus current is restricted inside the VCSEL.

1.3.3 Si Based Lasers

1.3.3.1 Si Hybrid Lasers

Wafer bonding technique is known as a better method to solve the issues of defects caused by the monolithical growth of III–V materials on group IV platform. A. Feng *et al* have demonstrated successful Si based hybrid AlGaInAs-silicon evanescent laser with electrical pumping in 2006 [45] with a CW operated evanescent laser device bonding on SOI (silicon-on-insulator). The laser devices were working under room temperature with 65 mA thresholds and around 1.8 mW output power. Wafer bonding technique is widely used and investigated by the researchers from UCSB and Intel. Wafer bonding technique has also been implemented in the opto-electronic integration. A. Goote *et al* reported a light emitting diode based on InP bonding with SOI substrate and emitted at four sections around 1300, 1380, 1460 and 1540nm [46].

1.3.3.2 III–V Lasers Monolithically Grown on Group IV Platform

Monolithic integration of III–V materials on Group IV platform is another solution to achieve highly efficient light-emitting devices. By using physical or chemical deposition method, high quality III–V materials can be grown on group IV platform including Si, Ge or Ge/Si substrate.

Compare d with Si hybrid laser, monolithically growth of III–V materials on Si has issue with high density of dislocations due to the lattice mismatch between III–V materials and Si. As we mentioned before, QW laser has poor performance on the highly lattice-mismatched material systems, however, the performance of InAs/GaAs QDs are much less sensitive to defects. The advantage of III–V materials could be migrated on Si and Ge platform . The III–V materials can be monolithically grown on group IV p latform using molecular beam epitaxy (MBE) technique, in whichn GaAs buffer layers on the top of a Si or Ge wafer, followed by the growth of the laser structures on the GaAs buffer layers. The thickness of GaAs buffer layer on Si wafer substrate is identical to release the strain due to the lattice mismatch between GaAs and Si [47]. InAs/GaAs quantum dots could achieve the photon spontaneous emission around 1.1, 1.3 and 1.5 μm by implementing different strain using GaAs and GaAsSb layers [48, 49]. High-performance light-emitting source including LEDs, lasers and superluminescent diodes (SLDs) based on III–V material have been well-established [50]. The quantum well and QD laser emission at 1.1, 1.3 and 1.5 μm could also be used on Si and Ge platform. In III–V material,

AlGaAs and InGaP can be used as cladding layer due to its high-energy bandgap property. AlGaAs is a promising method on GaAs because the lattice constant is similar to GaAs, which means fewer defects. Both quantum wells and QD can be considered as active region, that QW has narrow emission and QD has less sensitive to defects.

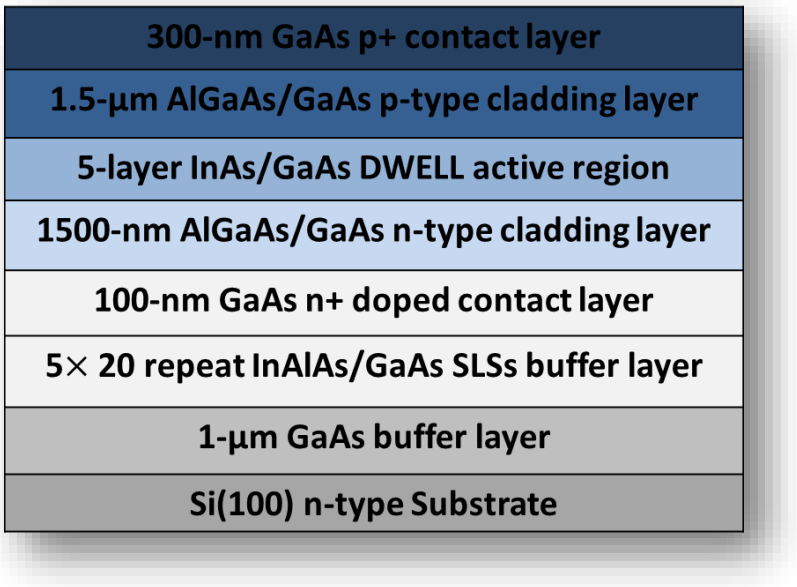

Figure 1.11 InAs/GaAs quantum dot laser structure on Si n-type substrate.

Substrates	J_{th} (A/cm^2)	Operation mode	Maximum operating temperature (°C)	Year	Publishers
Ge	**55.2**	**CW**	**60**	**2011**	**H. Liu *et al* [51]**
Ge/Si	**163**	**CW**	**30**	**2012**	**A. Lee *et al* [52]**
Ge/Si	**141.6**	**CW**	**119**	**2014**	**A. Liu *et al* [53]**
Si	**725**	**Pulsed**	**42**	**2011**	**T. Wang *et al* [47]**
Si	**194**	**Pulsed**	**85**	**2014**	**M. Tang *et al* [54]**
Si	**200**	**Pulsed**	**111**	**2014**	**S. Chen *et al* [55]**

Table 1.2 Recent results of InAs/GaAs QDs lasers monolithically grown on Si, Ge/Si and Ge substrate.

In the work done at our group [51, 52] and UCSB [53], as presented by table 1.2, InAs/GaAs quantum dots laser monolithically grown on Si, Ge and Si/Ge have been demonstrated at high

performance. C.w. operated and high reliabiliable QD Lasers have been achieved on Si/Ge and Ge substrate [56], with low threshold current density as well. Figure 1.11 shows the quantum dot laser structure grow directly on Si substrate, which demonstrated low threshold current density at 194 A/cm^2 and as high operating temperature 85 ºC.

Very recently, Z. Wang *et al* have demonstrated InP DFB array laser on Si substrate however it only can be worked with optical pump [57]. They use v-grooved Si substrate to reduce the defects which is a smart choice.

1.3.3.3 Group IV Lasers

For the group IV laser, in 2014, optical pump operated GeSn laser on Si have been demonstrated by S. Wirths *et al* [58]. In the earlier time, the Ge/Si laser demonstrated by J. Liu *et al* in 2010 but struggling with the high loss on group IV materials system [59]. Indeed, lasers with quantum confinement also have opportunity to play an important role in silicon photonics.

1.3.4 The Advantage of Epitaxy Growth

Epitaxial growth could bring high quality to crystal growth. For MBE, the growth is running under an ultra-high vacuum (UHV) environment and the growth rate is controlled precisely by molecular beam. In a MBE system, compare with MOCVD system, high purity solid source (or gas source) (>99.99999%) could be used, while organic source and chemical reaction are used in MOCVD system. MBE also ensures the growth rate can be lowered to the 0.01 monolayer per second (ML/s) level, which guarantees high accuracy of epi-layer thickness and composition during the epitaxial growth.

The major issues related to the heteroepitaxial growth of III–V material on Si substrates are the defects propagating from the interface of the III–V material with the Si surface. The types of defects and their corresponding solutions are presented in the next chapter.

1.4 The Defects of III–V Material Monolithically Grown on IV Platform

The integration technique decides the performance of III–V devices on Si platform. Si hybrid lasers use a bonding technique to directly bond Si substrate and III–V material. However, there are a few disadvantages of bonding technique including the high threshold current density (J_{th}) [60, 61], high cost [62] and low yield.

III–V materials monolithically grown on Ge or Si substrates is another integration method. However, the main issues of this method are the defects in the heterostructure like GaAs/Si. Also in the heterostructure epitaxy growth, the lattice mismatch brings the trouble to devices by formation of dislocations into crystal.

The defects can be classified by their dimensions. The 0-dimensional defects called point defects which normally caused by impurity and affects isolated sites in crystal structure. The 1-dimensional defects are dislocations and 2-dimensional defects include grain boundaries and external surface. The 3-dimensional defects change the crystal pattern over a finite volume which includes precipitates. The precipitates are usually small volumes of different crystal structure and large voids.

The point defects can be distinguished as two types, intrinsic and extrinsic. The intrinsic defect is an atom occupies an interstitial site where no atoms belong there, or an atom missing on its original position. The extrinsic defect is caused by impurity atoms. The point defects affect the resistivity of metals by conducting electron scattering and electronic conduction. On the optical side, more electrons states are introduced.

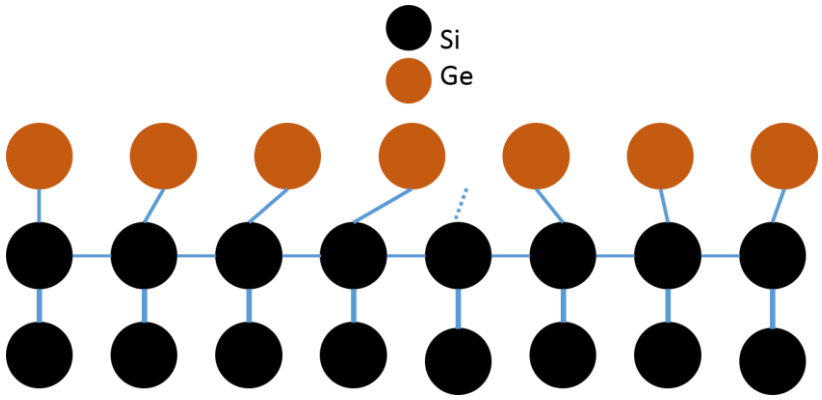

Figure 1.12 The formation of misfit dislocation in the interface of Si/Ge

The lattice mismatch between Si and Ge (4%) induced the edge misfit [63**]**. Figure 1.12 shows the mismatched Si atom which does not have Ge atom to connect. It will force the whole layer of Ge have misfit in the edge which is called misfit dislocation. The misfit dislocation cannot affect the crystal quality too much however it has the possible to produce threading dislocation

as a way to relive the internal stress. The effects of dislocations have mainly three parts. Firstly, the atoms along the dislocations are depleted because dislocations create huge amount of deeper states and occupied by majority carriers. Secondly, non-radiative recombination centre for minority carriers appeared due to the dislocations. Thirdly, hopping conduction will be appeared and leakage current increased. All these three effects degrade the performance of electronic and opto-electronic devices.

Figure 1.13 shows the formation of antiphase domains boundary (APD) in polar to non-polar epitaxy grows. And Figure 1.14 shows the top-view morphology of APD measured by AFM. The APD is formed due to the impossible connection between As to As or Ga to Ga atoms, which will propagate through the whole structure without stopping [64, 65]. The two-step growth and off-cut substrate solve the problem by letting the APD elimination when they meeting together from two directions. The two-step growths can be achieved on Si substrate with (100) 4° oriented to <110> or Ge substrate with (100) 6° oriented to <110, which involve first a GaAs buffer layer grown at low temperature (400 ˚C) and growth rate (0.1 ML/s), and the rest of 970 nm GaAs grown at higher temperature and growth rate.

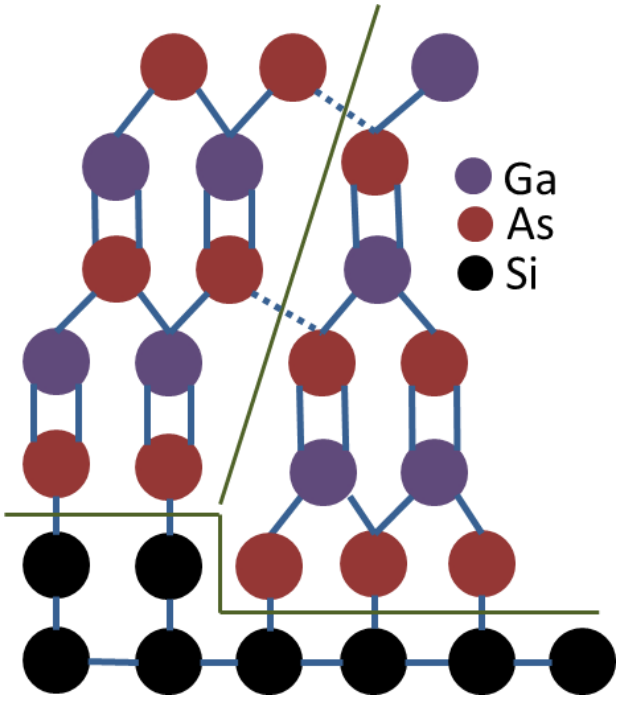

Figure 1.13 The formation of APD by growing GaAs on Si substrate. The bonding between As atoms are impossible so that cracks appear during the polar to non-polar material growth.

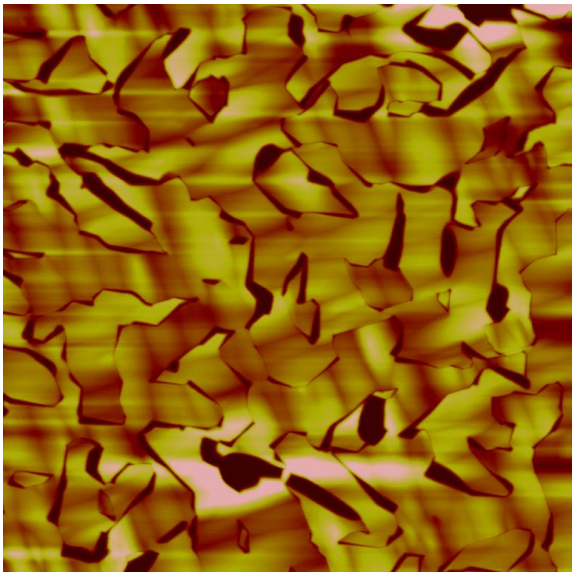

Figure 1.14 AFM image of 200 nm GaAs on Ge (100) substrate grown by MBE system with full of APD.

Another type of defects bothers the researchers in III–V monolithically grown on group IV platform is threading dislocation, which are normally caused by the strain at the interface between III–V material and group IV material. Figure 1.15 shows the high number of density of threading dislocations in the region near to GaAs/Si interface. The sample is grown by a MBE system with a two-step growth, First, 30 nm of GaAs layer is grown at low temperature (400 ºC) and the rest of the 970 nm GaAs is grown at higher temperature. The low temperature of GaAs growth can reduce the density of defects.

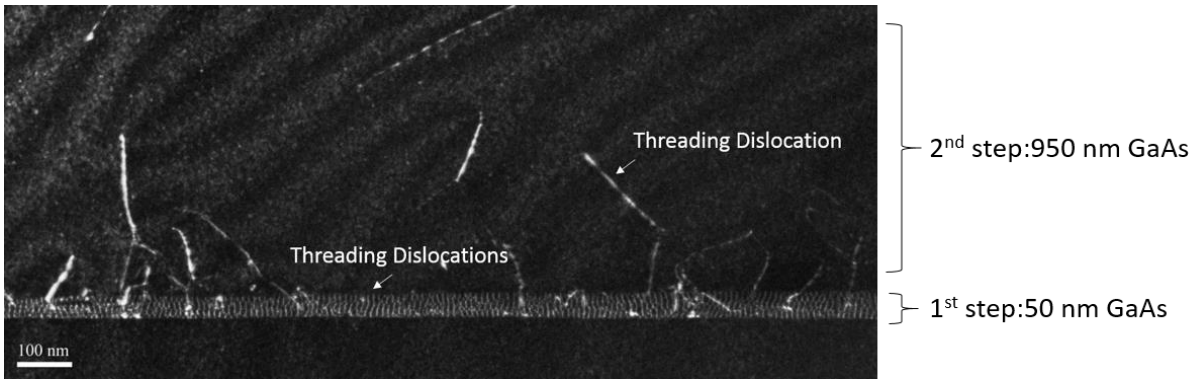

Figure 1.15 TEM image of GaAs on Si substrate grown by MBE with threading dislocations. The high density of TDs is observed in the first ~50 nm GaAs buffer layer and largely in the 2nd step. The TEM image is measured by University of Arkansas.

1.5 Defects Filter Layer and Strained-layer Superlattices

Before we design the DFLs, the mechanism of how dislocations ended needs to be explained. The dislocations can be ended by three methods, 1) it reaches the surface of crystal; 2) it encounter a perpendicular dislocations and eliminated by each other; 3) the resulting misfit dislocation array relieves a sufficient amount of misfit for the net glide force on the threading dislocation to drop to zero [66]. To dealt with TDs, we could let them increase the possibility to encounter each other by increasing the thickness of buffer. However the crack will be appeared when the thickness of buffer layers is over 3 μm for GaAs on Si due to the different thermal expansion coefficient. It is necessary to introduce another layer to form arrays of misfit dislocations to encounter with TDs with enough net glide forces.

In this sentence, SLSs have been considered as a significant method to reduce the effects from TDs by reducing the TDs density. As shown in figure 1.16, SLSs are formed with periodic two types of 2-dimensional semiconductor material with lattice mismatch for example $In_xGa_{1-x}As$ and GaAs, $In_xGa_{1-x}N$ and GaN, the unrealised strained force is possible to change the TDs' propagating direction. The arrows show their strain force direction which used to bend the direction of TDs' propagating. Only the certain direction of strain force could successfully effect on the TDs.

To optimise SLSs, the strain force is the most significantly part needs to be concerned. In general, the larger lattice mismatch of SLSs will introduce higher strain force, which will be more efficient to stop TDs' propagation. However, the larger strain has more chance to create new defects as well, which means the balance between strain and defects is significantly important. Also the thickness of SLSs is important to how much the strain will be relived. For different SLSs materials, the atoms bonding energy needs to be considered as well. The higher bonding energy should able to let less TDs penetration.

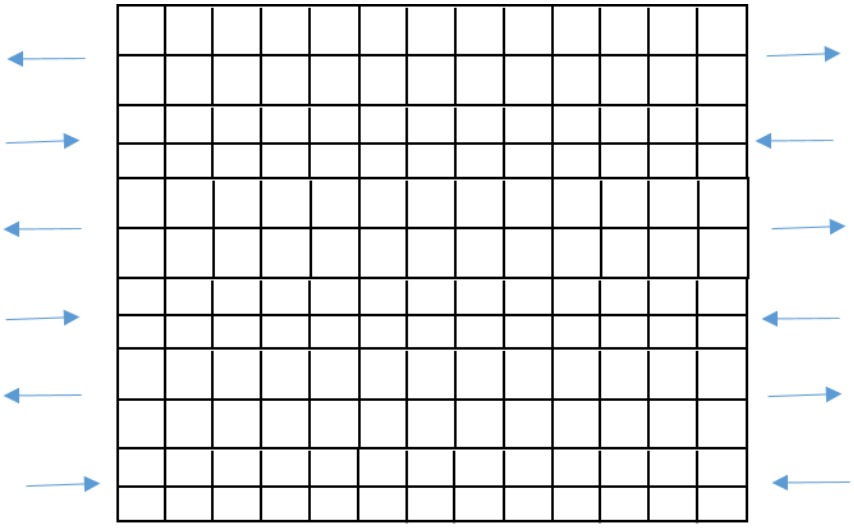

Figure 1.16 SLSs formed by two types of lattice mismatched material.

Until now, few methods of strained layer have been demonstrated based on different platforms including InGaN/GaNsuperlattice strained-layers (SLSs) on GaN substrates [67], InGaAs/GaAs SLSs and InAs/GaAs QDs on Si substrates [68, 69]. Figure 1.17 clearly shows the defects filter layers (DFLs) formed by three sets of SLSs reduce the density of dislocations significantly. In the beginning, the TDs went through GaAs buffer layers and then stopped by DFLs mostly. The direction of TDs is parallel to DFLs due to the strain force of SLSs. The mechanism of strained layer stop the dislocations is the large misfit stress acts to push dislocations out of the layer which the misfit stress comes from the lattice mismatched materials.

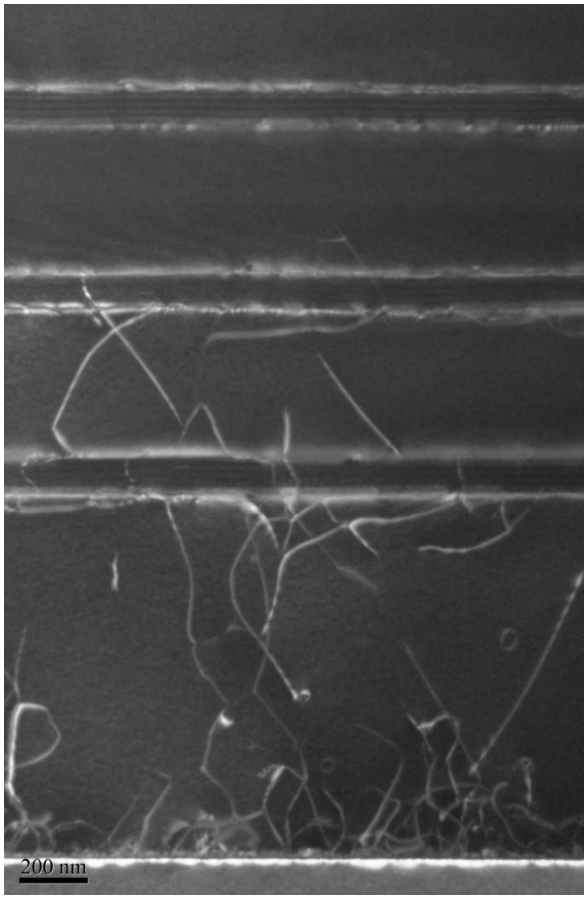

Figure 1.17 TEM image of three repeats of DFL, which is formed by 10 layers of InAlAs/GaAs SLSs. The dislocations are hard to find after two repeats of InAlAs/GaAs SLSs DFL. The TEM image is measured by University of Arkansas.

1.6 The Organisation of the Thesis

In this thesis, the main objective is to explore the details of fabrication and processing of InAs/GaAs QDs laser on Si substrates using InAlAs/GaAs SLSs DFLs. Low threshold current density lasers have been demonstrated in the thesis. Chapter 1 describes the motivation for Si photonics and the combination of InAs/GaAs quantum dots and Si platform. The background and principle of quantum dot lasers have been discussed also in this chapter.

Chapter 2 illustrates the principles of equipment used in the experiment. MBE, as the most important facility in the research projects, used to monolithically grow quantum dots on Si substrates. The details of MBE are presented in this chapter, including components such as Reflection High Electron Energy Diffraction (RHEED), and different pumps. The operation of X-ray diffraction is mentioned, which measures the composition of ternary or quaternary alloy, the strain of semiconductor compounds. The principle and operation of atomic force

microscopy (AFM) and photoluminescence (PL), as two major characteristic measurements method will be discussed as well.

Chapter 3 talks about the growth details of InAs/GaAs QDs on Si substrates which consists of GaAs nucleation optimisation, defect filter layers (DFLs) growth and InAs/GaAs QDs optimisation. TEM, AFM and PL are used to examine the crystal quality of devices. The study of different DFLs including InAs/GaAs QDs, InGaAs/GaAs SLSs and InAlAs/GaAs SLSs. The structures with different DFLs have been examined by PL, AFM and TEM. The laser devices with InAlAs/GaAs SLSs have been tested and discussed.

Chapter 4 gives the study of the first superluminescent diode monolithically grown on Si platform by using MBE system. The TEM, PL and AFM are used to examine the crystal quality. L-I measurement is used to examine the superluminescense in the absorption section of device.

Chapter 5 describes the optimisation of InGaAs/GaAs SLSs DFLs regards to three steps, improving GaAs spacer layer, modifying indium composition and GaAs thickness in InGaAs/GaAs SLSs DFLs. Two lasers have been fabricated based on the reference and optimised DFLs condition where L-I shows the improvements are significantly on optimised DFLs.

Chapter 6 is the summary of the works since the start of my PhD study. The future work of InAs/GaAs quantum dot laser on Si will be mentioned.

Reference

1. Yu B. Bolkhovityanov, and Oleg Petrovich Pchelyakov. “GaAs epitaxy on Si substrates: modern status of research and engineering”, *Physics-Uspekhi,* vol. 51, no. 5, pp. 437, 2008
2. R. Ho , K. W. Mai and M. A. Horowitz "The future of wires", *Proc. IEEE*, vol. 89, pp. 490 -504, 2001
3. David Miller, “Device Requirements for Optical Interconnects to Silicon Chips”, *Proceeding of the IEEE*, vol. 97, no. 7, pp. 1166-1185, 2009
4. H. Cho , P. Kapur and K. C. Saraswat "Power comparison between high-speed electrical and optical interconnects for interchip communication", *J. Lightw. Technol.*, vol. 22, no. 9, pp. 2021 -2033, 2004

5. A. F. Benner, M. Ignatowski , J. A. Kash , D. M. Kuchta and M. B. Ritter "Exploitation of optical interconnects in future server architectures", *IBM J. Res. Develop.*, vol. 49, no. 4/5, pp. 755 -775, 2005
6. D. A. B. Miller "Optical interconnects to silicon", *IEEE J. Sel. Topics Quantum Electron.*, vol. 6, pp. 1312 -1317, 2000
7. https://en.wikipedia.org/wiki/Moore%27s_law
8. D. Liang and J. E. Bowers, "Recent progress in lasers on silicon", *Nature Photonics*, vol. 4, no. 8, pp. 511–517, 2010
9. Jifeng Liu, Xiaochen Sun, Dong Pan, Xiaoxin Wang, Lionel C. Kimerling, Thomas L. Koch, and Jurgen Michel, "Tensile-strained, n-type Ge as a gain medium for monolithic laser integration on Si", *Optics Express*, vol. 15, no. 18, pp. 11272-11277, 2007
10. Bruce M. Green, Kenneth K. Chu, E. Martin Chumbes, Joseph A. Smart, James R. Shealy, and Lester F. Eastman, "The effect of surface passivation on the microwave characteristics of undoped AlGaN/GaN HEMTs", *IEEE Electron Device Letters*, vol. 21, no. 6, pp. 268, 2000
11. S.C. Binari, K. Ikossi, J. A. Roussos, Walter Kruppa, Doewon Park, Harry B. Dietrich, Daniel D. Koleske, A. E. Wickenden and Richard L. Henry, "Trapping effects and microwave power performance in AlGaN/GaN HEMTs", *Electron Devices, IEEE Transactions on* vol. 48, no. 3, pp. 465 – 471, 2001
12. Razeghi, M., M. Defour, R. Blondeau, F. Omnes, Ph Maurel, O. Acher, F. Brillouet, J. C. C‐Fan, and J. Salerno. "First cw operation of a $Ga_{0.25}In_{0.75}As_{0.5}P_{0.5}$-InP laser on a silicon substrate", *Applied Physics Letters*, vol. 53, no. 24, pp. 2389-2390, 1988
13. H. Q. Le, , G. W. Turner, S. J. Eglash, H. K Choi and D. A. Coppeta, "High-power diode-laser-pumped InAsSb/GaSb and GaInAsSb/GaSb lasers emitting from 3 to 4 μm", *Applied Physics Letters*, vol. 64, no. 2, pp. 152-154, 1994
14. U. Nowotny, Z. Lao, A. Thiede, H. Lienhart, J. Hornung, C. Kaufel, K. Kohler and K. Glorer, "44 Gbit/s 4:1 multiplexer and 50 Gbit/s 2:1 multiplexer in pseudomorphic AlGaAs/GaAs-HEMT technology", *Circuits and Systems, 1998. ISCAS '98. Proceedings of the 1998 IEEE International Symposium on*, vol. 2, pp. 201 – 203, 1998
15. Jin-Hee Lee, Hyung-Sup Yoon, Byung-Sun Park, Chul Soon Park, Sang-Soo Choi, and Kwang-Eui Pyun, "Pseudomorphic AlGaAs/InGaAs /GaAs High Electron Mobility Transistors with Super Low Noise Performances of 0.41 dB at 18 GHz" *ETRI Journal*, vol. 19, no. 3, pp. 171, 1996

16. News, Northrop Grumman sets record with terahertz IC amplifier, Semiconductor Today, 31 Oct 2014
17. C de Mello Donegá, A.A Bol and A Meijerink, "Time-resolved luminescence of ZnS:Mn2+ nanocrystals", *Journal of Luminescence*, vol. 96, no. 2 – 4, pp. 87–93, 2002
18. Sean Keuleyan, Emmanuel Lhuillier, and Philippe Guyot-Sionnest, "Synthesis of Colloidal HgTe Quantum Dots for Narrow Mid-IR Emission and Detection", *J. Am. Chem. Soc.*, vol. 133, no. 41, pp. 16422 – 16424, 2011
19. http://www.tf.uni-kiel.de/matwis/amat/semi_en/kap_5/backbone/r5_1_4.html
20. H.Y. Liu, M.J. Steer, T.J. Badcock, D.J. Mowbray, M.S. Skolnick, P. Navaretti, K.M. Groom, M. Hopkinson, R.A. Hogg, "Long-wavelength light emission and lasing from InAs/GaAs quantum dots covered by a GaAsSb strain-reducing layer," *Appl. Phys. Letters*, vol. 86, pp. 143108, 2005
21. Siming Chen, Wei Li, Jiang Wu, Qi Jiang, Mingchu Tang, Samuel Shutts, Stella N. Elliott, Angela Sobiesierski, Alwyn J. Seeds, Ian Ross, Peter M. Smowton and Huiyun Liu, "Electrically pumped continuous-wave III–V quantum dot lasers on silicon", *Nature Photonics*, vol. 10, pp. 307-311, 2016
22. Xue Huang, Yuncheng Song, Taizo Masuda, Daehwan Jung and Minjoo Lee, "InGaAs/GaAs quantum well lasers grownon exact GaP/Si (001)", *Electronics Letters*, vol. 50, no. 17, pp. 1226-1227, 2014
23. E Tournié, L Cerutti, JB Rodriguez, H Liu, J Wu, S Chen, "Metamorphic III–V semiconductor lasers grown on silicon", *MRS Bulletin*, vol. 41, no. 3, pp. 218-223, 2016
24. I. R. Sellers, H. Y. Liu, K. M. Groom, D. T. Childs, D. Robbins, T. J. Badcock, M. Hopkinson, D. J. Mowbray and M. S. Skolnick, "1.3 μm InAs/GaAs multilayer quantum-dot laser with extremely low room-temperature threshold current density", *Electronics Letters*, vol. 40, no. 22, pp. 1412 – 1413, 2004
25. G. T. Liu, A. Stintz, H. Li, K. J. Malloy and L. F. Lester, "Extremely low room-temperature threshold current density diode lasers using InAs dots in In0.15Ga0.85As quantum well", *Electronics Letters*, vol. 35, no. 14, pp. 1163 – 1165, 1999
26. Mitsuru Sugawara, and Michael Usami. "Quantum dot devices: Handling the heat", *Nature Photonics*, vol. 3, no. 1, pp. 30-31, 2009
27. Jerome Faist, Federico Capasso, Deborah L. Sivco, Carlo Sirtori, Albert L. Hutchinson and Alfred Y. Cho, "Quantum Cascade Laser", *Science*, vol. 264, no. 5158, pp. 553-556, 1994

28. Patent, Federico Capasso, Alfred Yi Cho, Jerome Faist, Albert Lee Hutchinson, Gaetano Scamarcio, Carlo Sirtori and Deborah Lee Sivco, “Quantum cascade laser”, US 5936989 A
29. Haisheng Rong, Richard Jones, Ansheng Liu, Oded Cohen, Dani Hak, Alexander Fang and Mario Paniccia, “A continuous-wave Raman silicon laser”, *Nature*, vol. 433, pp. 725-728, 2005
30. Haisheng Rong, Shengbo Xu, Oded Cohen, Omri Raday, Mindy Lee, Vanessa Sih and Mario Paniccia, “A cascaded silicon Raman laser”, *Nature Photonics*, vol. 2, pp. 170 – 174, 2008
31. Nick Holonyak Jr, and S. F. Bevacqua. “Coherent (visible) light emission from Ga ($As_{1-x}P_x$) junctions”, *Applied Physics Letters*, vol. 1, no. 4, pp. 82-83, 1962
32. Quist, T. M., R. H. Rediker, R. J. Keyes, W. E. Krag, B. Lax, Al L. McWhorter, and H. J. Zeigler., “Semiconductor maser of GaAs”, *Applied Physics Letters*, 1, pp. 91-92, 1962
33. Nathan, Marshall I., William P. Dumke, Gerald Burns, Frederick H. Dill Jr, and Gordon Lasher., “Stimulated emission of radiation from GaAs pn junctions”, *Applied Physics Letters*, vol. 1, pp.62-64, 1962
34. Hall, Robert N., G. E. Fenner, J. D. Kingsley, T. J. Soltys, and R. O. Carlson. "Coherent light emission from GaAs junctions." *Physical Review Letters*, vol. 9, no. 9, pp. 366, 1962
35. Nobel Prize in Physics 2000: Hebert Kroemer-Biographical, at <http:www.nobelprize.org/>
36. Alferov, Zh I., V. M. Andreev, E. L. Portnoi, and M. K. Trukan. "AlAs-GaAs heterojunction injection lasers with a low room-temperature threshold." *Sov Phys Semiconductors*, vol. 3, no. 9, pp. 1107-1110. 1970
37. Dingle, R., W. Wiegmann, and Ch H. Henry. "Quantum states of confined carriers in very thin $Al_xGa_{1-x}As$-GaAs-$Al_xGa_{1-x}As$ heterostructures." *Physical Review Letters*, vol. 33, no. 14, pp. 827, 1974
38. Van der Ziel, J. P., R. Dingle, R. C. Miller, W. Wiegmann, and W. A. Nordland Jr. "Laser oscillation from quantum states in very thin GaAs-$Al_{0.2}Ga_{0.8}As$ multilayer structures." *Applied Physics Letters*, vol. 26, no. 8, pp. 463-465, 1975
39. Holonyak Jr, N., R. M. Kolbas, R. D. Dupuis, and P. D. Dapkus. "Room-temperature continuous operation of photopumped MO-CVD $Al_xGa_{1-x}As$-GaAs-$Al_xGa_{1-x}As$ quantum-well lasers." *Applied Physics Letters*, vol. 33, no. 1, pp. 73-75, 1978

40. Y. Arakawa, and Hiroyuki Sakaki, "Multidimensional quantum well laser and temperature dependence of its threshold current." *Applied Physics Letters*, vol. 40, no. 11, pp. 939-941, 1982
41. Asada, Masahiro, Yasuyuki Miyamoto, and Yasuharu Suematsu. "Gain and the threshold of three-dimensional quantum-box lasers," *Quantum Electronics, IEEE Journal of*, vol. 22, no. 9, pp. 1915-1921, 1986
42. H Soda, Y Motegi, K Iga. "GaInAsP/InP Surface Emitting Injection Lasers". Japanese *Journal of Applied Physics*, vol. 18, no. 12, pp. 2329–2330,1979
43. Fumio Koyama, Susumu Kinoshita, Kenichi Iga, "Room temperature cw operation of GaAs vertical cavity surface emitting laser". *Trans. IEICE*, vol. E71, no. 11, pp. 1089–1090, 1988
44. Jack L. Jewell and Axel Scherer, "-Surface emitting semiconductor laser", US Patent, 4949350 A, Aug 14, 1990
45. Alexander W. Fang, Hyundai Park, Oded Cohen, Richard Jones, Mario J. Paniccia, and John E. Bowers, "Electrically pumped hybrid AlGaInAs-silicon evanescent laser", *Optics Express*, vol. 14, no. 20, pp. 9203-9210, 2006
46. A. De Groote, J. D. Peters, M. L. Davenport, M. J. R. Heck, R. Baets, G. Roelkens, and J. E. Bowers, "Heterogeneously integrated III–V-on-silicon multibandgap superluminescent light-emitting diode with 290 nm optical bandwidth", *Optics Letter*s, vol. 39, no. 16, pp. 4784-4787, 2014
47. Ting Wang, Huiyun Liu, Andrew Lee, Francesca Pozzi, and Alwyn Seeds, "1.3-μm InAs/GaAs quantum-dot lasers monolithically grown on Si substrates," *Optics Express*, vol. 18, no. 12, pp. 11381-11386, 2011
48. Z. Mi; S. Fathpour; P. Bhattacharya, "Measurement of modal gain in 1.1 μm p-doped tunnel injection InGaAs/GaAs quantum dot laser heterostructures," *Electronics Letters*, vol. 41, no. 23, pp. 1282 – 1283,2005
49. C.Y. Jin, H.Y. Liu, T.J. Badcock, K.M. Groom, M. Gutie´rrez, R. Royce, M. Hopkinson and D.J. Mowbray, "High-Performance Three-Layer 1.3-m InAs–GaAs Quantum-Dot Lasers With Very Low continuous-Wave Room-Temperature Threshold Currents", *Optoelectronics, IEE Proceedings*, vol. 153, no. 6, pp. 280-283, 2006
50. S. M. Chen, M. C. Tang, Q. Jiang, J. Wu, V. G. Dorogan, M. Benamara, Y. Mazur, G. Salamo, P. Smowton, A. Seeds and H. Liu, "InAs/GaAs quantum-dot superluminescent light-emitting diode monolithically grown on a Si substrate," *ACS Photonics*, vol. 1. No. 7,

pp. 638–642, 2014

51. H. Liu, T. Wang, Q. Jiang, R. Hogg, F. Tutu, F. Pozzi, A. Seeds, "Long-wavelength InAs/GaAs quantum-dot laser diode monolithically grown on Ge substrate," *Nature Photonics*, vol. 5, no. 7, pp. 416–419, 2011
52. A Lee, Q Jiang, M Tang, A Seeds, H Liu, "Continuous-wave InAs/GaAs quantum-dot laser diodes monolithically grown on Si substrate with low threshold current densities" *Optics express*, vol. 20, no. 20, pp. 22181-22187, 2012
53. A.Y. Liu, R.W. Herrick, O. Ueda, P.M. Petroff, A. Gossard, J.E. Bowers, "Reliability of InAs/GaAs quantum dot lasers epitaxially grown on silicon", *Selected Topics in Quantum Electronics, IEEE Journal of,* vol. 21, no. 6, pp. 1900708, 2015Mingchu Tang, Siming Chen, Jiang Wu, Qi Jiang, Vitaliy G. Dorogan, Mourad Benamara, Yuriy I. Mazur, Gregory J. Salamo, Alwyn Seeds, Huiyun Liu, " 1.3-μm InAs/GaAs quantum-dot lasers monolithically grown on Si substrates using InAlAs/GaAs defect filter layers", Optics Express, vol. 22, no. 10, pp. 11528-11535, 2014
54. SM Chen, MC Tang, J Wu, Q Jiang, VG Dorogan, M Benamara, YI Mazur, GJ Salamo, AJ Seeds, H Liu, "1.3 μm InAs/GaAs quantum-dot laser monolithically grown on Si substrates operating over 100 C", Electronics Letters, vol. 50, no. 20, pp. 1467-1468, 2014
55. A.Y. Liu, R.W. Herrick, O. Ueda, P.M. Petroff, A. Gossard, J.E. Bowers, "Reliability of InAs/GaAs quantum dot lasers epitaxially grown on silicon", *Selected Topics in Quantum Electronics, IEEE Journal of,* vol. 21, no. 6, pp. 1900708, 2015
56. Zhechao Wang, Bin Tian, Marianna Pantouvaki, Weiming Guo, Philippe Absil, Joris Van Campenhout, Clement Merckling, and Dries Van Thourhout. "Room-temperature InP distributed feedback laser array directly grown on silicon," Nature Photonics, vol. 9, no. 12, pp. 837-842, 2015
57. S. Wirths, R. Geiger, N. von den Driesch, G. Mussler, T. Stoica, S. Mantl, Z. Ikonic *et al*. "Lasing in direct-bandgap GeSn alloy grown on Si," *Nature photonics*, vol. 9, no. 2 pp. 88-92, 2015
58. Liu, Jifeng, Xiaochen Sun, Rodolfo Camacho-Aguilera, Lionel C. Kimerling, and Jurgen Michel. "Ge-on-Si laser operating at room temperature," *Optics letters*, vol. 35, no. 5, pp. 679-681, 2010
59. F. Höhnsdorf, J. Koch, S. Leu, W. Stolz, B. Borchert, and M. Druminski. "Reduced threshold current densities of (GaIn)(NAs)/GaAs single quantum well lasers for emission

wavelengths in the range 1.28-1.38 μm', *Electronics Letters*, vol. 35, no. 7, pp. 571-572, 1999

60. Xiankai Sun, Avi Zadok, Michael J. Shearn, Kenneth A. Diest, Alireza Ghaffari, Harry A. Atwater, Axel Scherer, and Amnon Yariv, "Electrically pumped hybrid evanescent Si/InGaAsP lasers", *Optics Letters*. vol. 34, no. 9, pp. 1345-1347, 2009
61. Lei Bi, Juejun Hu, Peng Jiang, Dong Hun Kim, Gerald F. Dionne, Lionel C. Kimerling, and C. A. Ross. "On-chip optical isolation in monolithically integrated non-reciprocal optical resonators, *Nature Photonics*, vol. 5, no. 12 pp, 758-762. 2011
62. Yu. B. Bolkhovityanov, A. S. Deryabin, A. K. Gutakovskii, L.V. Sokolov, "Edge misfit dislocations in the GeSi/Si(001) pair: Conditions and specific features of high-quantity generation", *Journal of Crystal Growth*, vol. 338, no. 1, pp. 12–15, 2012
63. S. Strite, D. Biswas, N. S. Kumar, M. Fradkin and H. Morkoç, "Antiphase domain free growth of GaAs on Ge in GaAs/Ge/GaAs heterostructures", *Appl. Phys. Letters*, vol. 56, no. 3, pp. 244-246, 1990
64. Herbert Kroemer, "Sublattice allocation and antiphase domain suppression in polar-on-nonpolar nucleation", *J. Vac. Sci. TechnologyB*, vol. 5, no. 4, pp. 1150-1154, 1987
65. R. Beanland , D.J. Dunstan & P.J. Goodhew, "Plasetic relaxation and relaxed buffer layers for semiconductor epitaxy", *Advances in Physics*, vol. 45, no. 2, pp. 87-146, 1996
66. Shuji Nakamura, Masayuki Senoh, Shin-ichi Nagahama, Naruhito Iwasa, Takao Yamada, Toshio Matsushita,Hiroyuki Kiyoku, Yasunobu Sugimoto, Tokuya Kozaki, Hitoshi Umemoto, Masahiko Sano, and Kazuyuki Chocho, "InGaN/GaN/AlGaN-based laser diodes with modulation-doped strained-layer superlattices grown on an epitaxially laterally overgrown GaN substrate", *Appl. Phys. Letters*, vol. 72, no. 2, pp. 211-213, 1998
67. Kazuhiko Nozawa, Yoshiji Horikoshi "Low Threading Dislocation Density GaAs on Si(100) with InGaAs/GaAs Strained-Layer Superlattice Grown by Migration-Enhanced Epitaxy", *Jpn. J. Appl. Phys.*, vol. 30. pp. 668-671, 1991
68. J. Yang, P. Bhattacharya and Z. Mi, "High-performance $In_{0.5}Ga_{0.5}As$/GaAs quantum-dot lasers on silicon with multiple-layer quantum-dot defect filters," *IEEE Trans. Electron. Dev.*, vol. 54, no. 11, pp. 2849–2855, 2007S

Chapter 2

Experimental Method

In the III–V laser device fabrication process, Molecular Beam Epitaxy (MBE), Atomic Force Microscopy (AFM), Transmission Electron Microscopy (TEM), X-Ray Diffraction (XRD), Photoluminescence (PL) and Electroluminescent (EL) have been used during PhD period. The samples were processed in London Centre for Nanotechnology (LCN) cleanroom, which consists of the etching, metallisation, photolithography and other laser processing. In this chapter, the equipment which include growth, characteristic measurement and device fabrication will be introduced in details.

2.1 Molecular Beam Epitaxy Growth

2.1.1 Molecular Beam Epitaxy System

Molecular beam epitaxy is a physical epitaxial growth method which implements molecule beam by heating the high purity (99.99999%) materials at particular temperature, so that the flux of beam, i.e., growth rate could be controlled precisely. MBE was first developed in the 1970s [1]. Compared with MOCVD, MBE does not only offer high precision control of the layer composition and thickness, but also provides high quality materials, especially for Al-containing III–V compounds. MBE works under ultra-high vacuum (UHV, 10^{-9} Torr) condition, which is obtained by using high power cryogenic pump (cryopump), ion pump and titanium sublimation pump. In general, a MBE system has three main chambers, loadlock chamber, buffer chamber and growth chamber. Loadlock and buffer chamber could store the wafers and bake them to different temperatures to degas of 200 ºC and 600 ºC respectively. The vacuum level of the loadlock chamber is slightly lower than the growth chamber, which is around 10^{-8}

Torr. There is a vacuum valve between the buffer chamber and the loadlock chamber and also between the growth chamber and buffer chamber.

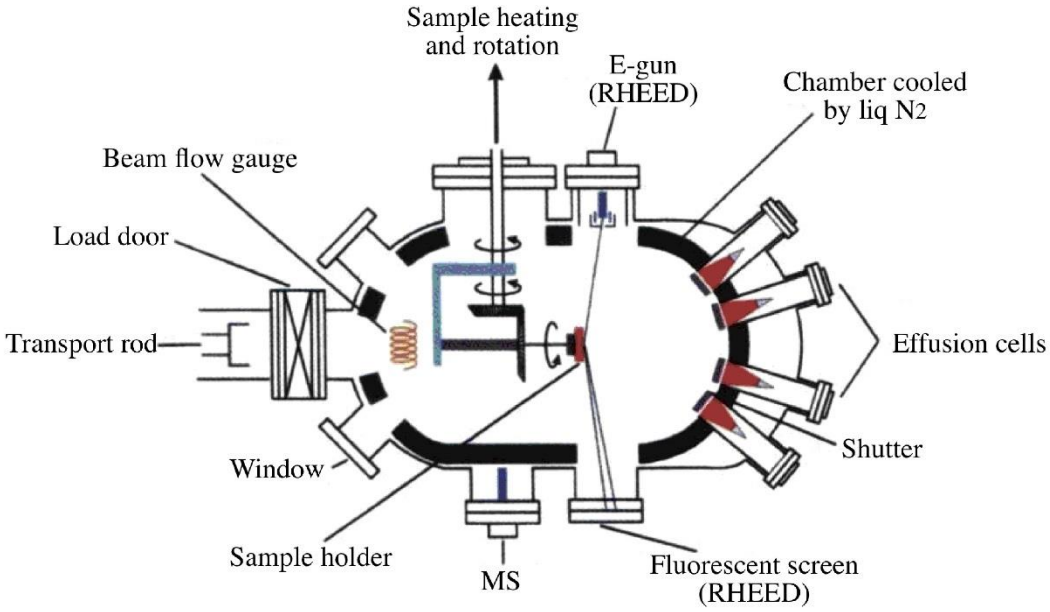

Figure 2.1. Schematic diagram of growth chamber for MBE system, which has detailed components including effusion cells, shutters, RHEED, window, sample holder, CAR system etc [3].

A schematic diagram of MBE system has been shown in Figure 2.1. In Veeco GEN-930 MBE system, nine effusion cells and two doping cells are filled with Gallium, Aluminium, Indium, Antimony, Phosphorus, Arsenic, Silicon and Beryllium, respectively. Reflective high-energy electron diffraction (RHEED) with fluorescent screen could examine the surface growth. Continuous azimuthal rotation (CAR) controls the wafer position in the chamber for growth, exchange, and calibration for beam flux gauge [2].

Figure 2.2 Veeco GEN 930 MBE system with phosphorus recovery system. Three chambers include loadlock, buffer and growth chamber. Cryopump and Turbo pump connected to loadlock chamber to vent and separate ion pump working on buffer and growth chamber. The growth chamber is kept at UHV condition by cryopump and ion pump.

2.1.2 Veeco GEN 930 Molecular Beam Epitaxy

We use Veeco GEN 930 MBE system which has four sections, growth chamber, buffer chamber, loadlock chamber and phosphorus recovery system. Figure 2.2 shows our Veeco GEN 930 MBE system in the cleanroom. The phosphorus recovery system is pumped by a turbo and scroll pump and cooled by liquid nitrogen (LN2). There is a vacuum valve between the main chamber and phosphorus recovery system. In this system, the machine is controlled by the operating system Molly developed by Veeco company.

2.1.2.1 Loadlock Chamber

In the loadlock chamber, turbo pump and cryopump combine with scroll pump, which could vent loadlock chamber to 10^{-9} Torr. The turbo pump and scroll pump could pump the loadlock chamber from atmosphere to 10^{-8} Torr level, while cryopump push the vacuum level to 10^{-9} Torr. The loadlock chamber can be exposed to the air during the sample exchanging. A UHV valve has been set between the loadlock chamber and buffer chamber. The valve uses the metal-

to-metal contact, which achieves the ultra-high vacuum condition in the buffer chamber (10^{-11} Torr at best). One Ion Pump is connected to the buffer chamber to maintain the vacuum level in buffer chamber. There is a heating station in the buffer chamber which could be used to degas the wafers up to 600 ºC.

A trolley, which has 8 spaces for 3-inch wafer is located in the loadlock chamber. The hatch door that contacts to air has an O-ring seal which can be baked to 200 ˚C and a copper gasket (10 inch) and standard blank flange are used to seal the quick hatch port. The loadlock chamber are used for outgas purpose and it can be heated by internal quartz lamps. The condition to bake the sample in loadlock chamber is 200 ˚C for more than 10 hours.

2.1.2.2 Buffer Chamber

One of the main function of buffer chamber is to isolate the UHV growth chamber and loadlock. Indeed, buffer chamber does the positive job to reduce the contaminations introduced to growth chamber from loadlock chamber because the loadlock chamber is kept at lower vacuum condition around 10^{-8} Torr and open to air during the sample changing.

It can also be used to store the degassed wafers and the inside trolley can store 16 wafers maximum. The buffer chamber has a heating stage which can heat and degas the wafer up to 600 °C. One residual gas analyser (RGA) is used to detect the gas molecules in the buffer chamber to examine contaminations during the period of degassing the wafers. To keep the UHV condition in buffer chamber, one ion pump is connected to the buffer chamber.

2.1.2.3 Growth Chamber

The growth chamber could ultimately reach the vacuum at 5×10^{-11} Torr level with CT-8 cryopump and at 5×10^{-10} Torr with turbo pump, Ion pump and scroll pump. To monitor the chamber condition, a RGA and ion gauge has been connected to the chamber. A RHEED gun and phosphorus screen are connected to the chamber to examine the growth performance. The phosphorus screen is covered with metal in case arsenic coating. An infrared pyrometer is detecting the substrate temperature which is independent from the thermocouple in the continuous azimuthal rotation (CAR). The pyrometer is normally working at high temperature (>400 ˚C). Under the working temperature of pyrometer, only thermal couple can tell the

temperature to operators. The wafer is located and controlled by CAR which will be explained in section 2.1.2.5.

In the Veeco GEN-930 MBE system, there are 11 cells, including two gallium sources, two indium sources, two aluminium sources, and three group V cells (phosphorus, arsenic and antimony). Each effusion cell has a shutter to control the flux on and off. Also in Veeco Gen 930, there is a main shutter which can stop all cells' flux. Due to the phosphorus can be explosive when the chamber opens to air, so a phosphorus recovery system has been designed by using high power pump and temperature difference to extract phosphorus from the growth chamber.

2.1.2.4 Effusion Cells and crackers

The effusion cells are face to the substrate during the growth with 30º. Each effusion cell contains high purity material with single element like gallium or indium. For III–V material MBE system, the effusion cells could have boron, gallium, indium, aluminium, and thallium. For the group III cell, the materials are contained in cells, with a shutter to control the on and off. However, group V materials need a cracker and bulk to control the temperature and a valve to adjust the flux of beam. The growth rate is controlled by both the temperature and valve of cells for group V materials.

The effusion cell has a head assembly that contains the crucible, which shown in Figure 2.3. The cell is heated electrically through the power and thermocouple connectors. The high purity material is contained within the crucible, which is made of pyrolytic boron nitride, tantalum, titanium, beryllium or quartz. The gallium and aluminium could destroy the crucible when the gallium and aluminium solidify.

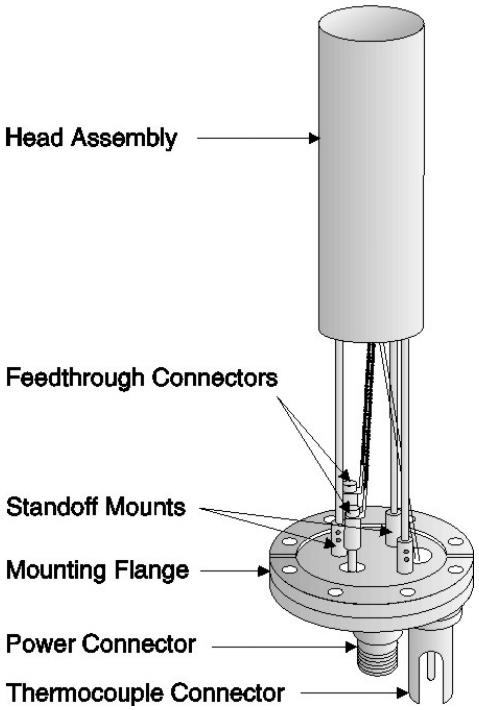

Figure 2.3 Effusion cell of group III material with dual filament. The cell connects with the power and thermocouple connector [4].

Arsenic cell has a zone which is used to crack the material in high temperature (Figure 2.4). The cracker could help Arsenic, Phosphor and Antimony to exchange between As_2 and As_4, Sb_2 and Sb_4, P_2 and P_4. The cell has bulk zone and cracking zone. The bulk zones store the large volume of the charge material and surrounded by cooling water for heat dissipation. The inside of bulk zone is crucible which assemblies with resistively heated filament. A refractory metal conductance tube is located in the cracking zone and a replaceable nozzle is used to improve the cracking efficiency uniformity. Both cracking and bulk zones are all controlled and monitored by thermocouple.

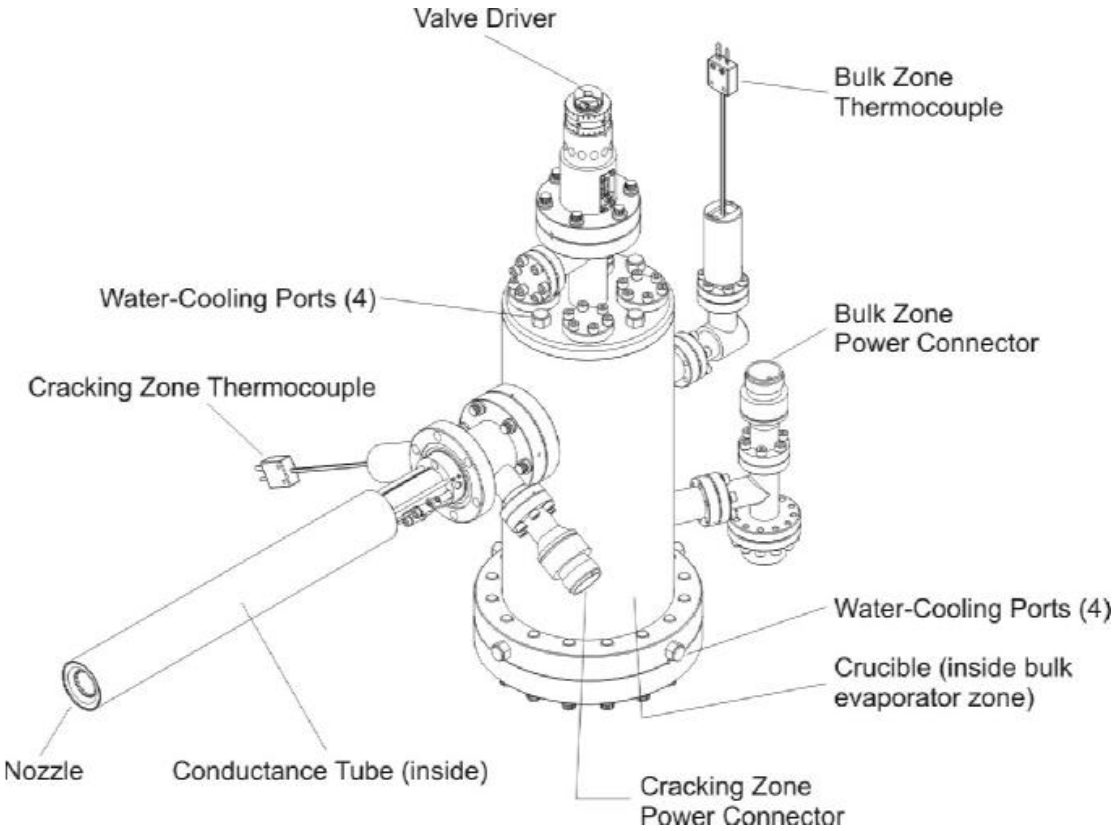

Figure 2.4 500cc Mark V arsenic valve cracker with bulk and cracking zone temperature controlled by thermocouple. [5]

2.1.2.5 Continuous Azimuthal Rotation (CAR)

The sample holder is controlled by CAR, which could ensure the sample is rotating clockwise or counter-clockwise during the growth and face different directions in the chamber as for various purposes, including loading wafers, measuring the flux and growth. The two rotations of substrate are controlled by two separate two motors. Behind the sample holder is the beam flux gauge, which can calibrate the growth rate.

2.1.2.6 Phosphorus Recovery System

The presence of phosphorus is the main issue of silicon-based growth because phosphorus could easily destroy silicon surface so as arsenic to germanium [6]. Moreover, phosphorus is dangerous when then chamber opens to air during maintance. The immediately react with oxygen will cause fire. However, cryopump does not have the function to pump phosphorus so that a secondary turbo pump and scroll pump are used here. During the growth period, the growth chamber is cooled by LN2 at -140 °C. After the growth, a small chamber named Phosphorous Recovery System is cooled by LN2 at -90 °C and growth chamber will be warmed

to room temperature, with opening a UHV valve between the growth chamber and phosphorus recovery chamber. Most of the phosphorus is vented into Phosphorous Recovery System, and react with oxygen and nitrogen for disposable purpose in the later stage.

2.1.2.7 Reflective High Energy Electron Diffraction

In the growth chamber, reflective high-energy electron diffraction (RHEED) is used to monitor the atomic surface reconstruction. The phosphorus screen could display the RHEED by showing its pattern. The patterns of RHEED show the surface of growing sample, as shown in Figure 2.5a. The RHEED also could be used to calibrate the growth rate by examining the intensity of RHEED in a particular point on the screen. In the rough surface, more scattered electron beams are observed by phosphorus screen like Figure 2.6. During the cycle of homoepitaxy growth, the formation of one monolayer could observe from the RHEED pattern. Moreover, RHEED patterns are also variable with the temperature change due to the surface reconstruction change at different temperature.

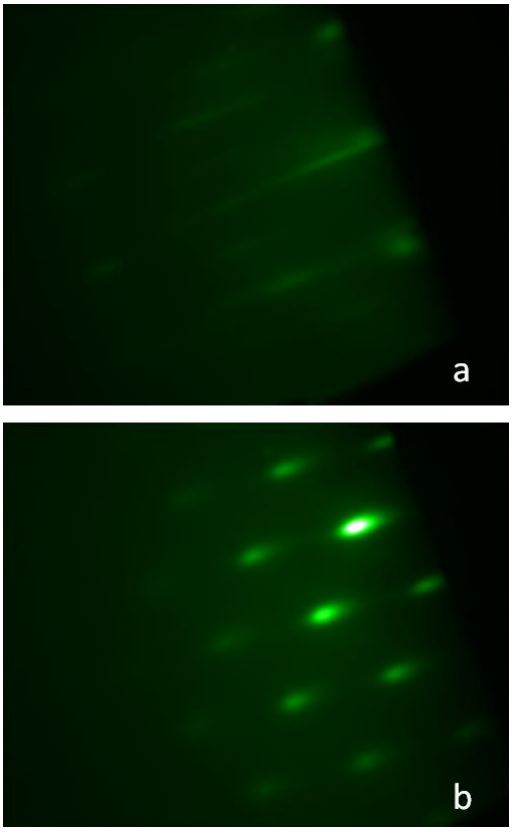

Figure 2.5 RHEED pattern with different materials and surface morphologies: a, smooth surface GaAs on Si with 4-bys patterns; b, InAs/GaAs QDs with sharp pattern due the 3-D physical shape of QDs

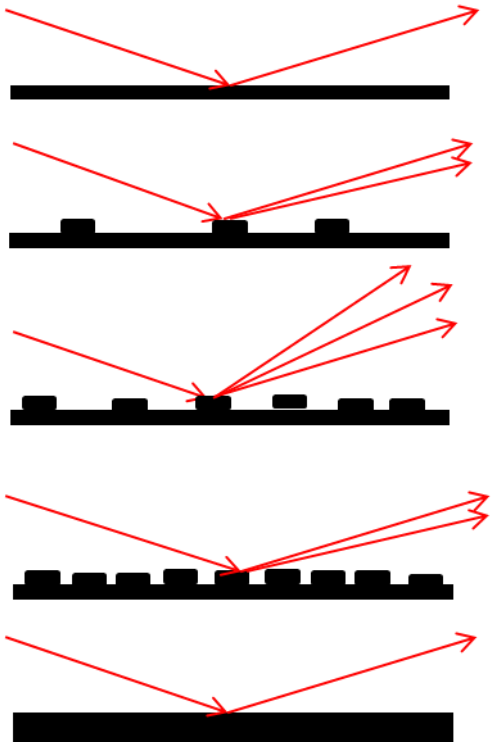

Figure 2.6 The variation of RHEED gun beam spotted on a growing surface, that surface is growing layer by layer and induced RHEED beam diffraction. Between the growths of each layer, a pattern changing from unfocused to focus could be obtained from the phosphorus screen.

2.1.2.8 Ultra High Vacuum Pumping System

Ultra-high vacuum in MBE system could ensure that low impurity background concentration to 10^{-14} cm^{-3}, which ensure the devices to work at high performance [7]. In order to keep the high vacuum condition for MBE system, we use ion pump, titanium sublimation pump, scroll pump, turbo pump and cryopump together in our MBE system.

Ion Pump and Titanium Sublimation Pump

For III–V material growth, different types of gas species are captured chemically or physically by different types of pumps such as ion pump and Ti sublimation pump (TSP). The principle of ion pump is using ion to trap the gas particle (oxygen, nitrogen...) in the vacuum condition into titanium film, which provides a continuously active pumping surface. So ion pump and TSP are perfect for the keeping of UHV condition but cannot pumping the chamber to UHV from low vacuum efficiently.

In the GEN930 MBE system, we have two ion pumps and TSPs connected to buffer chamber and growth chamber separately. Buffer chamber needs ion pump and TSP to absorb the gas molecule from the buffer stage which the wafer degas.

Scroll Pump and Turbo Pump

In the MBE system, scroll pump normally connects with turbo pump together to pumping the chamber from atmosphere to 10^{-8} Torr level. During the pumping, the scroll pump will start first and pump the chamber to 10^{-2} bar and the turbo increases the vacuum level to 10^{-8} bar. The scroll pump operating in reverse is known as a scroll expander, and can be used to generate mechanical work from the expansion of a fluid, compressed air or gas.

Cryogenic Pump

The cryogenic pump or cryopump could vacuum the chamber to UHV condition. A helium compressor and cold head are inside the cryopump. The compressor is located remotely from the cryopump cold head that is mounted to the vacuum chamber. Helium-filled connecting lines link the cold head and compressor together. As a part of two-stage oscillation displacer, the cold head has the shape of cylinder which allows high pressure ambient temperature gas pass. The cryopump could regenerate when the displacer return stroke, a high pressure side valve closes and a low pressure side valve opens to allow the expansion of Helium through the regenerator material thereby cooling it.

2.1.3 The Mechanisms of Molecular Beam Epitaxy Growth

As a method of material deposition, MBE deposits material by very precise control. The atomic layer is formed by the beam flux deposition. The atoms formed layer by layer on a substrate, as shown in Figure 2.7. For the homo-epitaxy growth, the layer is formed with 2D-by-2D because there is no lattice difference. There are three types of growth method, Frank van der Merwe, Stranski-Krastanov and Wolmer-Weber growth, corresponding to layer-by-layer, layer-by-island and island-by-island, as shown in Figure 2.8. Homo-epitaxy growth is the type of layer-by-layer, which corresponding to Frank-van-der Merwe mode. During the Frank-van-der Merwe mode growth, the atoms are absorbed on the substrate and migrate until meet a step edge where the potential energy is minimised. [8] InAs/GaAs Quantum dots are formed with Stranski-Krastanov mode, because the strain between InAs and GaAs could form island once

the strain force arrives critical point [9]. Wolmer-Weber island growth is the model of island-by-island growth.

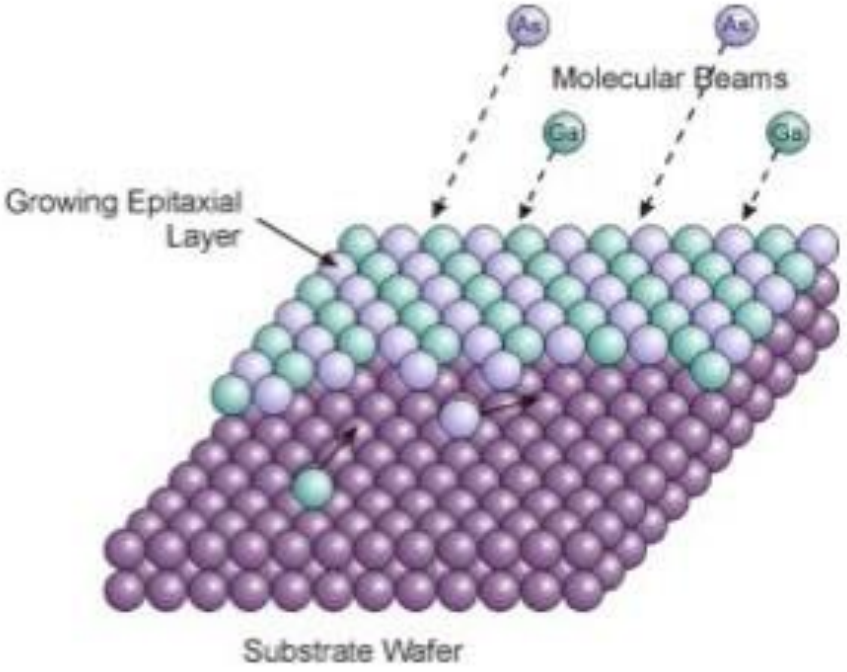

Figure 2.7 Schematic diagram of MBE growth layer by layer. The atoms spotted on the sample surface and formed layer under the molecular beam pressure and substrate temperature [10].

Figure 2.8 Three growth modes, Frank van der Merwe, Stranski-Krastanov and Wolmer-Weber growth which correspond to 2D-to-2D, 2D-to-3D, and 3D-to-3D growth.

Solid-Vapour Equilibrium for Binary Compounds

As the most frequent material used in MBE system, GaAs layer is formed by Ga atoms and As_2 or As_4. The reaction formula is,

$$Ga(g) + \frac{1}{2}\, As_2(g) \rightleftharpoons GaAs\ (s)$$

$$As_2(g) \leftrightharpoons As_4(g) \qquad \text{Equation 2.1}$$

Where Ga and As are in gas phase in the UHV system but GaAs is in solid phase. The equilibrium constant is induced during the growth, which defined as

$$K_i = \exp\left(\frac{\Delta S}{k}\right)\exp\left(\frac{-\Delta H}{kT}\right) = K^{0i}\left(\frac{-\Delta H}{kT}\right) \qquad \text{Equation 2.2}$$

Where ΔS is the change in entropy associated with the reaction, ΔH is the entropy of the reaction, k is Boltzmann constant. The equilibrium constant represents the composition of the system at equilibrium. It could be assumed, the nucleation of GaAs on substrate depends on the substrate temperature. However, during the nucleation process, part of III–V material could sublimate when the temperature condition makes the reaction reversible. The high V/III ratio could inhibit the effect of sublimation regarding to H. Seki *et al* [11]. As H. Seki mentioned, in the binary compounds, by considering the equilibrium partial pressure of group III material, the order for the sublimation temperature is

AlP > AlAs > GaAs > GaP > GaSb > InAs > InP > InSb [12]

Which means in the III–V heterostructure growth, the temperature is important. The The group III material growth rate has been described as Hertz-Knudsen equation,

$$r = \alpha \frac{V_c(P_{III}^0 - P_{III})}{\sqrt{2\pi mkT}} \qquad \text{Equation 2.3}$$

Where α is the sticking coefficient, V_c is the volume of a molecule of the growing crystal, P_{III}^0 and P_{III} are the pressure of the group III element incident on the substrate surface and the equilibrium partial pressure at the substrate surface, m is the molecular mass, k is the Boltazmann constant and T is the absolute temperature.

2.1.4 MBE Operation

2.1.4.1 Calibration

The calibration of MBE determines the accuracy of growth rate and it effects on the device performance. In the MBE system, the calibration includes temperature and growth rate.

There is an infrared temperature sensor to detect the temperature of wafer during the growth, which could have different reading from the temperature feedback from the thermal couple based on CAR. We use GaAs wafer oxidation temperature (580 ºC ±10) to determine the real temperature [13]. RHEED helps to observe the substrate dioxide progress with pattern change

from rough to sharp (figure 2.5). Because the possible reconstruction of GaAs are (2 × 4), (4 × 2) and c(4 × 4) [14], RHEED pattern will shows the 4 bys (figure 2.5a) which is able to examine the surface morphology. To calibrate the growth rate of Ga, Al and In sources, GaAs, AlAs and InAs are homoepitaxy grown on their corresponding substrates. Based on RHEED pattern and oscillation cycle, we could calculate the growth rate as figure 2.6 shows.

2.1.4.2 Sample Preparation

The epi-ready wafers are fixed at the sample holder that contains Mo and Nb. The sample holder is particular designed to fit Veeco MBE system without indium bonding [14]. The sample holder could fix 3 inch and 2 inch wafers. A 4-inch wafer need to be cut to quarter to fit in the particular holder, as shown in Figure 2.9.

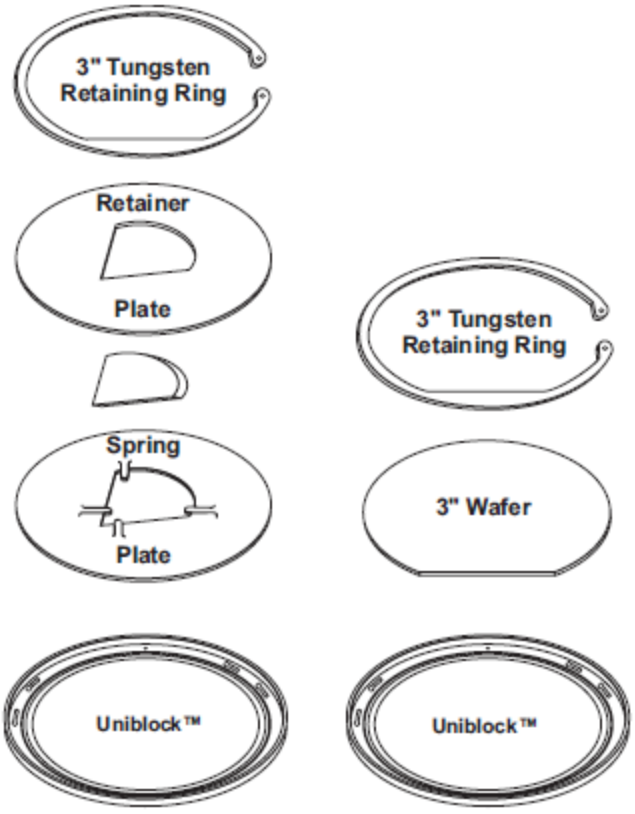

Figure 2.9 Standard configuration for whole and partial wafers based on Veeco sample holder.

The sample will be degassed at 200 ˚C for 12 hours at loadlock chamber. Loadlock chamber could degas 8 wafers maximum in one time which locates in one trolley. After the first low temperature degas, the samples are moved to buffer chamber and further degassed on the buffer stage at 400 ˚C for around 2 hours. Then it is ready to be deoxidized in the growth chamber.

For Si wafer, the substrate will be heat up to 1000 ˚C and for 20 minutes and for GaAs wafer, As valve need to be open once temperature over 500 ˚C and heat up to 580 ˚C for 8 minutes.

2.1.4.3 Sample Growth Controlled by Software Molly

To arrange the growth procedure, a receipt needs to be written in the MBE operating system - Molly. The Molly software automates the growth process by working from a recipe file, which describes the desired epitaxial layer structure to be grown. Moreover, manually control and override capabilities, data trending and logging to disk and simple but comprehensive system configuration and calibration are provided by Molly.

2.2 Atomic Force Microscopy

In order to examine the morphology of MBE grown sample, atomic force microscopy (AFM) has been used. Compare with other electron microscopy, AFM could provide a 3-dimension scan, which means, the roughness and attitude could be provided by AFM measurement. Figure 2.10 shows the AFM images with 3-D InAs/GaAs QDs.

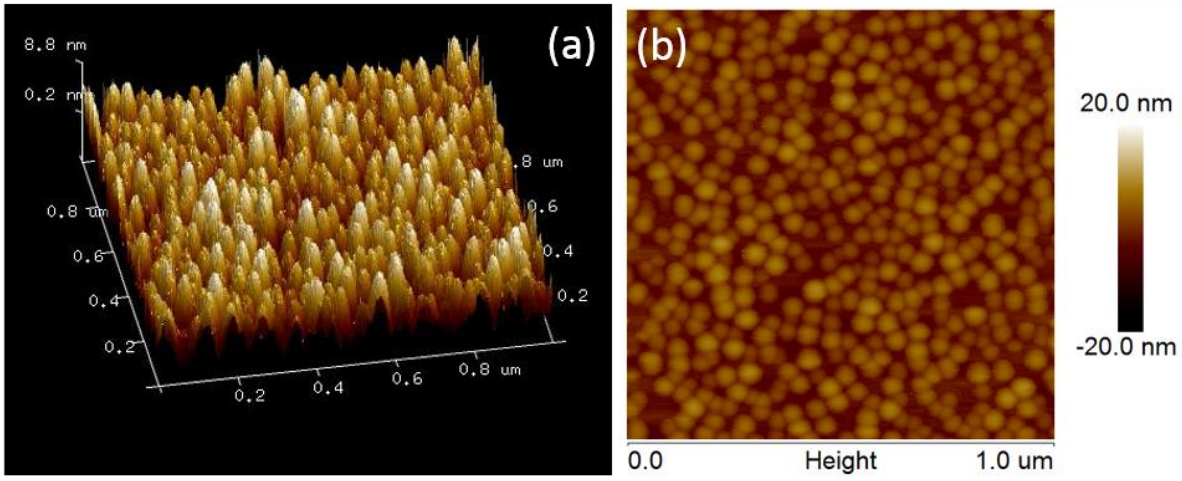

Figure 2.10 (a), Three dimensional 1 μm^2 AFM image of InAs/GaAs quantum dots grown on Si substrate. The QDs are 3-D in physical dimension with height range around 7 to 8 nm. (b)Two dimensional 1 μm^2 AFM image of InAs/GaAs quantum dots on Si substrate. The colour bar scales the height.

The basic AFM scanning has two modes, contact and non-contact. The mechanism of AFM is based on the atomic force between the cantilevers and samples. As shown in Figure 2.11, a laser beam is reflected at the top point of tip, and received by a photodiode, which is used to

measure the amplitude of vibration of tip. In the contact mode, the tip is scanning on the surface as the cantilever moving horizontally. In the non-contact mode, an electrical force has applied to cantilever and introduced a controllable frequent vibration. There is a small gap between the tip and sample surface, which allows the tip to sense the atomic force and reduce the abrasion on the tip. The AFM tip has a needle-shape with 10 – 15 μ m length, which has proved by SEM image in Figure 2.12.

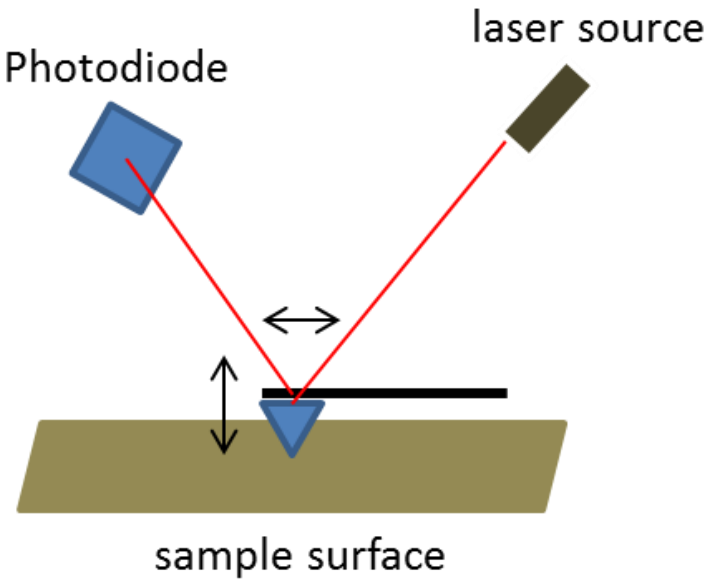

Figure 2.11 Schematic diagram of AFM. A laser source directly shot on the back side of cantilever which could vibrate during the scanning and the laser source reflected to photodiode to analysis the morphology. The cantilever could move forward and backward to contribute the trace and re-trace.

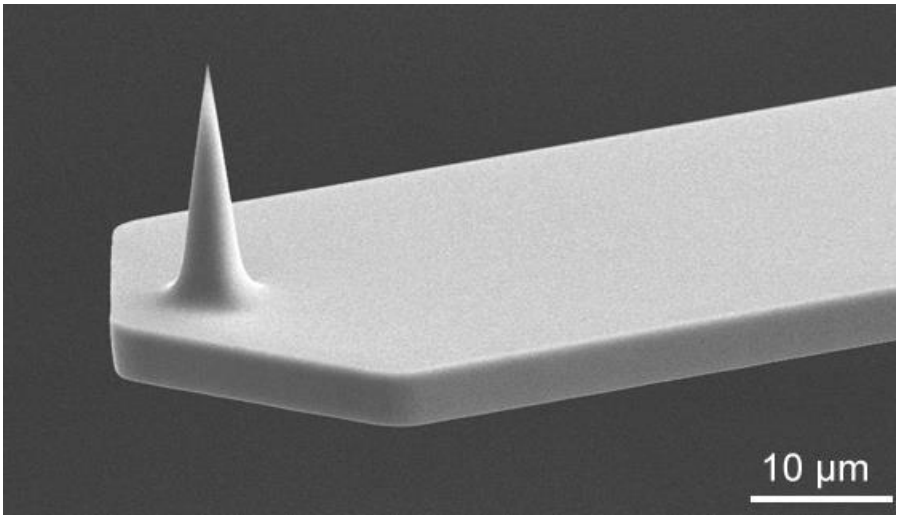

Figure 2.12 SEM image of AFM cantilever with blend tip on top. The tip is dedicated and easy to be broken. The AFM non-contact mode uses high frequency vibration on cantilever and keeps a short distance between sample and tip.

AFM is also compatible with other characteristic measurement equipments for example Raman spectroscopy, which helps to measure the Raman spectrum at a particular position on the sample.

In this project, the QD samples used to be measured by AFM were grown by MBE. One layer of QD grown on the top of calibration sample with lower thickness of cladding and 5 layers of DWELL structure. The top layer of QD will present same quality as the DWELL embedded within the cladding layer.

2.3 Photoluminescence

Photoluminescence (PL) is a straightforward method to measure the material quality by receiving a wavelength spectrum. By exciting a high power laser beam whose wavelength shorter than the energy bandgap of sample, for instance, a 532 nm green laser excited the InAs/GaAs QDs with GaAs bandgap (860 nm) at room temperature as Figure 2.13. The procedure of carriers' transaction from valance band of GaAs to InAs QDs valance band including photoexcitation, relaxation and radiative recombination.

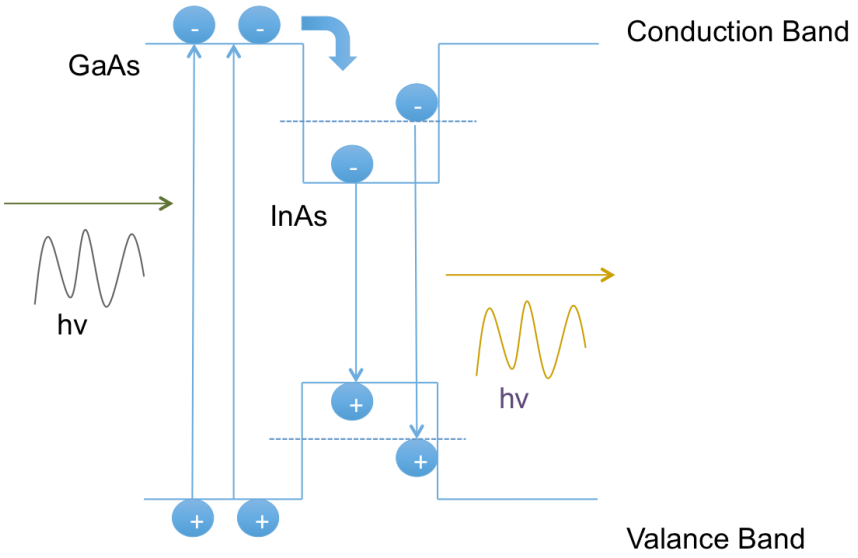

Figure 2.13 InAs/GaAs QDs bandgap structure with a stimulated photons injection and spontaneously photons emission. The carriers in GaAs were excited by the photon input and transmit to InAs QDs cause radiative recombination.

The spectrum could illustrate the emission wavelength, the intensity of spectrum, bandwidth of emission and different performance from low temperature (~10 K) to high temperature (~300 K). In the temperature dependent PL measurement, not only excitation energy could be calculated, the crystal quality can also be examined. For example, in Figure 2.14, the temperature dependent PL spectra show the clear trend of blueshift from high temperature (300 K) to low temperature (10 K).

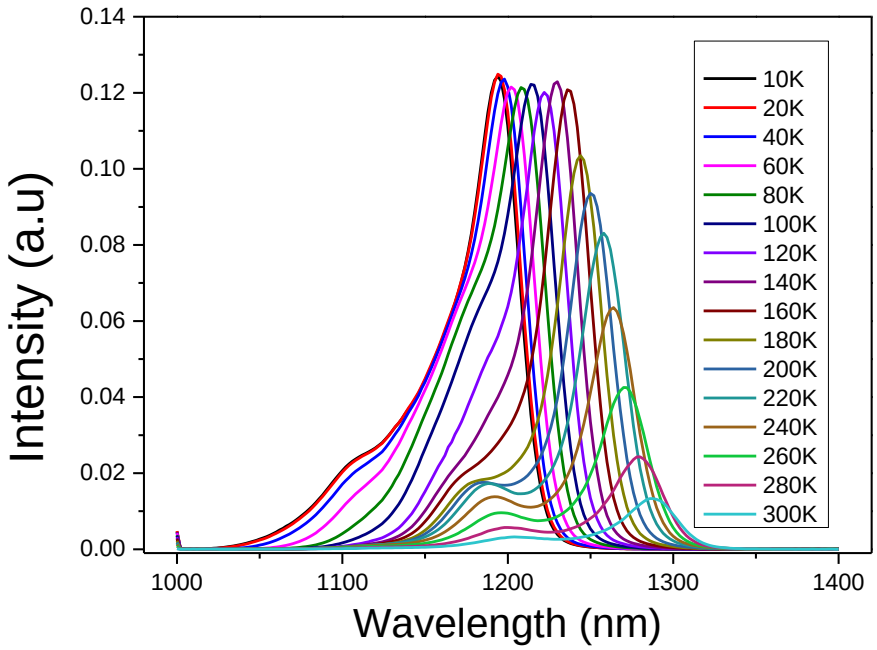

Figure 2.14 Temperature dependent PL spectra of InAs/GaAs quantum dots monolithically grown on a Si substrate.

As shown in Figure 2.15, a 532-nm green laser has been used to excite the PL sample which is pasted on a temperature controlled copper plate. The power of 532-nm laser is around 100 mW and various ND filters are applied to obtain different power density for PL measurement. Sample holder is located in a vacuum chamber, which pumped with 1500 Hz rotation speed turbo and compressed with liquid helium to 10 K temperature could be achieved with proportional-integral-derivative (PID) controller. Two lenses have been used to focus the beam emission from sample, which followed by a monochromator. An optical chopper synchronises the frequency with sampling frequency. An adjustable slit is behind the chopper and followed with few mirrors to extend the optical route. Figure 2.16 present three types of detectors are prepared, Si Ge and InGaAs which cover from visible to 1700 nm wavelength range. The signals from detectors were transmitted to lock-in and computer where the spectrum presented.

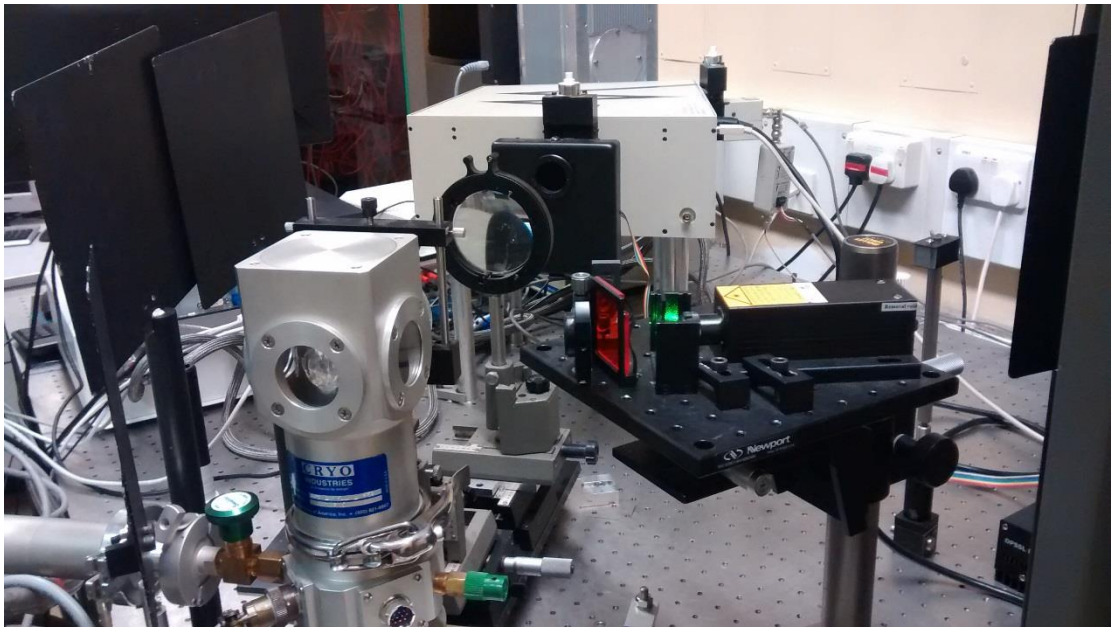

Figure 2.15 Photo of temperature dependent PL setup. The green laser emits a 532-nm beam onto the sample which is located in the thermal copper pad controlled by temperature PID controller. The cooling system is under the vacuum system, which is maintained by a 1500 Hz rotation pump and inside cryopanel connects to a liquid helium compressor. Two lenses focused the photons emitted from the sample and transmitted to detector.

Another PL setup, RPM-2000 (Figure 2.17), could measure the PL map of whole 6-inch wafers. The optical route is fixed in the package and two detectors, with one InGaAs detector and one CCD to cover from visible to 2.1 μm wavelength range. RMP-2000 has a white light source inside but also one 635-nm laser. Based on the PL mapping result, the quality of whole wafer can be observed.

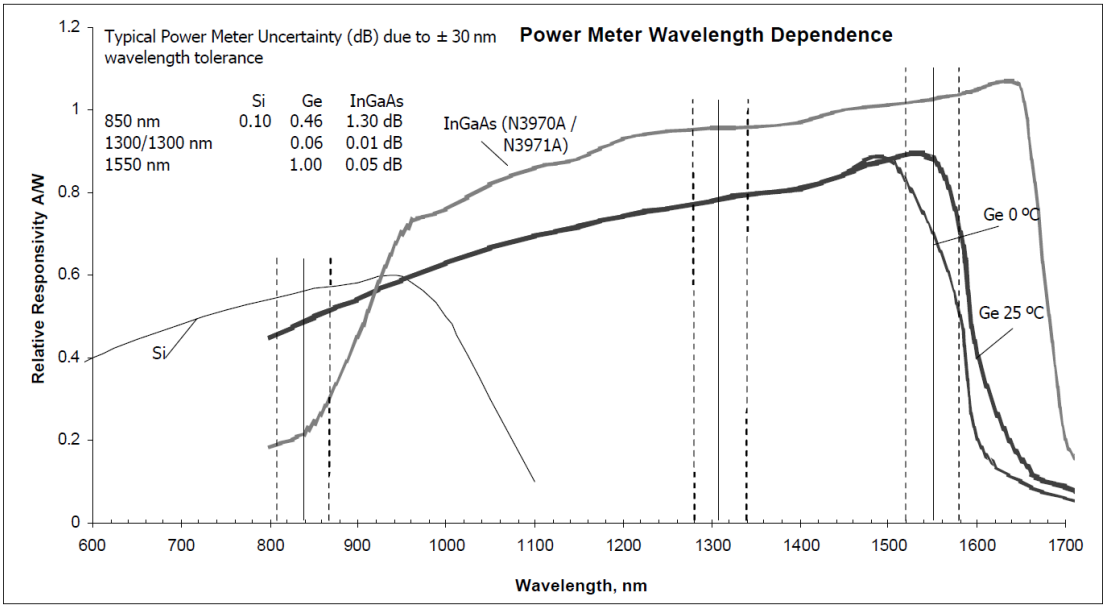

Figure 2.16 Response spectrum of Si, Ge and InGaAs photodetector, where Si detector covers the wavelength from visible range to around 1100 nm, Ge detector covers the wavelength from 900 nm to around 1600 nm and InGaAs could able to cover further until 2.1 µm.

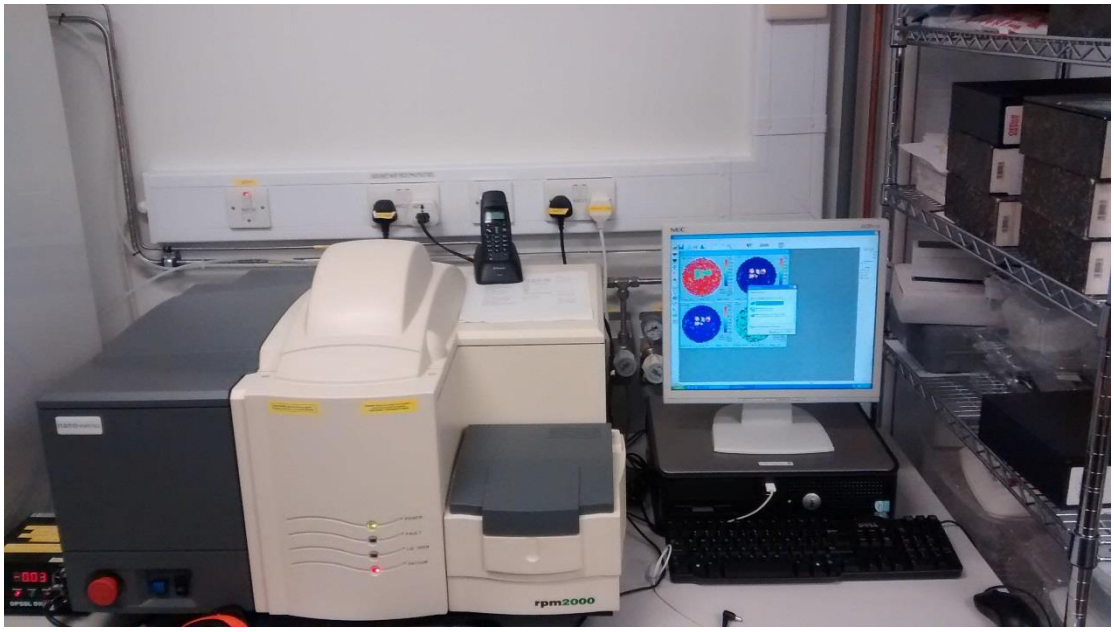

Figure 2.17 RPM-2000 PL setup with function of wafer mapping PL measurement and fixed optical route.

2.4 X-Ray Diffraction system

In the III–V material growth, trimetric and tetrameric crystals like InGaAs, InAlAs are used frequently. However the lattice constant and bandgap energy in $A_xB_{(1-x)}C$ (x: 0 - 1) and $A_xB_yC_{(1-x-y)}D$ (x, y: 0 - 1) is identical with the value of x for instance, $In_xGa_{(1-x)}As$, $In_xGa_yAl_{(1-x-y)}As$, which means it is necessary to examine the composition of element A, B and C in compounds. High Resolution X-Ray Diffraction (XRD) can achieve the analysis of crystal epitaxy layer thickness, composition, strain and relaxation. During the measurement, an X-Ray beam shot on the sample surface with angle θ and a detector receive the signal (Figure 2.18).

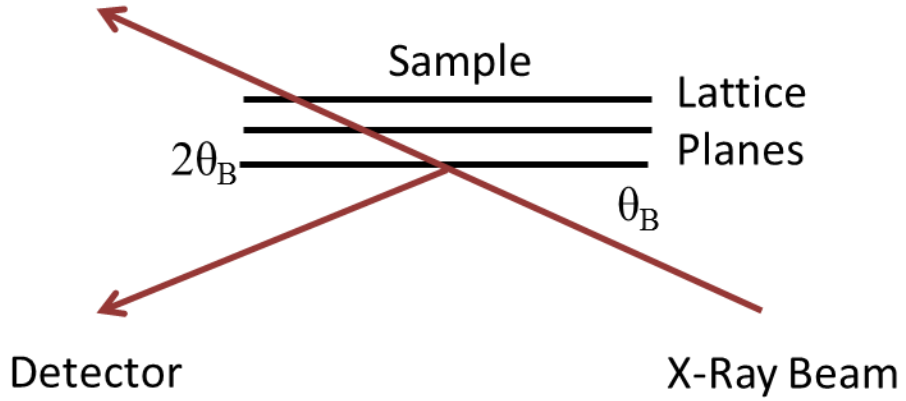

Figure 2.18 Schematic diagram of XRD with θ_B angle X-Ray beam on the sample. The different thickness of sample will correspond to the particular wavelength of X-Ray beam.

To analyse the crystal, XRD releases a high energy X-Ray beam with the angle of θ to the sample surface (normally wafer). The X-Ray diffraction obeys the Bragg law

$$2d\,(\sin\theta) = \lambda$$

where d is the inter spacing of each layer of crystal and λ is the wavelength of X-Ray. The HRXRD system we use is Bede D1 XRD (Figure 2.19) manufactured by Jordan Valley Semiconductor Ltd. The functions of Bede D1 are controlled by Bede control software.

Figure 2.19 Bede D1 XRD system.

2.5 Transmission Electron Microscopy

TEM is a microscopy technique which using electron beam to shine through the sample. The image is formed by the interaction (scattering) of electrons and atoms. A fluorescent screen used to display the image. In general, TEM has stronger capability to measure the sample with lower magnitude than AFM. Atomic structure can be clearly observed with high resolution TEM (HRTEM). Also there are two modes of TEM called dark field and bright field by applying different aperture position before the image and direction of incident beam.

2.5.1 Layout of TEM

The TEM system is running under vacuum condition (10^{-4} Pa) to increase the mean free path of electron gas interaction. The vacuum condition also forbids the appearance of electric arc between the high voltage from cathode and ground. There are two types of electron gun can be used as electron sources, thermionic electron gun and field emission electron gun. Field emission electron gun could generate higher brightness than thermionic electron gun but it

requires higher vacuum condition as well. The brightness is defined by the beam current density in unit solid angle.

As shown in figure 2.20, the incident beam comes from electron gun and goes through the specimen, which allocated on the specimen stage. The interaction between electrons and atoms of specimen will create the diffraction beam and focus by the objective lens (magnetic) to form the diffraction pattern and image plane.

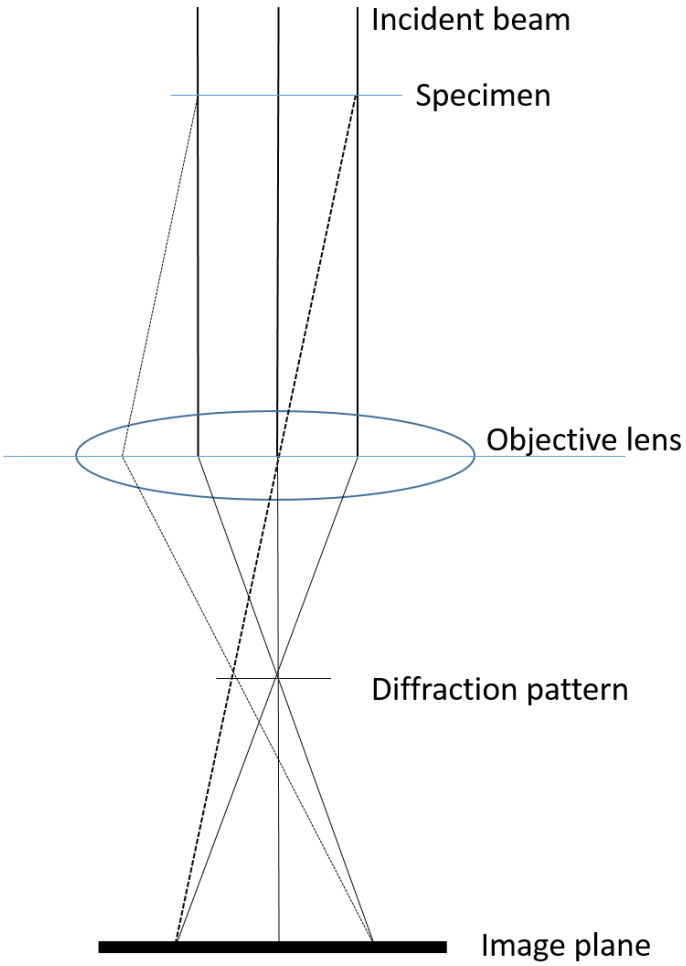

Figure 2.20 Layout of TEM

2.5.2 Dark Field, Bright Field and High Resolution TEM

The dark field and bright field TEM are basically two types of measurement with using aperture and different angle of incident beam. In the dark field images, the direct beam is blocked by the aperture which allows high angle interaction beam to be measured. It normally used to identify the crystal defects or particle size. For bright field, only direct interaction beam

allowed to go through the aperture. A larger size of aperture is used for high resolution TEM (HRTEM) which allows more beams to pass. HRTEM needs relative higher point solution with a well alignment of specimen, however atomic structure can be observed.

2.6 Device Processing

The laser device must be processed in clean room with numbers of steps. Generally speaking, for board-area Si based laser, silicon itself is not a good conductor as electrode, so top contact with both n and p type are applied in laser devices. The basic processes of laser device process could be illustrated as following orders.

1. Etch the ridges and contact
2. Use plasma-enhanced chemical vapour deposition (PECVD) to cover a SiO_2 layer to sample
3. Open n and p-type contact windows
4. Use evaporator to deposit n and p-type contacts
5. Use rapid thermal processing (RTP) to anneal the sample
6. Cleave the sample to laser bar
7. Use wire bonding or mounting laser

Cleaning

Before the processing start, laser sample need to be cleaned in with solution of acetone and iso-propanol (IPA) to reduce the contamination in the device. The contamination is undesired to laser processing. After the cleaning with acetone and IPA, the sample was put in ultrasonic bath for two minutes. After the ultrasonic bath, IPA and acetone were used again to clean to make sure no contamination left on surface and checked with microscope. The cleaning process must be repeated if any contamination is found on by microscope.

Patterning

To pattern the wafers, photolithography is used in the processing. Photoresist can decide the area exposed to the light or electron beams. During the patterning, Approximately 1.8 μm thickness of Shipley S1818 photoresist cover on sample and spin with 4,000 rpm for 30 seconds. The photoresist is dried with baking at 115 ºC for 60s. Microscope again used to examine the surface of sample.

Etching

To remove the region which not been covered by photoreisit, etching is using in the device fabrication. In the process of etching samples, wet etch and dry etch are used. Wet etch is using liquid solvent to remove the materials on the sample. Dry etch is using plsama-drive machine by exposure sample to a bombardment of ions. Wet etching could provide the removal of material on two direction, vertically and horziontally, so the controlling of etching time need to be precesily. To compare with these two etching methods, a table has been give.

Dry Etch	Wet Etch
Complicated operation	Ease to use
Cost high	Cost low
More reliable, repeatable	No damage to substrate

Table 2.1 The comparsion of dry etch and wet etch.

In the wet etch process, due to the different material properties between each III–V material, using different kinds of solvent are needed to etch down GaAs and AlGaAs. The solvent is mixed with 1:1:x H_3PO_4:H_2O_2:H_2O where x is 3, 5 and 10.

Metallisation

The metal of GaAs contact layer could be depositied by E-beam evaportor, thermal evaportor and sputter. We use InGe/Au for n contact layer which has exposed under the active region for Si-based laser. The p contact layer is Ti/Pt/Au and annealled by Rapid Thermal Processing (RTP) for 5 seconds at 440 °C. Figure 2.21 shows the Si based laser bar with n and p contact layer on top with different length.

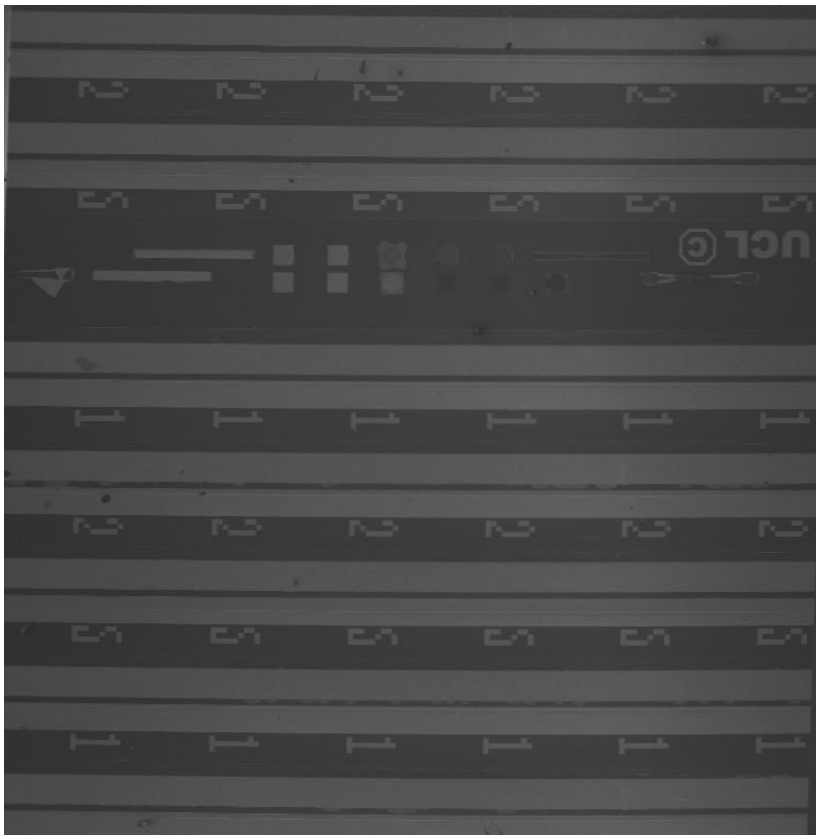

Figure 2.21 Scanning electron microscopy (SEM) image of laser devices with different size of optical cavity, which numbered on it. UCL logo is printed on the sample device

2.7 Laser Measurement

The cleaved laser needs to be tested in power-current (L-I) measurement and current-voltage (I-V) measurement to examine the laser performance. As shown in Figure 2.22 for the top contact laser devices, they are placed on a heat sink which controlled by thermoelectric cooling with temperature range 10 to 100 ºC. Then temperature sensor was mounted inside the heat sink. We implemented two probes to contact the p and n contact of laser devices. We have two operating modes which are pulsed and continuous-wave (CW). The pulsed current is operated by pulsed ILX Lightwave 3545B laser diode controller that is able to operate with duty cycle 0.01% to 0.1% and pulse widths of 0.1 μs up to 10 μs. The CW mode is operated by ILX Lightwave laser diode controller.

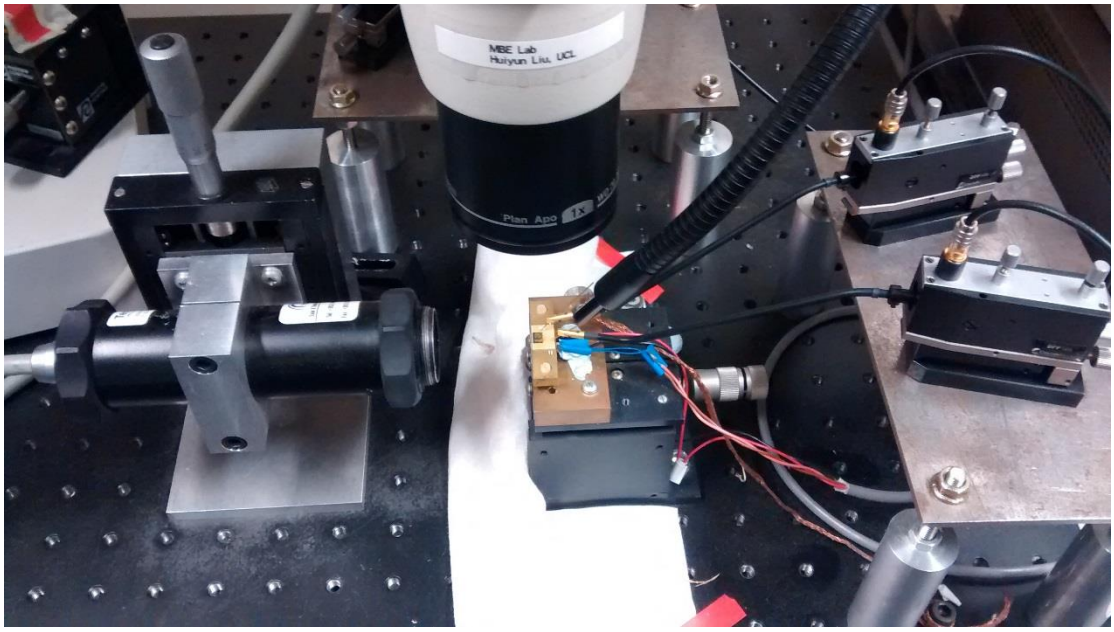

Figure 2.22 L-I measurement setup with a detector on the left side and monitored by microscopy. The laser devices placed on the copper heat sink with thermoelectric cooling.

2.8 Reproductivity of Experiments

During the experiments, there are three sections have been involved: MBE growth, cleanroom processing and characteristic measurements. MBE system has high reproductivity due to its precisely control of growth rate and ultra-high vacuum growth condition. The growth rate has been calibrated before every growth beginning. Also, MBE system has high uniformity to produce wafer in 3-inch scale. The laser devices are processing in the cleanroom as followed the same recipe. During the AFM measurements, the image I captured were all using the brand new AFM tip to guarantee the size of QDs are most accurately. The temperature dependent PL were measured under same laser excited power and other parameter were kept same only temperature differs and same as power dependent PL only laser excited power changes.

Reference

1. A. Cho and J. Arthur, “Molecular beam epitaxy”. *Progress in Solid State Chemistry*, vol. 10, pp. 157-191, 1975
2. N. N. Ledentsov, “Growth processes and surface phase equilibria in Molecular Beam Epitaxy”, *Springer-Verlag*, 1999
3. http://cnx.org/contents/1096167b-8518-4159-a88d-3b2ae4df6645@9.3:28/ Chemistry_of_Electronic_Material
4. GEN 930/ GEN II MBE System Operation Manual, Veeco

5. Arsenic Valved Cracking Effusion Cell 500cc Mark V User Guide, Veeco
6. Damien Bordel, Denis Guimard, Mohan Rajesh, Masao Nishioka, Emmanuel Augendre, Laurent Clavelier, and Yasuhiko Arakawa, "Growth of InAs/GaAs quantum dots on germanium-oninsulator-on-silicon (GeOI) substrate with high optical quality at room temperature in the 1.3 mm band", *Applied Physics Letters*, vol. 96, pp. 043101, 2010
7. Günther Bauer and Gunther Springholz, "Molecular beam epitaxy—aspects and applications," *Vacuum*, vol. 43, no. 5, pp. 357–365, 1992
8. F. C. Frank and Jan. H. van der Merwe, "One-dimensional dislocations. I. Static theory". *Proceedings of the Royal Society of London Series A Mathematical Physical Sciences,* vol. 198, no. 1053, pp.205-216, 1949
9. TR Ramachandran, R Heitz, P Chen, and A. Madhukar, "Mass transfer in Stranski–Krastanow growth of InAs on GaAs", *Applied Physics Letters*, vol. 70, pp. 640, 1997
10. http://www.ee.ucl.ac.uk/about/MBE
11. Hisashi SEKI, Akinori KOUKITLI, "Thermodynamic analysis of molecular beam epitaxy of III–V semiconductors", *Journal of Crystal growth*, vol. 78, pp. 342-352, 1986
12. Akinori KOUKITU, Yoshitugu HASEGAWA and Hisashi SEKI, "thermodynamic analysis of the moype and mbe growth of pentanary iii-v alloy semiconductors",
13. J. H. Neave and B. A. Joyce. "Structure and Stoichiometry of (100) GaAs surfaces during molecular beam epitaxy." *Journal of Crystal Growth*, vol. 44, no. 4, pp. 387-397, 1978
14. M. D. Pashley, "Electron counting model and its application to island structures on molecular-beam epitaxy grown GaAs(001) and ZnSe(001)," *Physical Review B*, vol. 40, pp. 10481, 1989
15. "Veeco UNI-Block: Excellent Performance and Convenience with a Non-Bonded Substrate Holder," *Veeco Application Note*, No. 3/96,1996

Chapter 3

InAlAs/GaAs Defect filter Layer

3.1 Introduction

As a future driving force, Si photonic will lead the optoelectronic industry without doubt. The optoelectronic integrated device on silicon platform is the main focal point for researchers. As a complete optoelectronic circuit, the components, such as Si-based light emitting source, modulator [1-3], waveguide [4] and detectors [5] are needed. However, the optoelectronic devices, especially light emitting device based on Si platform, have been considered as the "Holy Grail", because the difficulties are dramatically enhanced for group-IV platform in comparison with III–V platform [6]. Si and Ge are in-direct bandgap material, which means the low efficiency of photon emission with high ratio of Auger recombination and so that Si-based light emitting devices are hard to fabricate [7]. To solve the issue, III–V integration and Si Raman laser has been adopted by researchers. Although Si Raman Laser has been demonstrated with continuous-wave (CW) mode by H. Rong *et al* [8], the optical pumping operation leads to the difficulty of Si Raman laser apply in Si optoelectronic integration. Si hybrid laser has been assumed as one of the solution which using wafer bonding technique to combine III–V optoelectronic devices on Si or Silicon-on-insulator (SOI) platform [9, 10]. The advantage of Si hybrid laser is the combination of quantum well or quantum dot lasers with Si substrate and waveguide because SOI could be fabricated as a waveguide. Moreover bonding technique avoids the issue of high density of threading dislocations which propagated from heterostructure epitaxy growth [11, 12]. CW operation of Si hybrid laser has been well established since last 20 years [13]. However the optical output power and threshold current density (J_{th}) are significantly affected negatively compare with pure III–V optoelectronic device especially lasers [14]. Another method to solve the integration issue is using

monolithical growth of III–V material on Si substrate by molecular beam epitaxy (MBE) system or metal organic chemical vapour deposition (MOCVD) system [15]. There are also a few other depositions systems could able to achieve the III–V material on Si substrate like atomic layer deposition (ALD) [16]. However, the ultra-high vacuum environment and better monitor system, such as RHEED, of MBE offers better control of growth of III–V/Si interface, and hence is able to offer better the III–V devices performance monolithically grown silicon.

The study of GaAs on Si substrates growth has been started since mid of 1980s [17, 18] and it was optimised by few groups later. However, the difficulties of III–V material monolithically grown on Si substrates are the lattice mismatch and different thermal expansion coefficient between III–V materials and Si substrates. To migrate III–V light emitting source on Si platform, buffer layer is very necessary in the growth and GaAs, InP, GaP, AlP and AlAs play the role most of time. For the epitaxial growth of the polar materials to non-polar substrates, anti-phase domain (APD) is appeared, but can be eliminated by introduce two-step growth and off-cut oriented Si substrate. As well there are high density (10^{10} cm^{-2}) of threading dislocations (TDs) propagating from the interface between III–V material and Si substrate due to the lattice mismatch between Si and other III–V material. To further reduce the density of TDs, defect filter layer (DFL) is an ideal method to reduce the density of TDs from ~10^{10} to ~10^{6} cm^{-2}. Until now, different types of DFLs are demonstrated, including InGaAs/GaAs strained-layer superlattices (SLSs) on Si substrate, InGaN on GaN. By using the InGaAs DFL, the first 1.3 μm InAs/GaAs QD laser based on Si substrate has been established by T. Wang *et al* [19] with maximum operating temperature of 42 ºC and RT J_{th} = 725 A/cm^2. In this chapter, different types of DFLs including InAs/GaAs QDs [20], InGaAs submonolayer QDs [21], InGaAs/GaAs SLSs [22] and InAlAs/GaAs SLSs are compared by photoluminescence (PL), atomic force microscopy (AFM) and transmission electron microscopy (TEM).

3.2 MBE Growth of DFLs Structures

Silicon-based InAs/GaAs QDs structures are grown by MBE system with various DFLs introduced after GaAs buffer layer. Before the growth, Si substrate has been de-oxidised at 900 ºC for 30 minutes. A two-step growth of 1 μm of GaAs buffer layer has been optimised on Si (100) off-cut substrate 4˚ oriented to [110]. Different types of DFLs have been grown after GaAs buffer layer for comparing the efficiency of blocking the propagation of TDs. InAs/GaAs QDs, InGaAs SML QDs, InGaAs/GaAs SLSs and InAlAs/GaAs SLSs have been tested in the

project. Five layers of InAs/GaAs dot-in-the-well (DWELL) are grown around nucleation temperature 510 ºC and each layer of DWELL has 3 monolayers of InAs deposited on 2 nm of $In_{0.15}Ga_{0.85}As$ and capped with 6 nm of $In_{0.15}Ga_{0.85}As$. The growth rate of InAs on $In_{0.15}Ga_{0.85}As$ is ~0.1 ML/s. As shown in RHEED pattern, it could be clearly found that the dots are formed around 16 second during the deposition. The DWELL structure is sandwiched with 50 nm GaAs and 100 nm $Al_{0.4}Ga_{0.6}As$ layer, which GaAs grown at 590 ºC and AlGaAs grown at 610 ºC.

3.3 The PL Measurement of Each DFLs

The growths of each type of DFL are based on the same growth conditions, which help us to determine the performance of DFL by filtering the TDs. AFM, PL and TEM have been used to investigate the performance and compare study between each type of DFL.

3.3.1 InAs/GaAs QD DFL

5 layers of InAs/GaAs QDs with 50 nm GaAs spacing layer form one set of DFL and was repeated 3 times with 250 nm GaAs spacing layer. Each layer consists of 2.2 ML InAs/GaAs QDs grown on 2 nm InGaAs and capped with 6 nm InGaAs. The InAs/GaAs QDs were grown at 510 ˚C, the optimised growth temperature. Figures 3.1 and 3.2 present the temperature dependent and power dependent PL measurement respectively. In the power dependent measurement (10 K), the excited state and ground state are obvious shown in the spectrum, with ground state emission at 1184 nm (1.045 eV) and excited state emission at 1132 nm (1.095 eV), as shown in Figure 3.1.

We see a regular blue shift when the temperature decreases from 300 K to 10 K but the peak intensity first increase and then fall. The blueshift is due to the lattice shrink at low temperature which effects on the bang gap. During the measurements, the excited laser power was kept at 10 mW. The increase of PL is contributed to the carrier frozen in the quantum dot and less opportunity of the thermal escape. These effects also appear in the rest of PL measurements as well. The fall of PL in the low temperature growth condition could due to the asymmetric distribution of QDs' size, as is confirmed by the AFM measurement. The asymmetric distribution of QD's also results of higher bandwidth of PL emission.

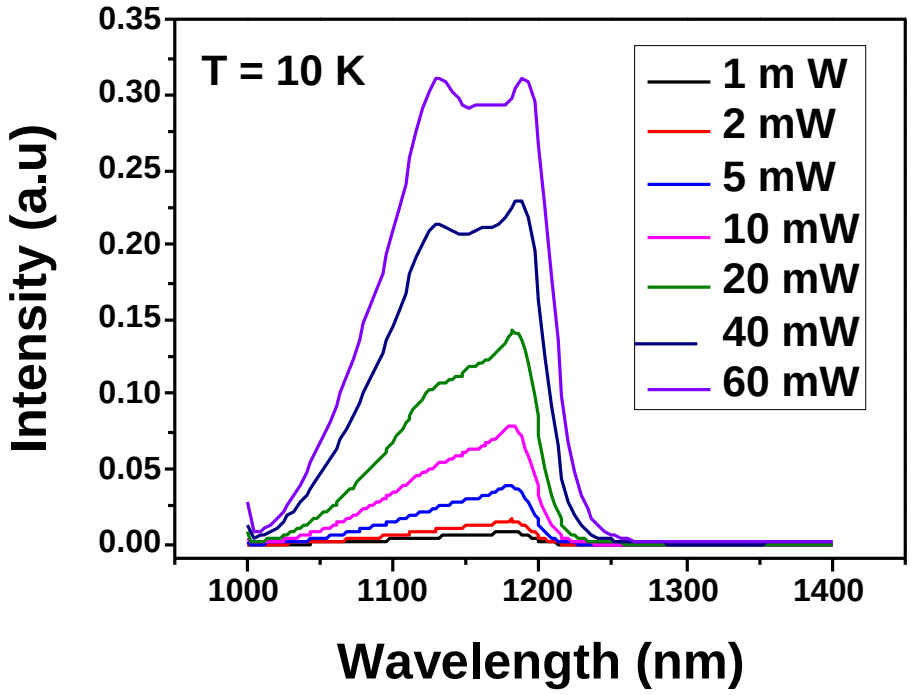

Figure 3.1 Power dependent PL measurements of InAs/GaAs QDs on Si substrate with InAs QDs DFLs at 10 K.

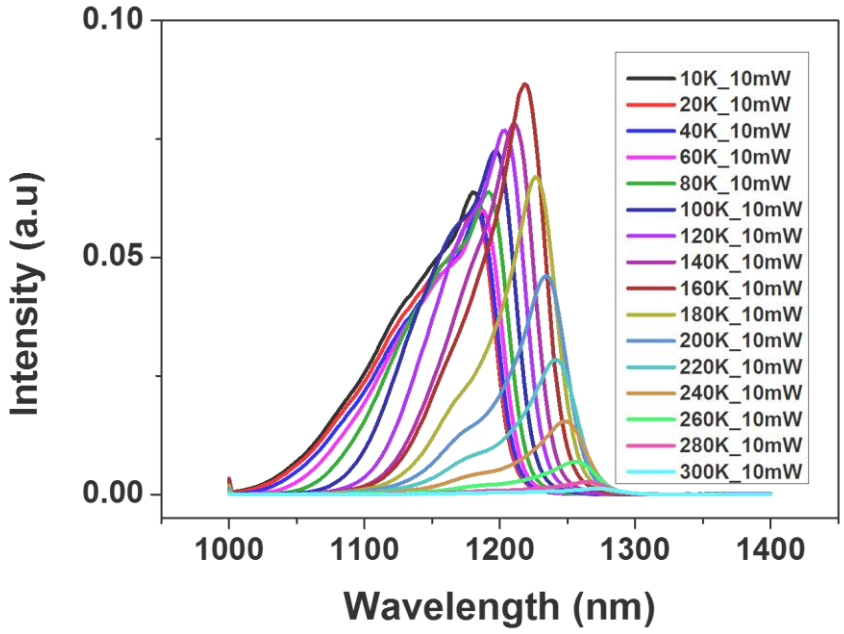

Figure 3.2 Temperature dependent PL measurements of InAs/GaAs QDs on Si substrate with InAs QDs DFLs under the excited power 10 mW.

3.3.2 InGaAs SML QD DFL

For each set of InGaAs SML QD DFLs, approximately 1 ML InAs has been grown and covered by GaAs layer, which repeated 10 times with 10 nm GaAs spacing layer to form one set of DFL. Three sets of DFL were grown in the experiment sample with 400 nm GaAs spacing layer. The PL measurement represented InGaAs SML QD DFL with stronger emission at ground states compare with InAs QDs DFL, the separation between ground state and excited state is larger as well.

At 10 K, the PL spectra (as shown in Figure 3.3) present a excited state at 1134 nm (1.093 eV) and ground state at 1194 nm (1.038 eV) where the gap is 57 meV between excited and ground state. With the excited power increasing, the excited state become more obvious. Figure 3.4 shows the temperature dependent PL spectra that the peak intensity decrease at temperature 160 K.

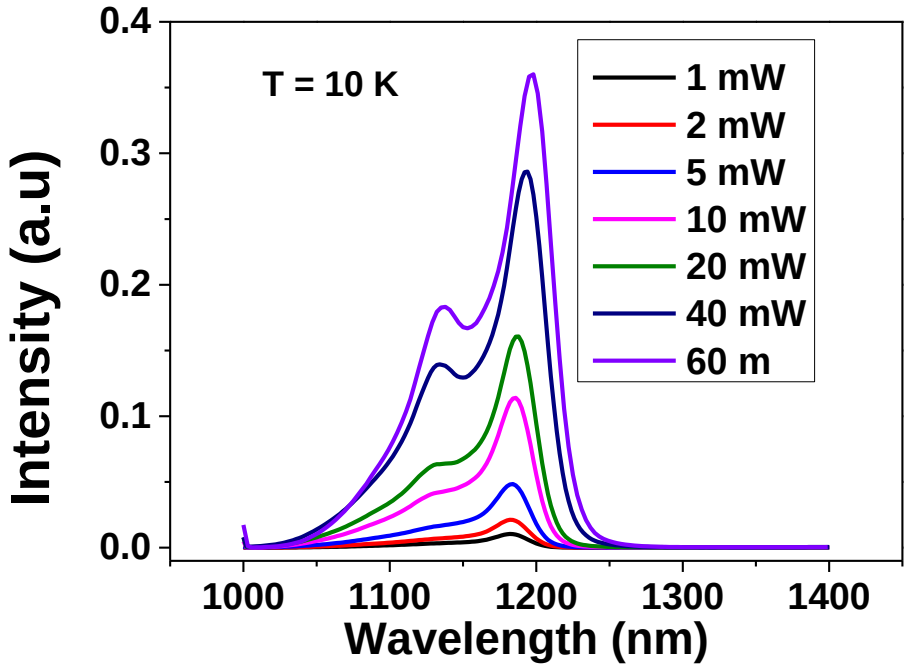

Figure 3.3 Power dependent PL measurements of InAs/GaAs QDs on Si substrate with InGaAs SML QDs DFLs at 10 K.

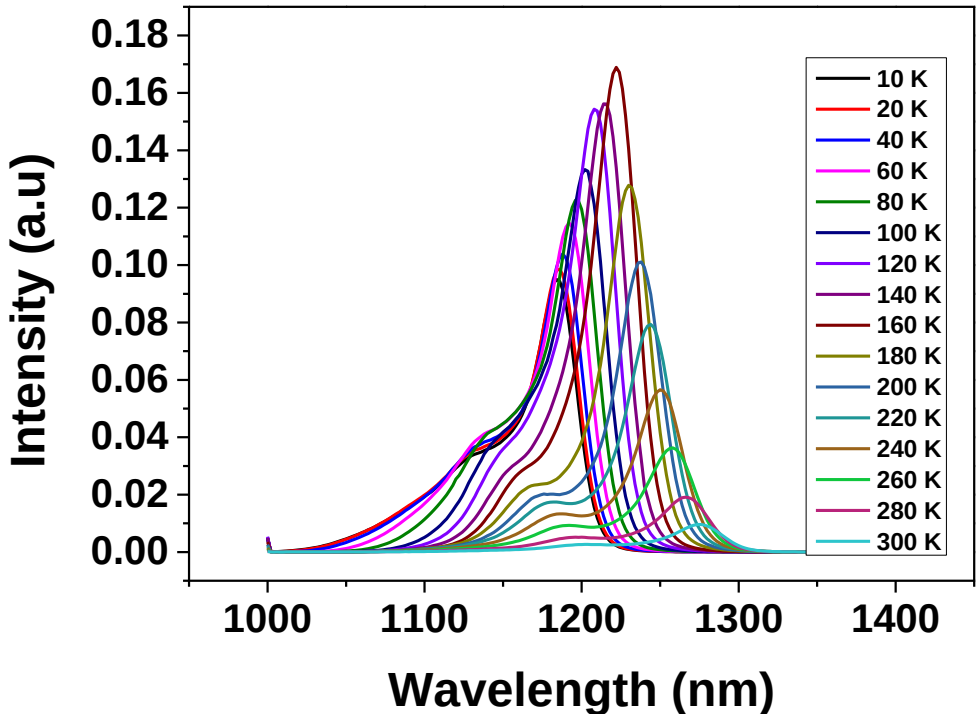

Figure 3.4 Temperature dependent PL measurements of InAs/GaAs QDs on Si substrate with InGaAs SML QDs DFLs under the excited power 10 mW.

3.3.3 InAlAs/GaAs SLSs DFL

To optimise the DFL, Al was considered due to its high bonding energy, which could block the propagation of defects. Three sets of InAlAs/GaAs SLSs DFL have been fabricated and examined in order to make comparison study.

In the power dependent PL measurements (Figure 3.5), the ground state and excited state emission are at 1194 nm (1.038 eV) and 1144 nm (1.084 eV) under the temperature condition 10 K. Compare with the other sample's power dependent measurement, the excited states emissions are clearly to be observed with laser power increasing. The gap between excited and ground state is about 46 meV. Figure 3.6 presents the temperature dependent PL, that second excitation states were observed at lowtemperature (< 40 K).

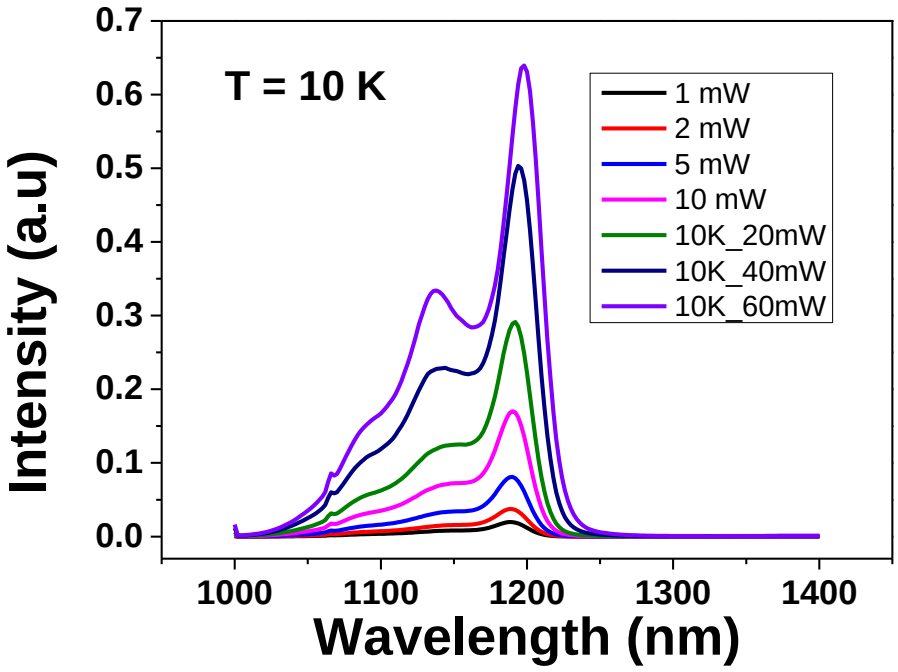

Figure 3.5 Power dependent PL measurement of InAs/GaAs QDs on Si substrate with InAlAs/GaAs SLSs DFLs.

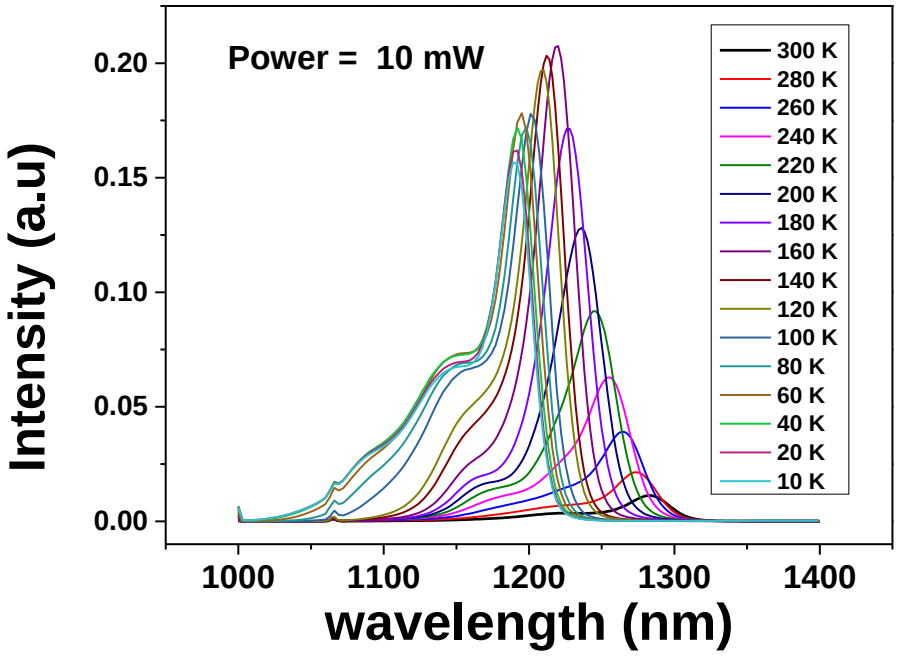

Figure 3.6 Temperature dependent PL measurements of InAs/GaAs QDs on Si substrate with InAlAs/GaAs SLSs DFLs.

3.3.4 InGaAs/GaAs SLSs DFL

InGaAs/GaAs SLSs DFLs also have been compared studied in this project. InGaAs/GaAs SLSs have been proved as a successful type of DFL based on Si substrate. In order to compare the performance of each type of DFL, same temperature condition and spacing layer thickness of growth were used in InAlAs/GaAs SLSs and InGaAs/GaAs. The temperature dependent PL (Figure 3.7) shows the ratio of PL intensity of excited state with ground state increase when the temperature significantly decrease from 300 to 10 K, which means the more carrier were excited to excited state. At 10 K , the ground state emits at 1180 nm (1.051 eV) and excited state emit at 1132 nm (1.095 eV) which the gap is 44 meV less than other DFL.

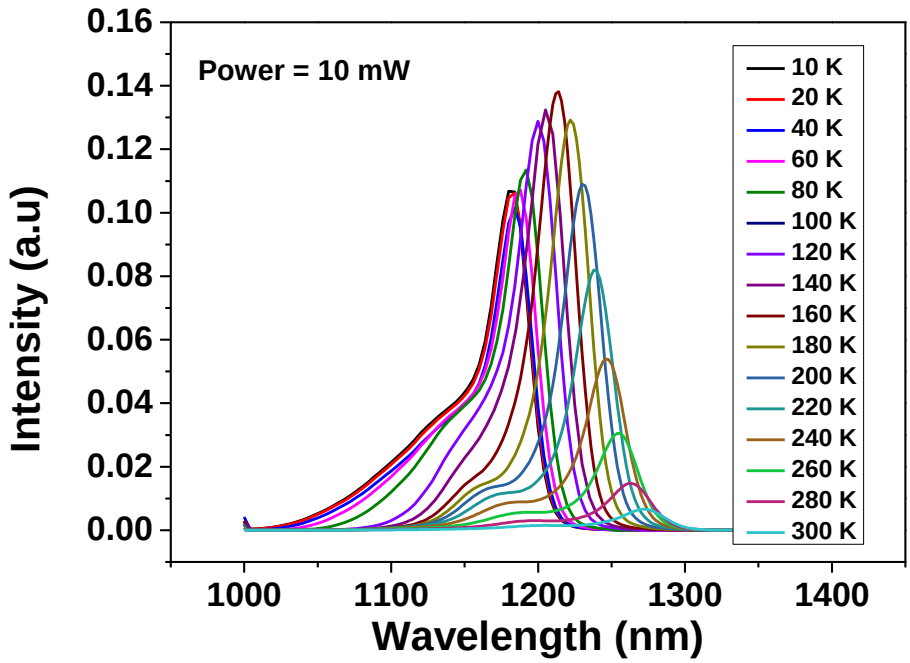

Figure 3.7 Temperature dependent PL measurements of InAs/GaAs QDs based on Si substrate with InGaAs/GaAs SLSs DFLs under 10 mW excited power.

3.3.5 PL Comparison

Figures 3.8 and 3.9 compare the PL spectrum for InAs/GaAs quantum dots with different DFL under 10 mW excited power at 10 K and room temperature, respectively. The measurements were undertaken at same condition including monochrometre setting, temperature and excited laser power. It obviously shows that the intensity of InAs/GaAs QDs with InAlAs SLSs DFL have the strongest emission in the 10 K and at room temperature, while the sample with InAs QDs DFL has the lowest emission. In Figure 3.10, the trends of PL peak intensity against

temperature are shown which proves InAlAs/GaAs SLSs have the strongest emission at whole temperature range. For all the samples, the peak intensity decrease once temperature is below 160 K which could due to the carriers were trapped in excited state and recombination from conduction band to valance band rather than decay to ground state.

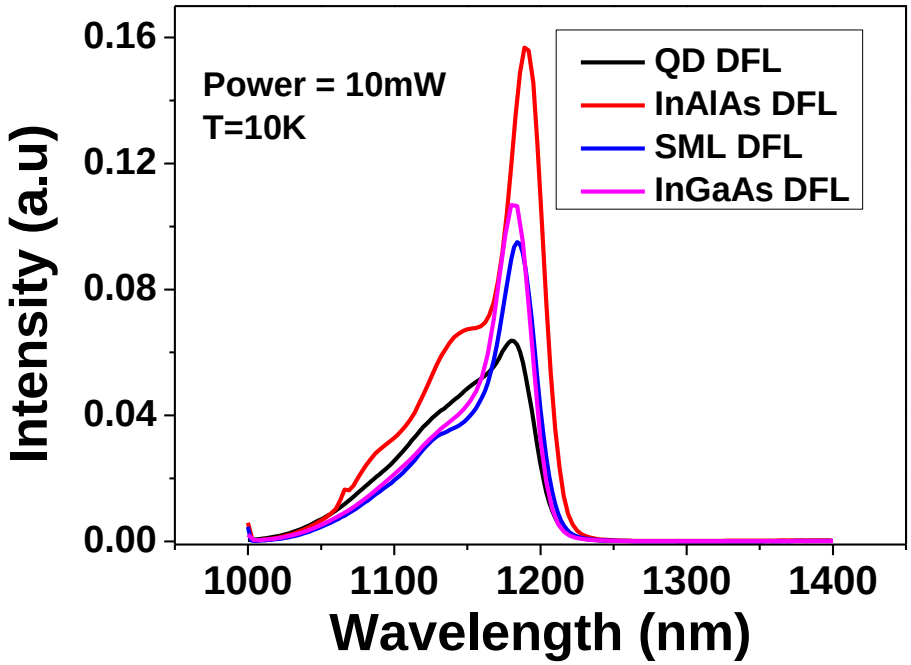

Figure 3.8. Comparative PL measurement for each types of DFL under the same temperature (10 K) and excited laser power (10 mW).

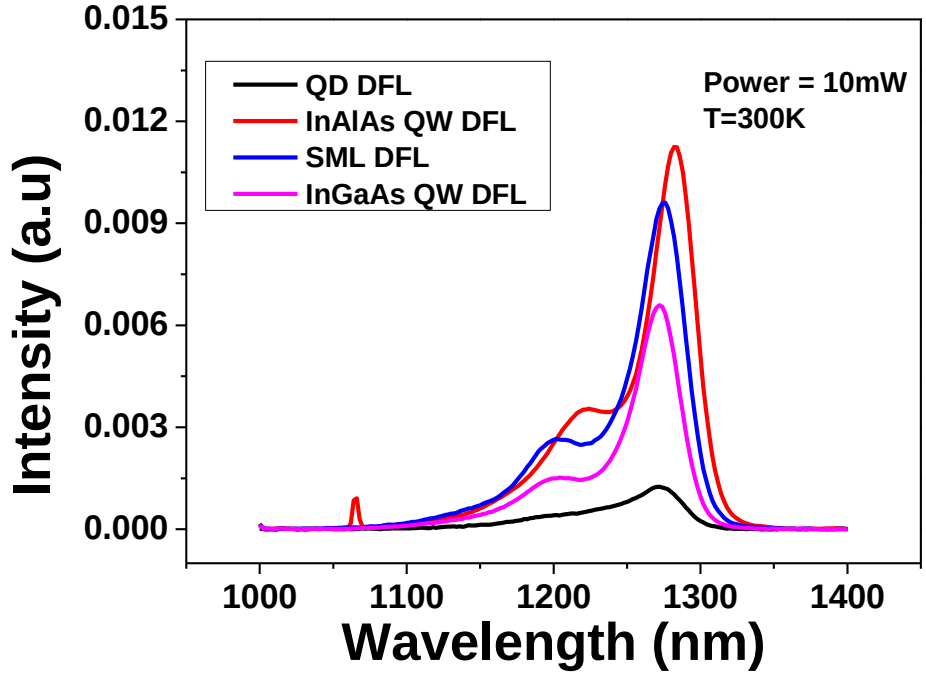

Figure 3.9 Comparative PL measurement for each types of DFL under the same temperature (300 K) and excited laser power (10 mW).

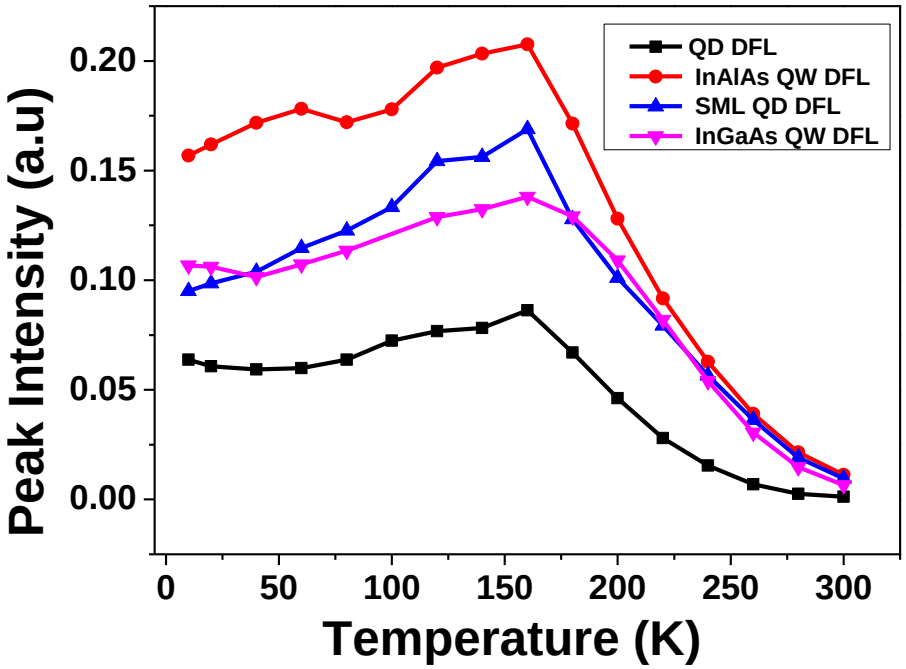

Figure 3.10 PL measurement of peak intensity against temperature for each types of DFLs. The excited laser power was kept at 10 mW during the measurements.

3.4 AFM Measurement Comparison of Each DFLs

We used AFM to examine the uncapped InAs/GaAs QDs and the density of QDs are observed from 1 μm × 1 μm image. The defects density also presented in large scale AFM image (5 μm × 5 μm). The uncapped InAs/GaAs QDs grow with identical conditions as the capped QDs in the PL measurement, which is able to make comparison study with PL measurement.

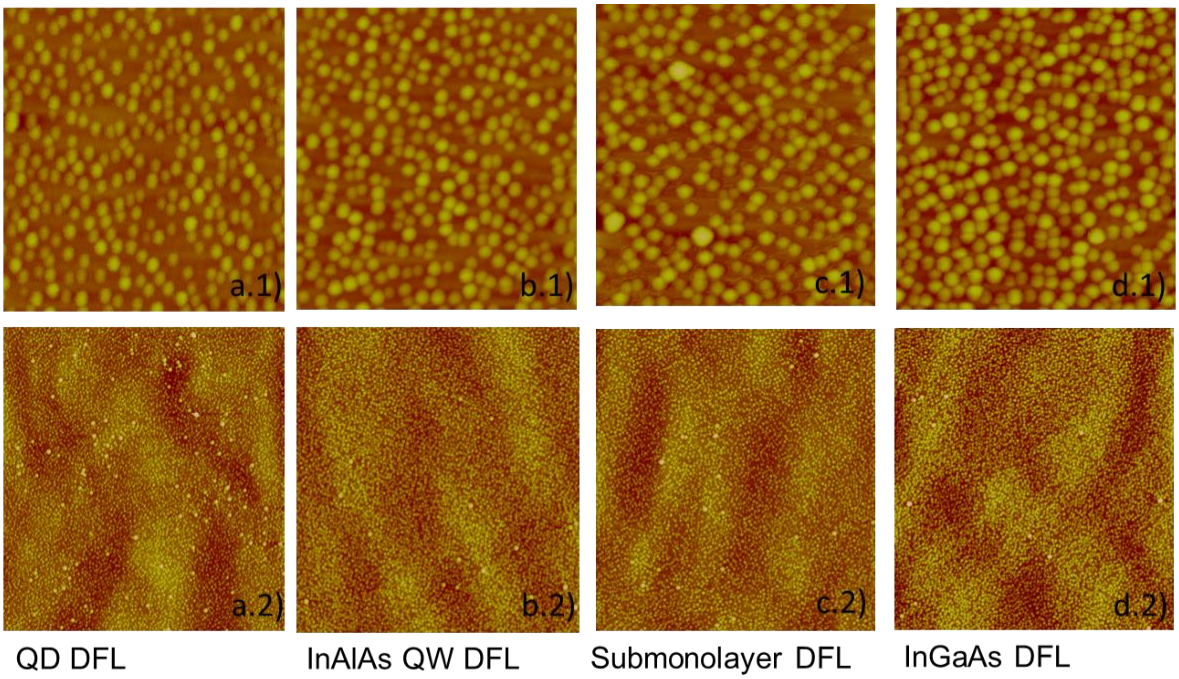

Figure 3.11 AFM images of InAs/GaAs QDs monolithically grown on Si substrate with different types of DFLs, where 1) is 1 μm × 1 μm and 2) is 5 μm × 5 μm.

Figure 3.11 presents the comparison of InAs/GaAs QDs with different types of DFL. It is clear that InGaAs/GaAs SLSs DFL and InAlAs/GaAs SLSs DFL have the lowest number of defect density and highest number of dots density. The sample with QD DFL has the dots density is 2.97×10^{10} cm^{-2} which is higher than InGaAs SML DFL 2.74×10^{10} cm^{-2} dot density. In contrast, the samples with InAlAs/GaAs SLSs DFL and InGaAs/GaAs SLSs DFL have dot density 3.18×10^{10} cm^{-2} and 3.24×10^{10} cm^{-2} respectively. The QD defect (larger dots) densities are 52, 6.4, 6.8 and 4.4×10^{9} cm^{-2} for QD, InAlAs, submonolayer and InGaAs DFL respectively. The QD defect is different with crystal defects, which is normal caused by strain non-uniformity. By combining the density of QDs and defects, it proves that InAlAs/GaAs SLSs DFLs and InGaAs/GaAs SLSs DFLs contribute best crystal quality.

3.5 TEM Measurement Comparison of Each DFL

As a straight forward method to assess the crystal quality of semiconductor restructure, TEM is a necessary tool to examine the crystal structure with cross-section view. The samples with different DFLs have been measured by TEM and the active region consisting of 5 layers of InAs/GaAs QDs in the well structure.

Before the DFLs, as shown in Figure 3.12, the GaAs buffer layer has stopped the most of TDs in the first 30 nm which should credit to the low temperature and growth rate GaAs. It also shows the TDs have gone through all the three layers of DFL and cross the QDs region as well. However, InGaAs SML DFL (Figure 3.12 (b)), InGaAs/GaAs SLSs DFL (Figure 3.12 (c)) and InAlAs/GaAs SLSs DFL (Figure 3.12 (d)) successfully confine the TDs propagating into the active region. There is more than 1×10^{10} cm^{-2} TDs observed after the 1 μm GaAs buffer layer measured by EPD (etch pit density). After the three set of InAlAs/GaAs SLSs DFL or InGaAs/GaAs SLSs DFL, it has been filtered to 10^{7} cm^{-2}. The densities of TDs have been measured by University of Arkensas

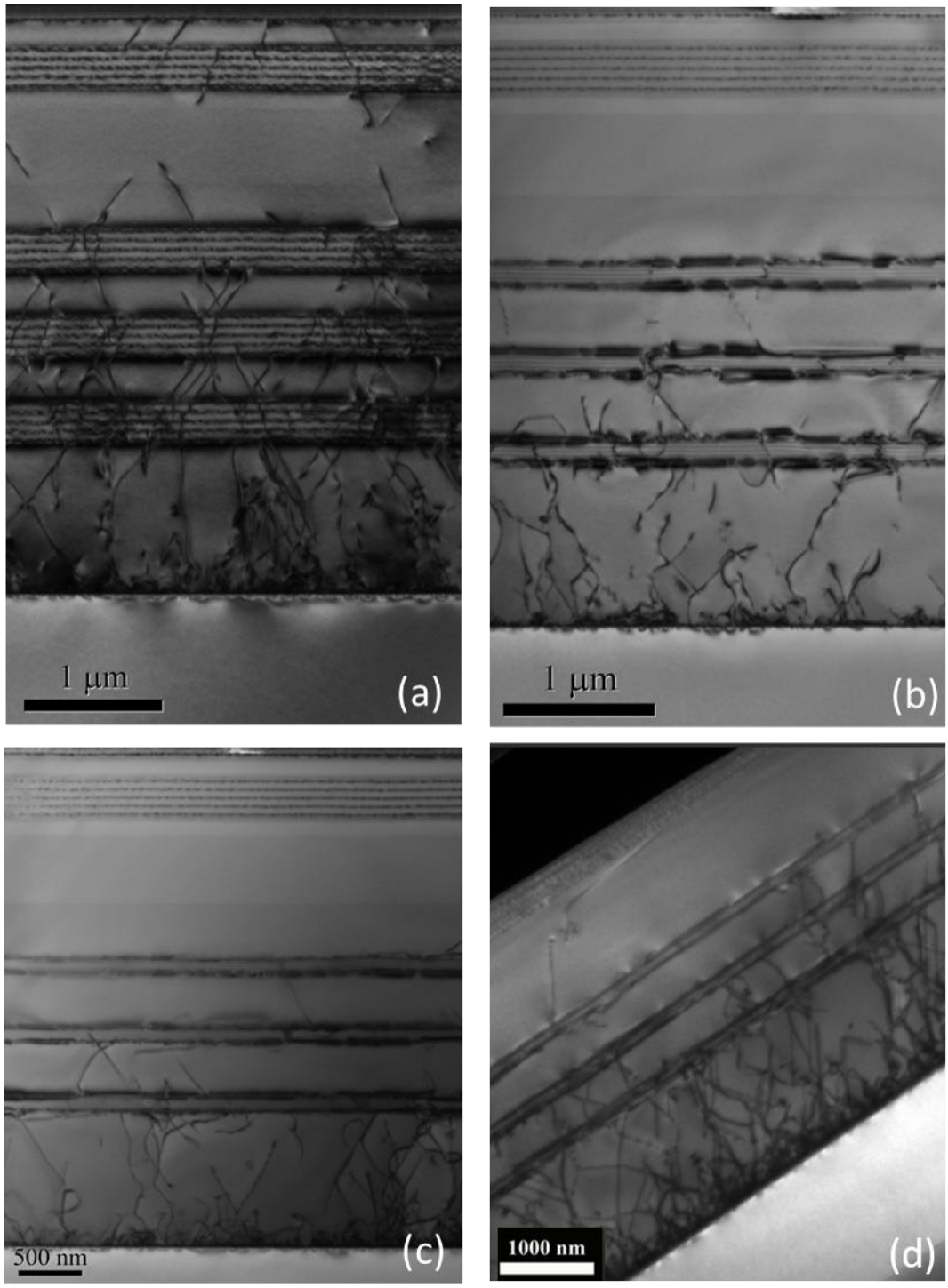

Figure 3.12 TEM measurements of InAs/GaAs QDs based on Si substrate with (a) InAs QDs DFL. The TDs are observed crossing the whole DFL layers and active region; (b) InGaAs SML QDs DFL; (c) InGaAs/GaAs SLSs DFLs. (d) Dark-field TEM measurements of InAs/GaAs QDs based on Si substrate with 3 set of InAlAs/GaAs SLS DF. The TEM images were measured by University of Arkansas.

In the Figure 3.13, the high resolution TEM images were presented, which show the interface of InAlAs and GaAs has defect free. The TEM shows the thickness InAlAs and GaAs are 10 nm exactly. In the Figure 3.14, the five layers of InAs/GaAs QDs capped with 6 nm InGaAs and space with GaAs 50 nm. QD region has no defect observed and we could assume we have minimised the TDs affect to our laser structure.

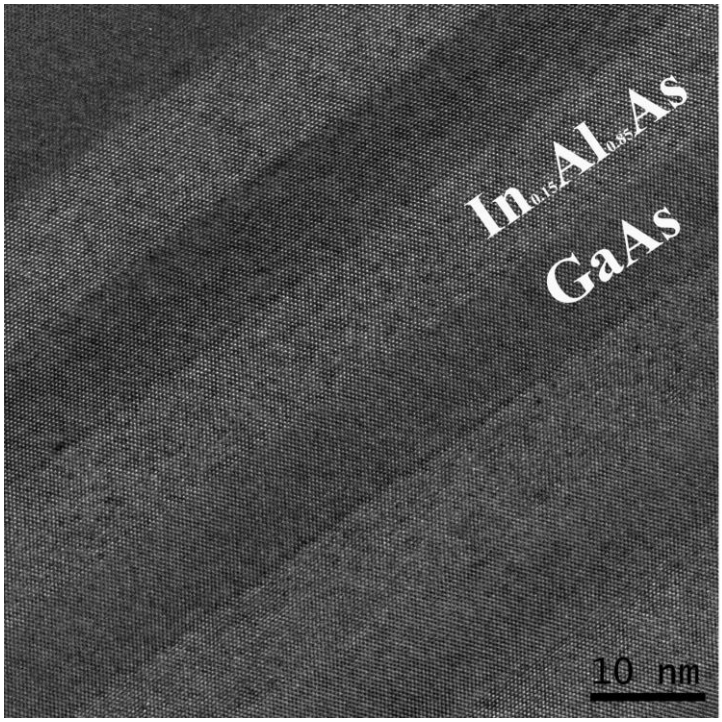

Figure 3.13 High resolution TEM (HRTEM) image of InAlAs/GaAs SLSs. The InAlAs/GaAs SLS has clear atoms interface without any defects. The TEM images were measured by University of Arkansas.

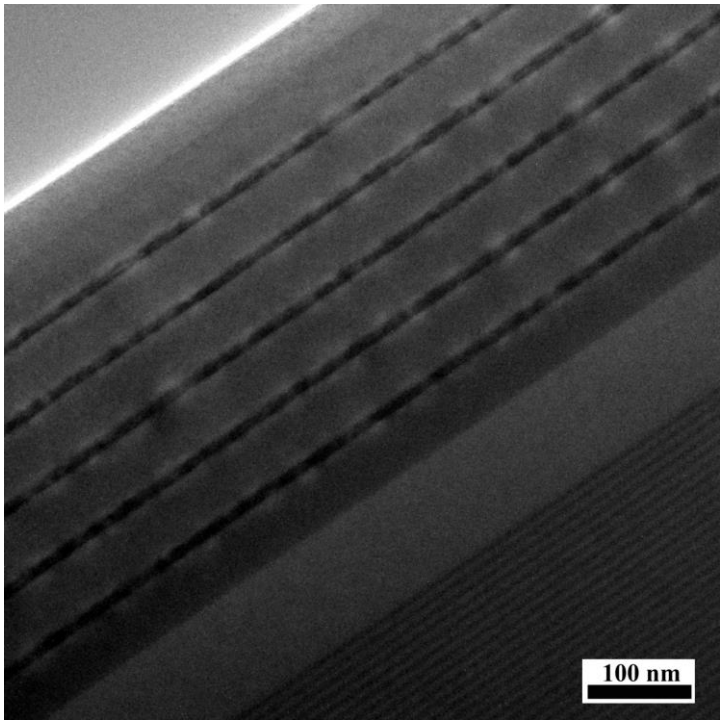

Figure 3.14 TEM image of 5 layers of InAs/GaAs QDs grown on Si substrate with InAlAs/GaAs SLSs DFLs. The image indicates the defect free active region with scale bar 100 nm. The TEM images were measured by University of Arkansas.

3.6 Laser Growth and Processing

The Si substrate has been de-oxidised by heating to 900 ºC for 30 minutes. Then the substrate was cooled down to 400 ºC for 1st step GaAs layer growth. The first 30 nm GaAs is grown at low growth rate, 0.1 ML/s. the 2nd step buffer layer of 970 nm GaAs grown at higher temperature and growth rate. The two-step GaAs buffer layer has Si doped. The InAlAs/GaAs SLSs DFLs which consist of 5 repeats of SLS structure and each SLS has 5 layers of InAlAs/GaAs for 10 nm thickness receptivity. Between each set of InAlAs/GaAs SLSs, 400 nm GaAs spacing layer were grown at 2 ML/s. After DFLs, 300 nm Si doped GaAs contact layer and 1500 nm AlGaAs Si doped cladding layer were grown. InAs/GaAs QDs DWELL structure formed active region which consists of 5 layers of InAs/GaAs QD with 50 nm GaAs spacing layer. The 3 ML InAs/GaAs QDs grown at optimised temperature around 510 ºC which was on 2 nm $In_{0.15}GaAs_{0.85}$ and capped 6 nm $In_{0.15}Ga_{0.85}As$. Another Be doped (p-type) 1500 nm AlGaAs cladding layer and GaAs top contact deposited on active region.

In the device fabrication processing, the two GaAs contacts are located top for avoiding the poor quality of Si and GaAs interface, as shown in Figure 3.18. N-type GaAs contact were

etched down from top surface and metallise with InGe/Au. The P-type GaAs contact deposited with Ti/Pt/Au. 50 μm of ridges were etched. The ridges were etched down to 200 nm below the active region for an improved carrier confinement. Devices of 3-mm length were mounted and wire bonded on ceramic tiles to enable testing. No facet coating is applied.

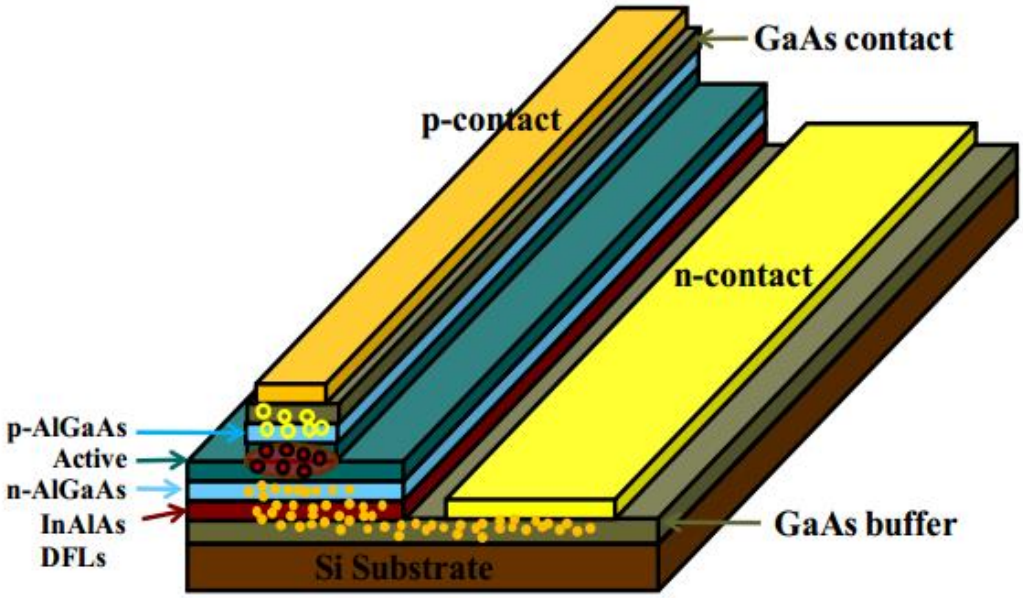

Figure 3.15 InAs/GaAs QDs laser based on Si substrate schematic diagram with asymmetric structure, where n and p contact are both faced topside.

The optical power against current (L-I) characteristic measurement proves that our lasers have significantly improvement compared with the previous work on InAs/GaAs QDs laser on Si substrate with InGaAs/GaAs SLSs DFLs. The lowest J_{th} is at 194 A/cm^2 (Figure 3.16) and maximum operating temperature is 85 ºC under pulsed mode (Figure 3.20). Figure 3.21 proves the lowest J_{th} 194 A/cm^2 by measuring the spectrum of laser and there have multi emission at $J_{th\ of}$ 267 A/cm^2. At J_{th} of f194 A/cm^2, a narrow laser spectrum has been measured and it is cantered at 1267 nm. Upon increasing the current density, the density of lasing modes is observed to increase.

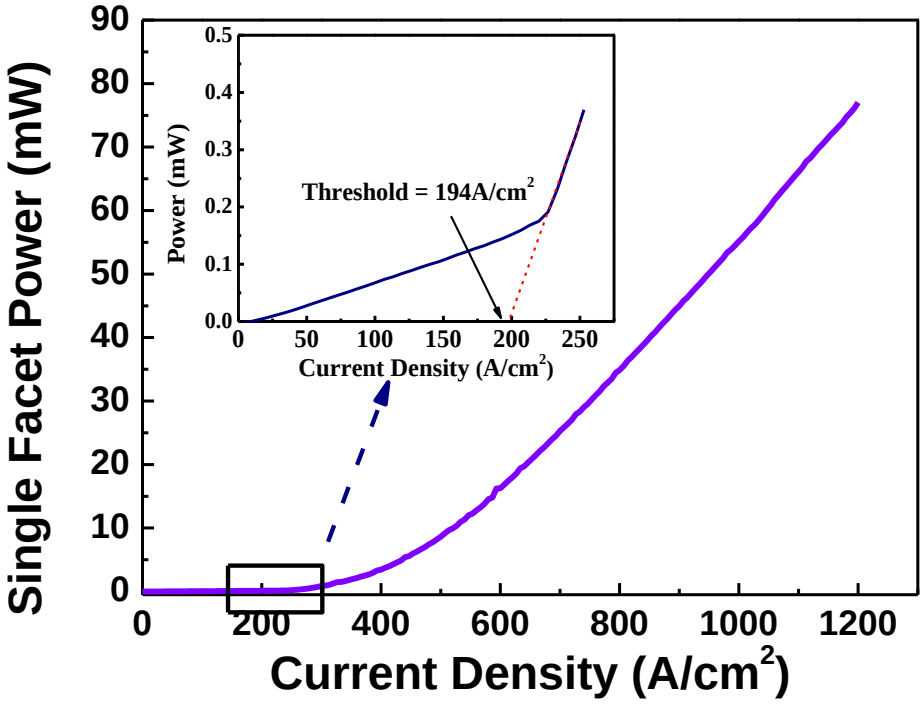

Figure 3.16 L-I measurement of InAs/GaAs QDs laser diode based on Si substrate with low threshold current density 194 A/cm^2

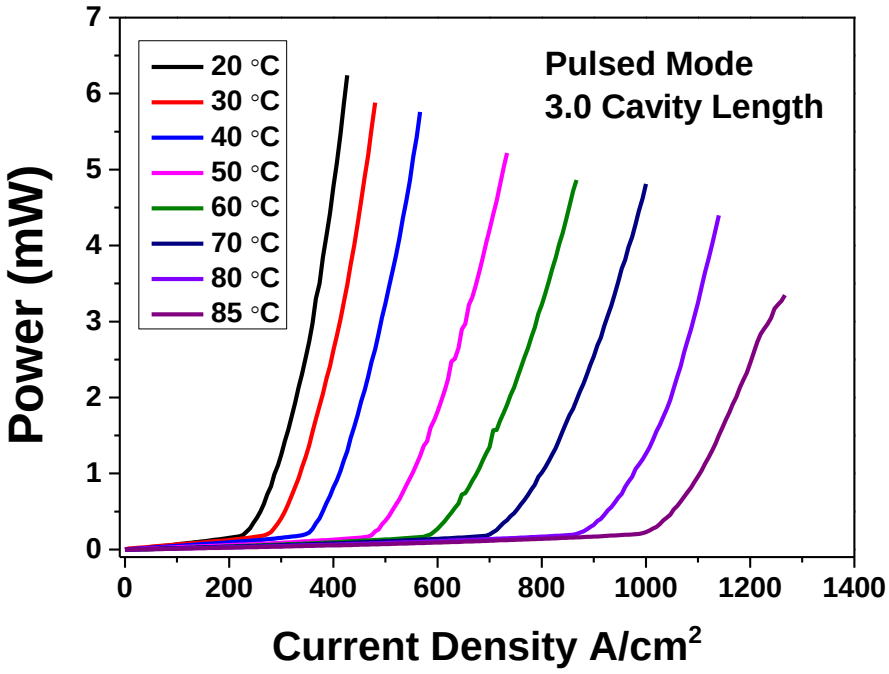

Figure 3.17 Temperature dependent L-I measurement which proves the laser operating at maximum temperature 85 ºC.

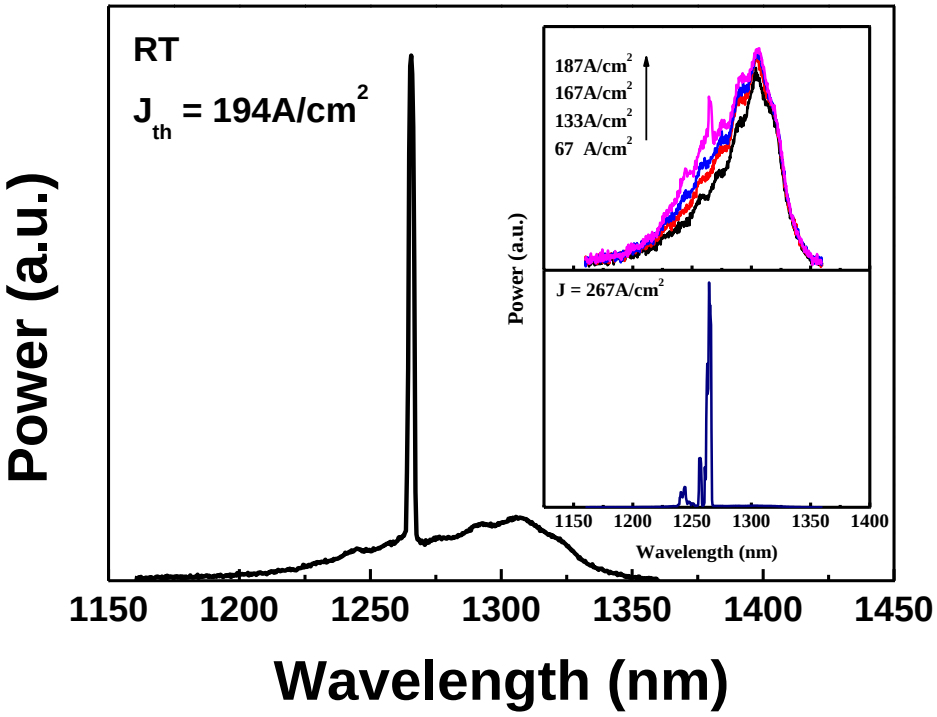

Figure 3.18 laser spectrum at room temperature. The spectrum shows the lasing with J_{th} from 67 to 267 A/cm^2.

In order to examine the laser quality, characteristic temperature (T_0) has been calculated which is 45 K between the temperature 20 to 85 ºC. The equation which used to obtain the value of T_0 has been presented as

$$J_{th} = J_0 \exp(T/T_0)$$

Ideally, if the variation of J_{th} is significantly reduced and then the larger T_0 value can be found out. The T_0 can be improved by introducing P-type modulation doping into quantum dots so that the confinement of holes will be stronger [25].

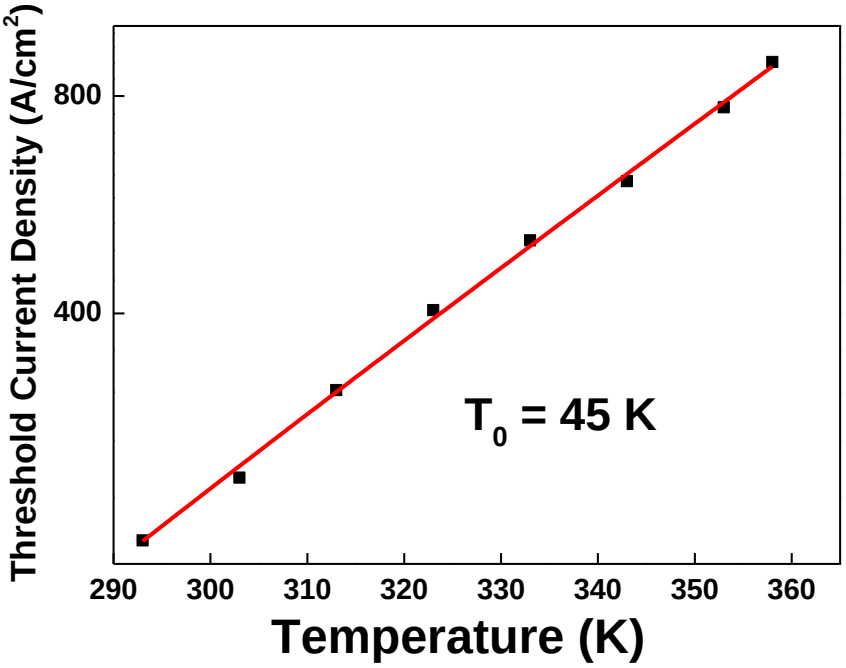

Figure 3.19 Threshold current density against temperature for InAs/GaAs QDs laser based on Si substrate. Characteristic temperature has been calculated as 45 K between temperatures 20 to 85 °C.

3.7 Conclusion

We have successfully demonstrated a InAs/GaAs QDs laser monolithically grown on a Si substrate with low J_{th} (194 A/cm^2) and high temperature operating (maximum 85 ˚C) by introducing a InAlAs/GaAs SLSs DFLs to reduce the density of TDs. The reason of only pulsed operation is due to the density of TDs cannot be achieved as same as GaAs based laser devices. High ratio of non-radiative recombination centre were created within those defects (TDs). Also carriers simply escape due to the heat stacked in point defects.

In conclusion, InAlAs/GaAs SLSs DFLs present the strongest ability to improve the crystal quality by reducing lower density of TDs due to the higher bonding energy of Al and As atoms. No defects observed in the active region by TEM measurements. The poor performance of T_0 is due to the high ratio of non-radiative recombination centre in the heterostructure [26] and it is lower than other GaAs based InAs/GaAs QD lasers [27].

Reference

1. G. T. Reed, G. Mashanovich, F. Y. Gardes, and D. J. Thomson, “Silicon optical modulators,” *Nature Photon.*, vol. 4, no. 8, pp. 518–526, 2010
2. Qianfan Xu, Bradley Schmidt, Sameer Pradhan, Michal Lipson, Micrometre-scale silicon electro-optic modulator, *Nature*, vol. 435, pp. 325-327, 2005
3. Mark A. Foster, Amy C. Turner, Jay E. Sharping, Bradley S. Schmidt, Michal Lipson, Alexander L. Gaeta, “Broad-band optical parametric gain on a silicon photonic chip”, *Nature*, vol. 441, no. 960-963, 2006
4. W. R. Headley, G. T. Reed, A. Liu, M. Paniccia, S. Howe, “Polar-ization independent optical racetrack resonators using rib waveguide onsilicon on insulator,” *Appl. Phys. Letters*, vol. 85. Pp. 5523–5525, 2004
5. J. Michel, J. Liu, and L. C. Kimerling, “High-performance Ge-on-Si photodetectors,” *Nature Photon.*, vol. 4, no. 8, pp. 527–534, 2010
6. Linus C. Chuang , Forrest G. Sedgwick , Roger Chen , Wai Son Ko , Michael Moewe , Kar Wei Ng, Thai-Truong D. Tranand Connie Chang-Hasnain, “GaAs-Based Nanoneedle Light Emitting Diode and Avalanche Photodiode Monolithically Integrated on a Silicon Substrate”, *Nano Letters*, vol. 11, no. 2, pp 385–390, 2011
7. P.T. Landsberg, M.J. Adams, “Radiative and Auger processes in semiconductors”, *Journal of Luminescence*, vol. 7, pp. 3–34, 1973
8. Haisheng Rong, Richard Jones, Ansheng Liu, Oded Cohen, Dani Hak, Alexander Fang and Mario Paniccia, “A continuous-wave Raman silicon laser”, *Nature*, vol. 433, pp. 725-728, 2005
9. Alexander W. Fang, Hyundai Park, Oded Cohen, Richard Jones, Mario J. Paniccia, and John E. Bowers, “Electrically pumped hybrid AlGaInAs-silicon evanescent laser”, *Optics Express*, vol. 14, no. 20, pp. 9203-9210, 2006
10. Hyundai Park, Alexander W. Fang, Satoshi Kodama, and John E. Bowers, “Hybrid silicon evanescent laser fabricated with a silicon waveguide and III–V offset quantum wells”, *Optics Express*, vol. 13, no. 23, pp. 9460-9464, 2005
11. G. Roelkens, Joris Van Campenhout, Joost Brouckaert, Dries Van Thourhout, Roel Baets, P. Rojo Romeo, P. Regreny *et al*. "III–V/Si photonics by die-to-wafer bonding." *Materials Today*, vol. 10, no. 7, pp. 36-43, 2007
12. Yu B. Bolkhovityanov, and Oleg Petrovich Pchelyakov. “GaAs epitaxy on Si substrates: modern status of research and engineering”, *Physics-Uspekhi*, vol. 51, no. 5, pp. 437-456,

2008

13. S. Tanaka, S. Jeong, S. Sekiguchi, T. Kurahashi, Y. Tanaka, and K. Morito, "High-output-power, single-wavelength silicon hybrid laser using precise flip-chip bonding technology," *Optics Express*, vol. 20, no. 27, pp. 28057-28069, 2012
14. SM Chen, MC Tang, J Wu, Q Jiang, VG Dorogan, M Benamara, YI Mazur, GJ Salamo, AJ Seeds, H Liu, 1.3 μm InAs/GaAs quantum-dot laser monolithically grown on Si substrates operating over 100°C, *Electronics Letters*, vol. 50, no. 20, pp. 1467 – 1468, 2014
15. R. Chen, T. D. Tran, K. W. Ng, W. S. Ko, L. C. Chuang, F. G. Sedgwick, and C. Chang-Hasnain, "Nanolasers grown on silicon," *Nature Photon.*, vol. 5, pp. 170-175, 2011
16. Markku Leskelä and Mikko Ritala, "Atomic layer deposition (ALD): from precursors to thin film structures", *Thin solid films*, vol. 409, no. 1, pp. 138-146, 2002
17. W. I. Wang, "Molecular beam epitaxial growth and material properties of GaAs and AlGaAs on Si (100)", *Appl. Phys. Letters*, vol. 44, no. 12, pp. 1149-1151, 1984
18. W. T. Masselink, T. Henderson, J. Klem, R. Fischer, P. Pearah, H. Morkoc, M. Hafich, P. D. Wang, and G. Y. Robinson, "Optical properties of GaAs on (100) Si using molecular beam epitaxy." *Applied Physics Letters*, vol. 45, no. 12, pp. 1309-1311, 1984
19. T. Wang, H. Liu, A. Lee, F. Pozzi, A. Seeds, "1.3-μm InAs/GaAs quantum-dot lasers monolithically grown on Si substrates," *Optics Express*, vol. 19, no. 12, pp. 11381–11386, 2011,
20. Jun Yang, Pallab Bhattacharya, Zetian Mi, High-Performance In0.5Ga0.5 As/GaAs Quantum-Dot Lasers on Silicon With Multiple-Layer Quantum-Dot Defect filters, *Electron Devices, IEEE Transactions on*, vol. 54, no. 11, no. 2849-2855, 2007
21. Alexey R. Kovsh, Alexey E. Zhukov, Nikolay A. Maleev, Sergei S. Mikhrin, D. A. Livshits, Yuri M. Shernyakov, M. V. Maximov *et al*. "High power lasers based on submonolayer InAs–GaAs quantum dots and InGaAs quantum wells." *Microelectronics Journal*, vol. 34, no. 5, pp. 491-493, 2003
22. Uchida, Y., H. Kakibayashi, and S. Goto. "Electrical and structural properties of dislocations confined in a InGaAs/GaAs heterostructure." *Journal of Applied Physics* vol. 74, no. 11, pp. 6720-6725. 1993
23. A.R. Kovsh, N.A. Maleev, A.E. Zhukov, S.S. Mikhrin, A.P. Vasil'ev, Yu.M. Shernyakov, M.V. Maximov, D.A. Livshits, V.M. Ustinov, Zh.I. Alferov, N.N. Ledentsov, D. Bimberg, InAs/InGaAs/GaAs quantum dot lasers of 1.3 μm range with high (88%) differential

efficiency, *Electronics Letters*, vol. 38, no. 19, pp. 1104 – 1106, 2002

24. O. B. Shchekin, D. G. Deppe, 1.3 μm InAs quantum dot laser with To=161 K from 0 to 80°C, *Applied Physics Letters*, vol. 80, pp. 3277 2002
25. Zhang, Y., X. Q. Wang, W. Y. Chen, X. D. Bai, C. X. Liu, S. R. Yang, and S. Y. Liu. "Analysis of room temperature PL spectra of InAs/GaAs/InP and InAs/InP self-assembled QDs: A five-band study." *Optical and Quantum Electronics*, vol. 33, no.11, pp. 1131-1137, 2001
26. Mingchu Tang, Jiang Wu, Siming Chen, Qi Jiang, Alwyn J Seeds, Huiyun Liu, Vitaliy G Dorogan, Mourad Benamara, Yuriy Mazur, Gregory Salamo, Optimisation of the defect filter layers in 1.3-μm InAs/GaAs quantum-dot lasers monolithically grown on Si substrates, *Optoelectronic IET*, vol. 9, no. 2, pp. 61-64, 2015
27. V. M. Ustinov, and A. E. Zhukov, GaAs-based long-wavelength lasers, *Semiconductor Science and Technology,* vol. 15, no. 8, pp. R41–R54, 2000

Chapter 4

Silicon-based InAs/GaAs Quantum-dot Superluminescent Diodes

4.1 Introduction

The major differences between the laser and LED, we could define based on optical power aginist current (L-I) measurement and intensity spectrum are superluminescent emission. The emission of superluminescent diode (SLD) has advantage of both high power and wide half maximum bandwidth. Figure 4.1 shows the emission status of LED, SLDs and laser, which a clear threshold point can be found on laser L-I characteristic measurement. However, between the lasing and LED, there is a short region which has the power increasing but not efficient as lasing, leading to superluminescence. In order to inhibit the emission from SLD to lasing, the devices can be fabricated as two sections, in which one is gain and another is absorption, or by tilting the facet of device to reduce the feedback of carriers inside the cavity.

The high power and wide FWHM properties of SLDs can be applied in a wide range of application, such as Optical Coherence Tomography (OCT) [1] and fibre-optic gyroscopes [2]. As a great scan method to indicate the coronary artery disease and applied in ophthalmology diagnose, OCT is widely used in the medical examiner and SLDs is the component to emit the light near infrared.

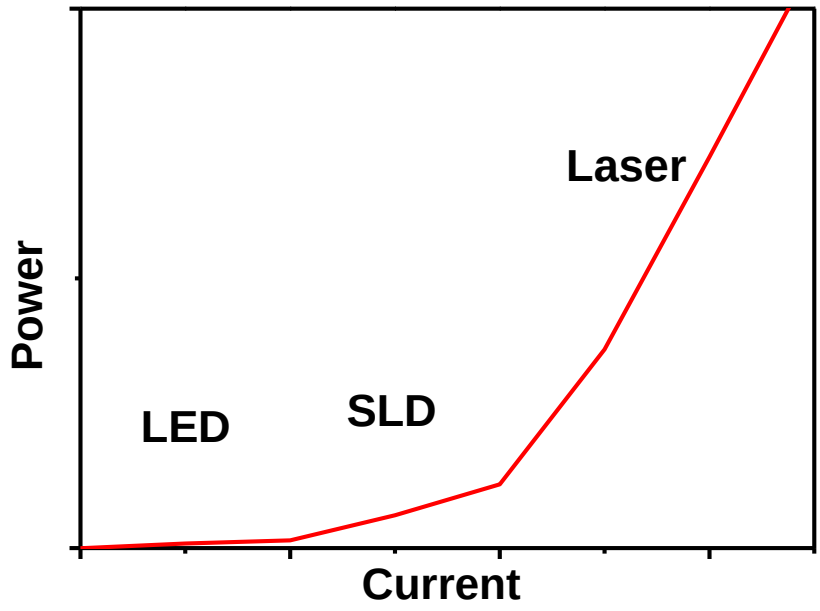

Figure 4.1 L-I characteristic measurement of a typical light emit source to distinguish LED, SLD and laser.

GaAs-based quantum-dot SLDs have been achieved successfully [3, 4] which inspire us to move it on Si platform because the technique of GaAs on Si has been achieved. The motivation of Si-based SLDs is not only the application on OCT industry, but also the SLDs could be integrated on Si based optoelectronic circuits [5]. Recently, SLDs on Si platform has been published by A. Groot *et al*, who demonstrated a multi bandgap SLDs grown on InP substrate and bonding with Si platform with large bandwidth 290 nm [6]. The potential of Si based SLDs attracts researchers to put efforts on it.

4.2 Epitaxial Structure Growth

1 μm of GaAs buffer layer were optimised grown on Si off-cut substrate with (100) 4º oriented to <110> direction. The epi-ready Si substrates have baked in the loadlock chamber for 13 hours under 200 ºC and heated to 500 ºC for 2 hours in the buffer chamber for de-gas, then de-oxidise in the 900 ºC for 10 minutes. The GaAs buffer layer has two steps to grow, first 30 nm GaAs grown at 0.1 ML/s growth rate and around 400 ºC substrate temperature, and the rest of 970 nm GaAs buffer layer were grown at higher temperature and growth rate. The first 30 nm of GaAs layer trapped the major dislocation propagating from the interface of GaAs/Si due to the 4% lattice mismatch and antiphase domain caused by polar to non-polar heteroepitaxial

growth. The rest of 970 nm release the strain which came from GaAs/Si and reduce the high density of dislocation in GaAs buffer layer. It has been proven that the dislocation propagating from the GaAs/Si interface is at density level about 10^{10} cm^{-2} [7].

After GaAs buffer layer, InAlAs/GaAs SLSs DFL has been grown for supressing threading dislocation propagating through to active region and destroy the carrier transition and device performance. InAlAs/GaAs SLSs DFL has been provem as significant method to reduce the density of threading dislocation.[3] Three sets of InAlAs/GaAs SLSs DFLs have been grown with 400 GaAs nm spacing layer between each set of DFL, each set of DFLs consists of 10 repeats of 10 nm InAlAs and 10 nm GaAs. For PL and AFM measurement propose, the test samples with 100 nm AlGaAs/GaAs cladding layer were chosen while1500 nm AlGaAs/GaAs for laser device. 5 layer of InAs/GaAs QDs were grown at optimised temperature which trapped in a GaAs well to form dot-in-well structure (DWELL). Each layer of QDs was annealed to 610 ºC and space with 40 nm GaAs. To form 1.3 μm InAs/GaAs QDs, 3 monolayers of InAs were grown on 2 nm $In_{0.15}Ga_{0.85}As$ and capped with 6 nm $In_{0.15}Ga_{0.85}As$. In order to examine the density and quality of QDs, one layer of uncapped InAs/GaAs QDs grown on the top of surface for AFM measurement propose.

4.3 PL Measurements and Analysis

Power dependent and temperature dependent PL measurements have been made by using our PL system. The samples have been cut to small piece around 9 cm^2 and paste to the copper metal plate with vacuum gel. We first line up and optimise the optical route to obtain the strongest intensity to make sure all the measurements are under identical conditions. The PL sample is excited by a 532 nm green laser from the power range 0.01 mW to 70 mW adjusted by ND filter. The PL spectrum has been measured from 300 K to 10 K with 20 K interval.

Figure 4.2 shows the temperature dependent PL measured with same laser power input at 10 mW. The Peak intensities have kept at same level when the temperatures lower than 160 K but the peak intensities of excited state increase from our measurement which means the more carrier recombination happened in the low temperature because the lower ratio of thermal escape.

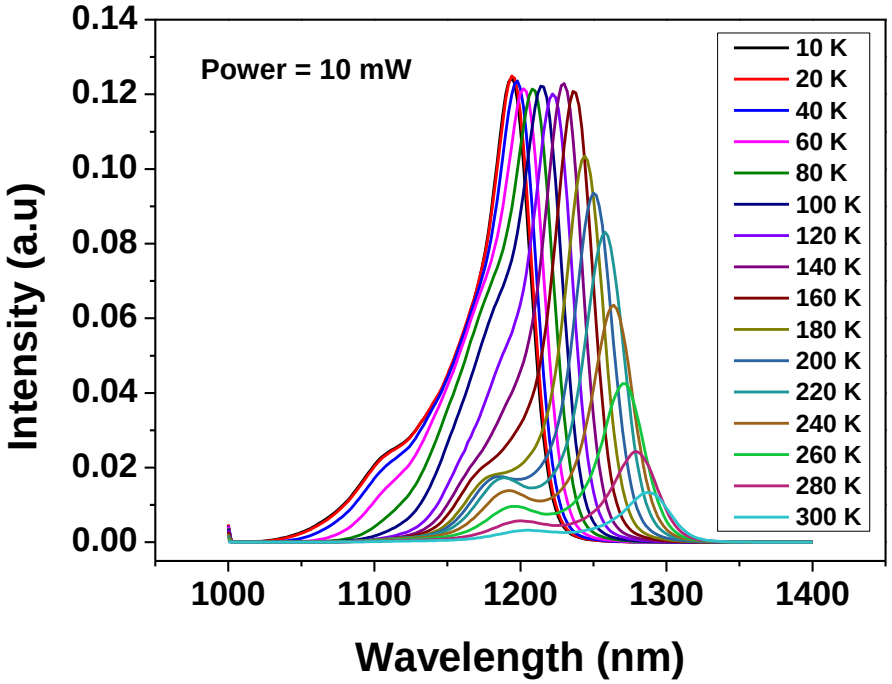

Figure 4.2 Temperature Dependent PL measurement of temperature optimised InAs/GaAs QDs monolithically grown on Si substrate with InAlAs/GaAs SLSs DFL.

The integration of PL intensities could use to determine the thermal active energy, which is factor of device performance in the high temperature. We first integrate the temperature dependent PL for each curve and draw the diagram which is integrate PL intensity against the inverse of temperature (1000/T). The formula to determine thermal active energy is

$$I(T) = \frac{I_0}{1+C_1 e^{-Ea/kT}} \qquad \text{Equation 4.1}$$

where E_a is the thermal activation energies (TAE) for loss mechanisms, which is active at certain temperature ranges, k is the Boltzmann constant, T is the temperature, and I_0 and C_1 are fitting constants.

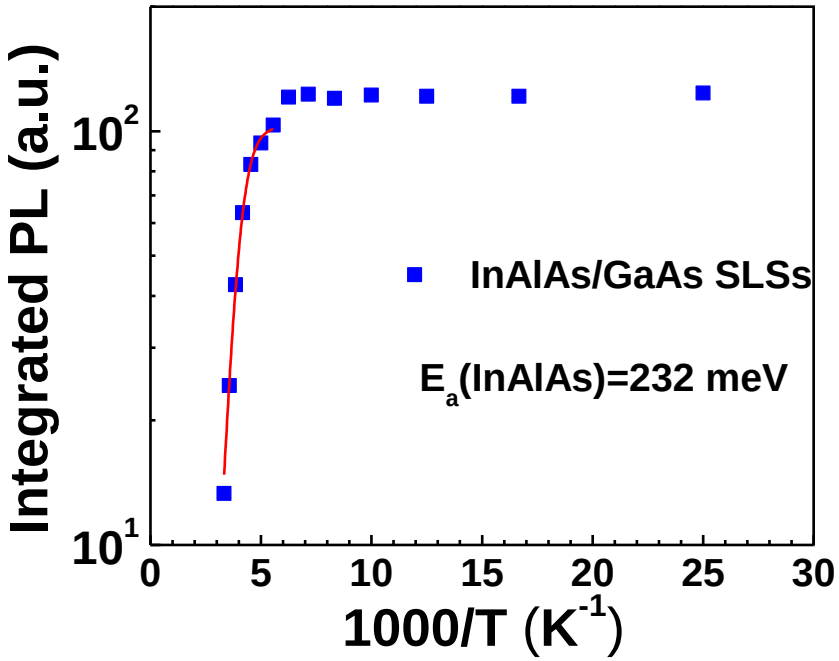

Figure 4.3 Arrhenius plot of integrated PL intensity against the inverse of temperature of InAs/GaAs QDs based on Si substrate. The red line is the fitting with thermal active energy 232 meV.

The Arrhenius plot is fitted the curve, as shown in Figure 4.3. We calculate the thermal activation energy is 232 meV. The Si-based QDs thermal activation energy is similar to Ge-based [8] and GaAs-based QDs [9, 10], which proves the high quality of MBE grown Si based InAs/GaAs QDs.

Figure 4.4 shows the power dependent PL spectra under 10 K temperature condition. The laser power has been increased from 1 to 60 mW in order to observe the excited state emission. The ground state emission at 10 K is around 1190 nm and the intensities are increased with the power of laser from 0.1 mW to 60 mW. The excited state is observed to increase with increasing the excitation power of laser, due to the more carriers trapped in the QDs region. Figure 4.5 have fitted the three peaks of the PL measurement under the 10 K temperature condition and 60 mW laser power input, which three peaks are at 1100 nm, 1129 nm and 1139 nm. The curves we fitted tell us the peak at 1129 nm has the lowest emission and obviously narrower than other than the peak at 1100 nm and similar to 1139 nm. As we know the 1139 nm peak is the ground state emission so the 1129 peak could be another ground state for minor smaller size of QDs

which was proven by our AFM measurements and figure 4.6. Figure 4.6 shows the normalisation of the PL spectra based on figure 4.4 and we can clearly observe the 1129 nm peak was excited when the laser power more than 40 mW. There are only two peaks which are ground state and excited state when the power of laser below 40 mW. The slight red shift in the measurements is due to the laser heated up the sample with high power of laser. The two states of QDs could bring the SLD large FWHM, which will benefit to SLD. We can found our SLD has large FWHM in the laser measurements.

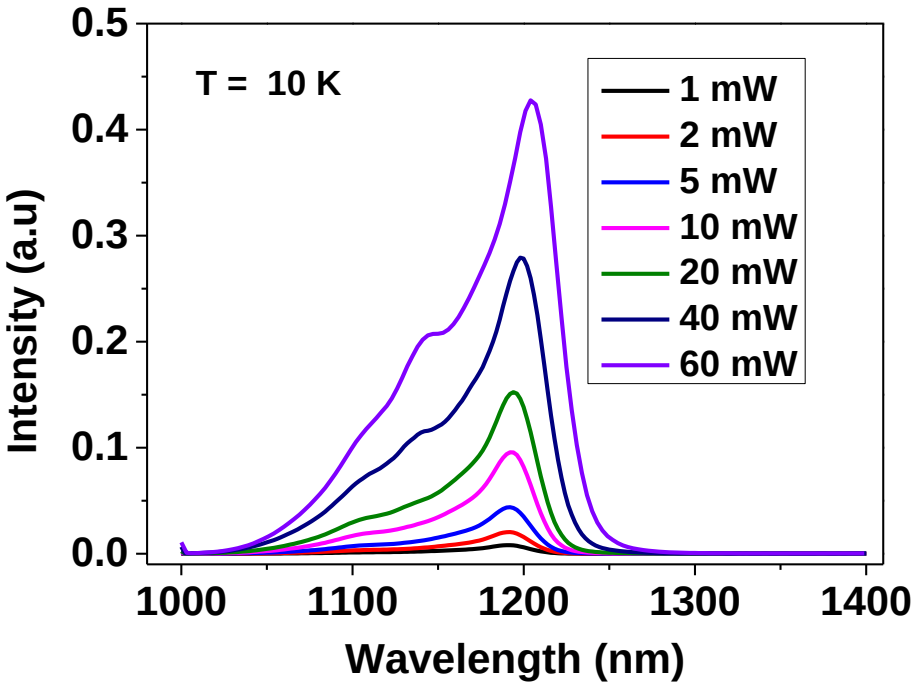

Figure 4.4 Power Dependent PL measurement of temperature optimised InAs/GaAs QDs monolithically grown on Si substrate with InAlAs/GaAs SLSs DFL.

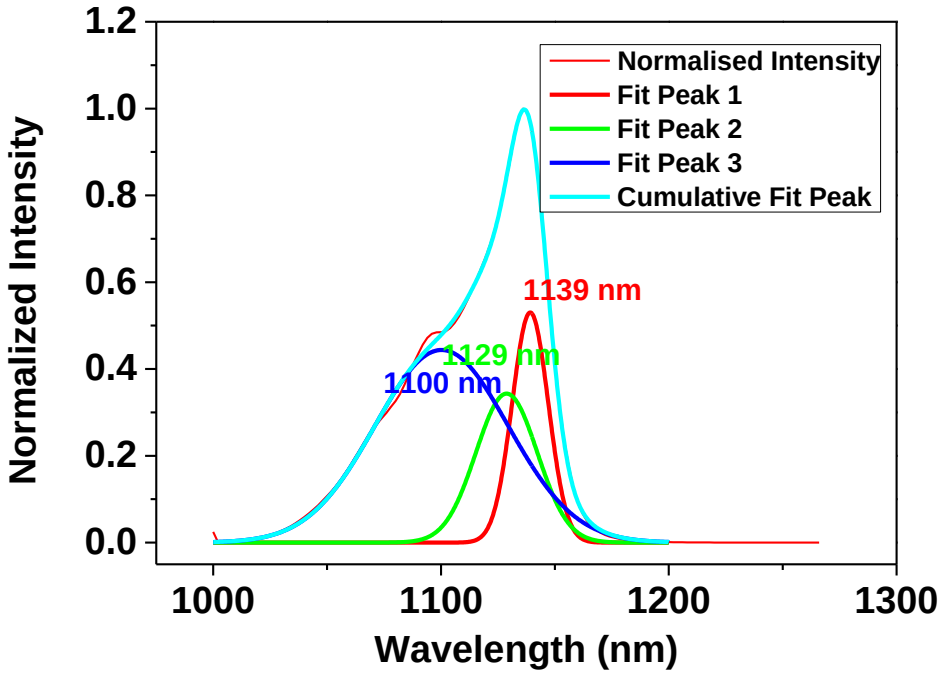

Figure 4.5 PL measurements of InAs/GaAs QDs on Si substrates with 10 K temperature condition and 60 mW power input. The 3 state emission PL has been fitted to three peaks which are at 1100 nm, 1129 nm and 1139 nm.

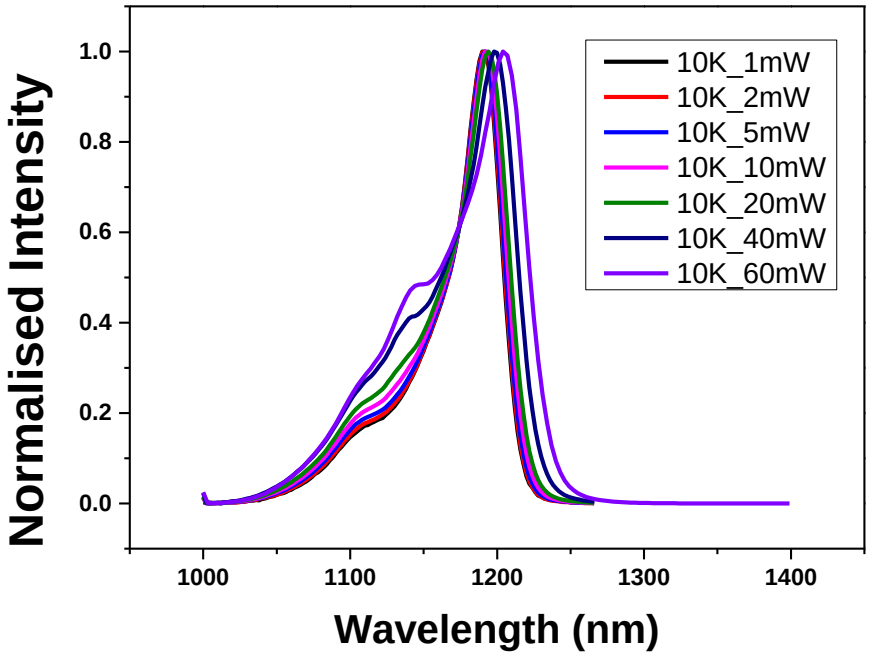

Figure 4.6 Normalised power dependent PL measurements of InAs/GaAs QDs on Si substrate under the 10 K temperature condition. The power range is from 1 mW to 60 mW.

4.4 High Density QDs Growth

AFM is used here to examine the morphology of InAs/GaAs QDs and the defects densities. The number of QDs density could contribute the high gain value of light emitting source including laser and SLD. By lowering the growth temperature of QDs, the density of QDs is significantly increase to ~4.1×10^{10} cm^{-2} and QD defects density measured by AFM is around 7×10^{8} cm^{-2}. The reason why we observe the higher QDs density is due to the lower temperature of QDs nucleation. The lower nucleation temperature could attract more QDs stick on the sample surface. However, it also could introduce more point defects in the QDs and it can be solved by reducing the InAs from 3 ML to 2.7 ML. From our experiment, we optimise the InAs/GaAs QDs grow at 510 ˚C with 2.7 ML deposition.

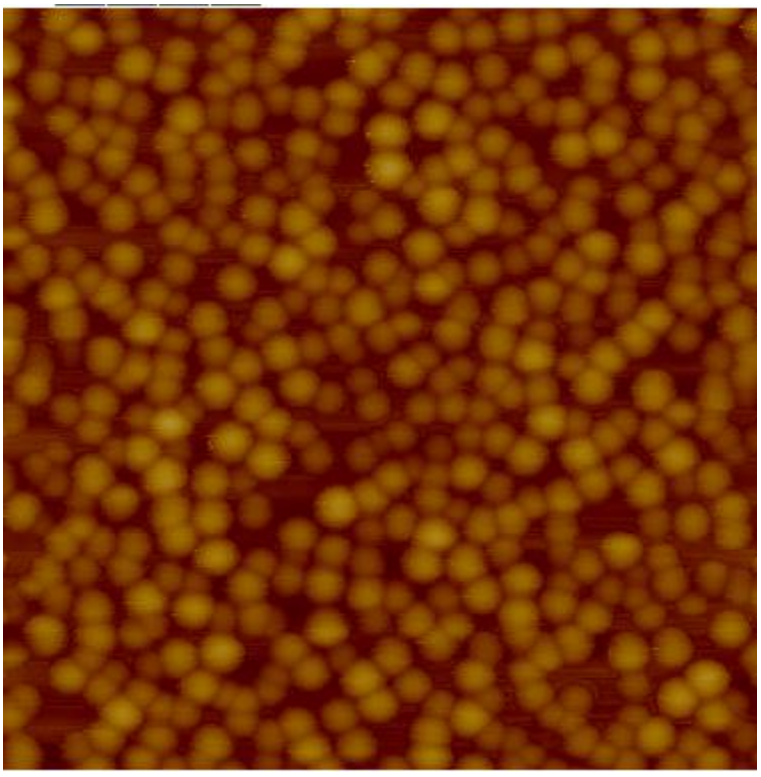

Figure 4.7 1µm × 1µm InAs/GaAs QDs AFM images with dot density 4.13×10^{10} cm^{-2}

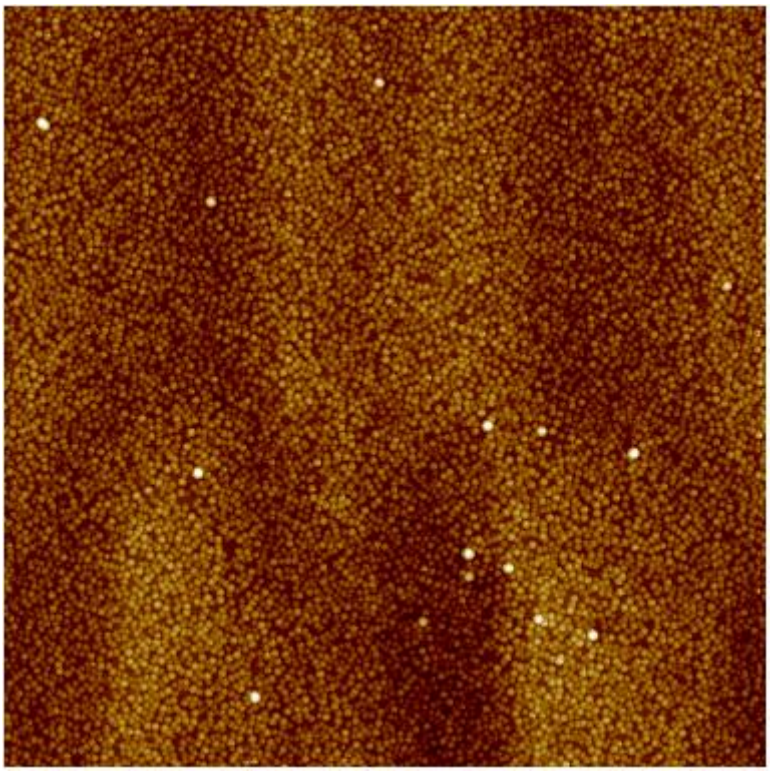

Figure 4.8 5µm × 5µm InAs/GaAs QDs AFM images with defects density 6 × 10^9 cm^{-2}

InAlAs/GaAs SLSs DFL has been examined as a significantly method to filter the threading dislocations from ~10^{10} to 1.0 × 10^6 cm^{-2} which have been discussed in last chapter. From our TEM measurement, QDs region shows that there is no defects propagating from the substrate. In the figure 4.9, we compare the two types of InAs/GaAs QDs which grown at 520 ˚C and 510 ˚C in PL measurement. The PL measurements clearly show that the QDs grown at 510 ˚C has the strongest intensity emission and more separation between the ground state and excited state. The larger separation between the ground state and excited state means the higher thermal energy required to excite carriers from ground state to excited state, it develops the performance in the high temperature.

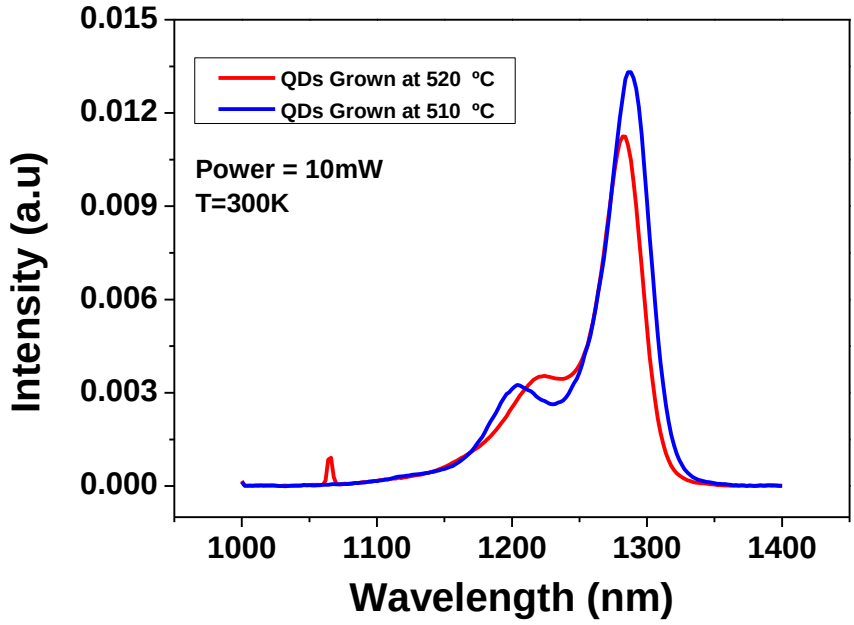

Figure 4.9 PL comparison of different temperature growth of QDs by MBE. The QDs grown at 10-degree lower cause higher peak intensity of PL emission.

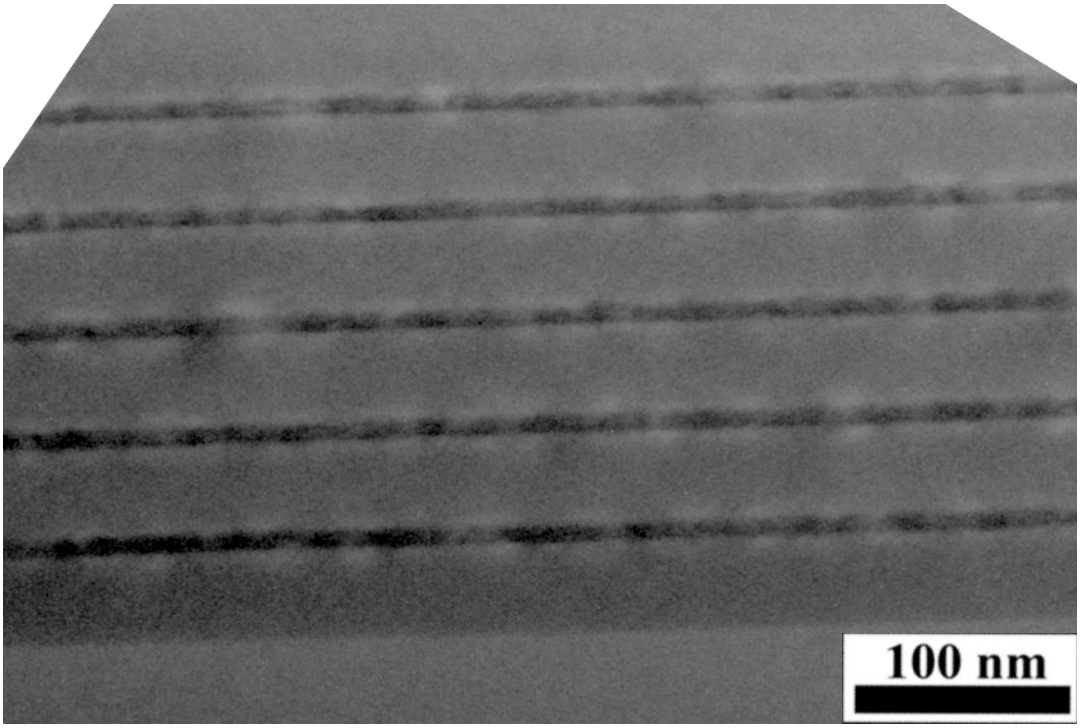

Figure 4.10 High resolution TEM image of 5 layers of InAs/GaAs QDs grown on Si substrate without any defects. Each layers of QDs are grown on 2 nm InGaAs and capped with 6 nm InGaAs. The TEM images were measured by University of Arkansas.

4.5 Device Fabrication and Results

The SLD devices were grown at n-doped Si off-cut substrate with (100) 4º oriented to <110> direction. 1 μm of Si-doped optimised GaAs buffer layer was grown on Si substrate, followed by five sets of InAlAs/GaAs SLSs DFL grown on the GaAs. Each set of InAlAs/GaAs SLSs DFLs has 5 repeats of 10 nm of InAlAs and 10 nm of GaAs to form one layer of superlattices and GaAs 300 nm spacing layer between each set of DFLs. One 300 nm of GaAs n-type contact layer which will be etched down from the top of sample. 1500 nm of n-type AlGaAs cladding layer and n-type guiding layer of 10 repeats AlGaAs/GaAs SLSs were grown before the 5 layers of InAs/GaAs DWELL structure. Same P-type of AlGaAs cladding layer and AlGaAs/GaAs SLSs were grown on the top and 300 nm P-type GaAs contact layer for electrode propose.

The SLD was fabricated in a two-section ridge-waveguide structure following standard ridge-waveguide laser pro-cessing. 20-μm-wide ridges were defined by wet etching to a depth of 1.6 μm (i.e. 200 nm above the active region). Two sections were electrically isolated by shallow etch of highly p-doped GaAs contact layer, providing a resistance of ~2 kΩ between adjacent contacts. Ti/Pt/Au and InGe/Au metal contact layers were deposited on the p-GaAs contacting layer and the exposed n-GaAs buffer layer, respectively. A schematic of the two-section SLD is shown in Figure 4. The device consists of a 2-mm long gain section and a 1-mm long absorber, which was reverse biased while electrically driving the gain section to inhibit lasing. No facet coating was applied.

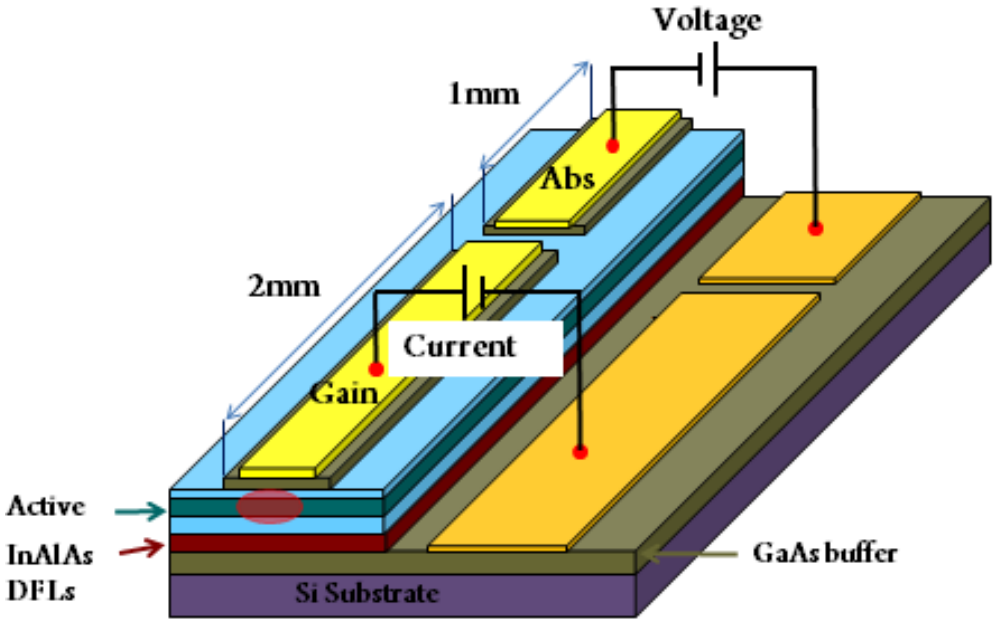

Figure 4.11 Schematic diagram of InAs/GaAs QDs SLD grown on Si substrate with two sections: gain and absorption. The N type GaAs contact were etched down through the whole p-i-n region.

It is necessary to examine the material growth could work function as laser but not only LED. the device has been first fabricated as a laser diode, which examined by L-I characteristic measurement shown at Figure 4.12. A clear threshold current point found during the L-I characteristic measurement. The inset of Figure 4.12 shows the spectrum of laser emission around 1250 nm.

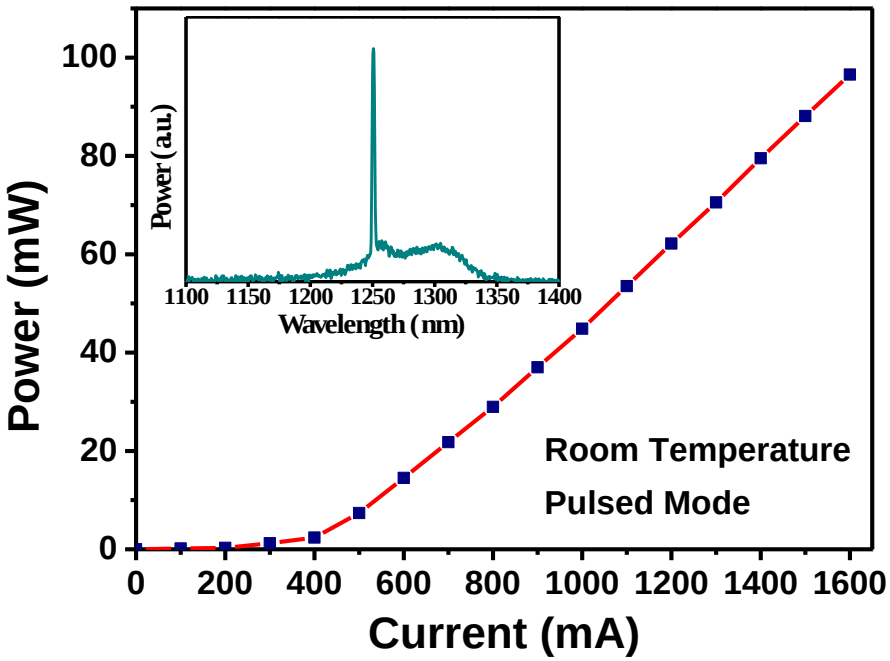

Figure 4.12 L-I characteristic of InAs/GaAs QDs laser grown on Si substrate under pulsed operation at room temperature. The inset shows the lasing spectrum just above the threshold current. The laser fabricated as 3-mm length and 50 μm ridge width.

SLD has the function of wider FWHM and stronger intensity when the injection current increase which has been proved in Figure 4.13. The inset of Figure 4.13 shows the integration of EL measurement is increasing exponentially which means the gain section is working properly with high injection current. The power spectrum presented by Figure 4.13 is operated under pulsed mode with 5% duty-cycle and 10 μs pulsed width at room temperature.

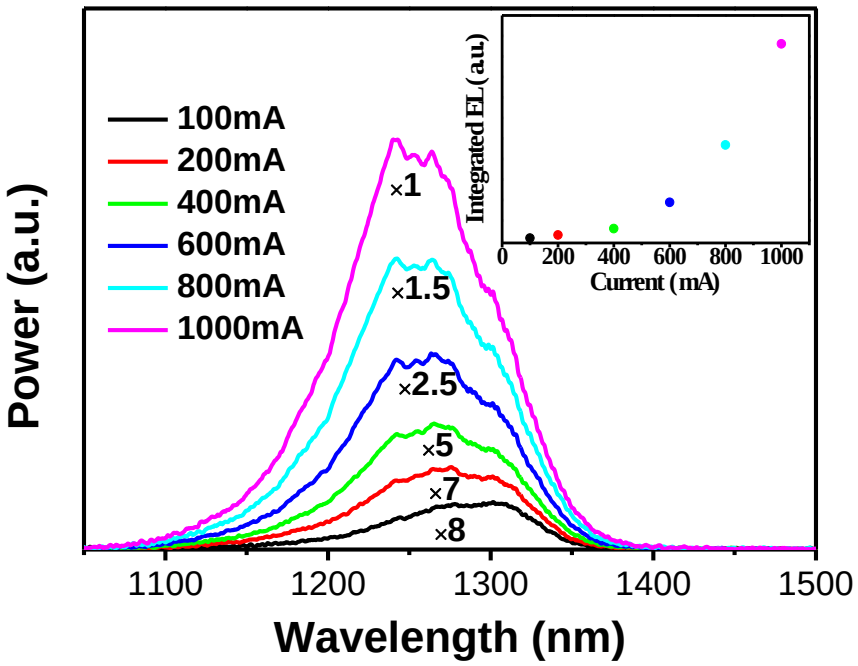

Figure 4.13 Output power spectrum as a function of the injection current under pulsed operation (5% duty-cycle and 10 μs pulse-width) measured at room temperature. The inset plots the integrated intensity measured from the emission spectrum against the injection current.

With low injection current, the SLD emission is dominated by the ground-state, which causes a broadband emission centred at 1280 nm with FWHM of 101 nm (Figure 4.14). With the injection current increase until 800 mA, an increasing FWHM with 114 nm and blue shift of centred wavelength with 20 nm. This could be due to the smaller dots are filled with carriers when injection currents go up so that the FWHM become larger and blueshift appears. Once the injection current arrives 1000 mA, the FWHM fall to 111 nm which probably due to a non-uniform increase in gain for different size of dots takes place and introduce a narrowing FWHM.

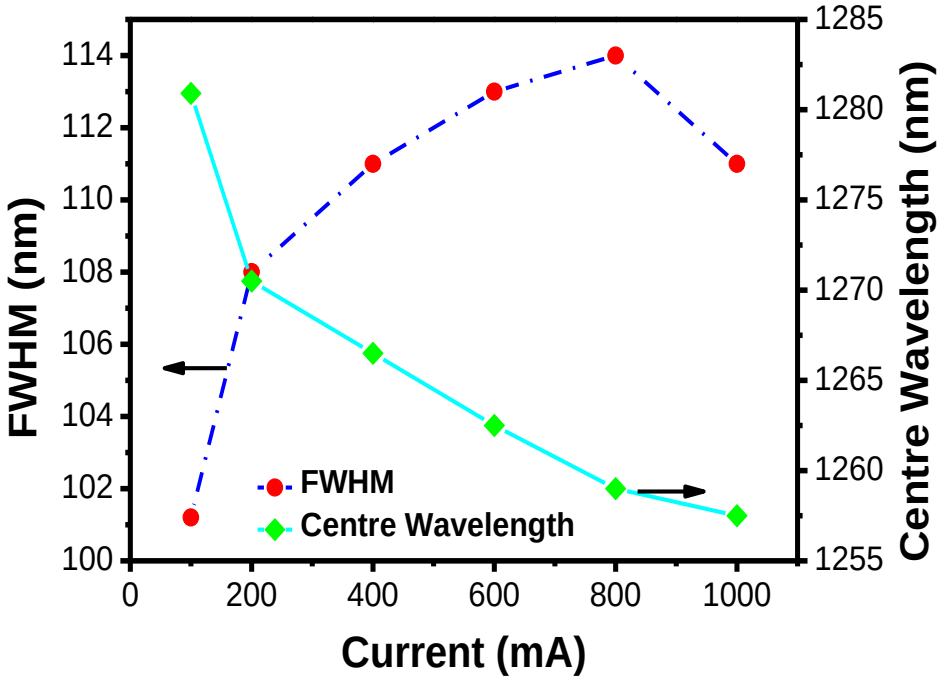

Figure 4.14 Plot of the evolution of the full-width half maximum and the centre wavelength against the injection current. The FWHM is increasing with the injection current until 800 mA and the centre wavelength blue shift when injection current increase.

The L-I characteristic measurements (Figure 4.15) shows the superluminescent emission from 20 to 40 ˚C. The fabricated InAs/GaAs QDs SLD monolithically grown on Si substrate was bar-tested and directly probed without any mounting and bonding. There is no active cooling applied during the measurement. The 2-mm long gain section are pumping electrically under pulsed mode with the 1-mm long absorber reversed biased at a voltage of 1 V. The curve of L-I characteristic measurements with the temperature increment. At 1000 mA injection current, a 2.6 mW of output power has been obtained. The output power has the potential to be improved because the there is no coating and polishing based on the as-cleaved facet and the substrate itself has 4˚ offcut. The SLD's output power went down to 0.5 mW once the temperature more than 40 ˚C.

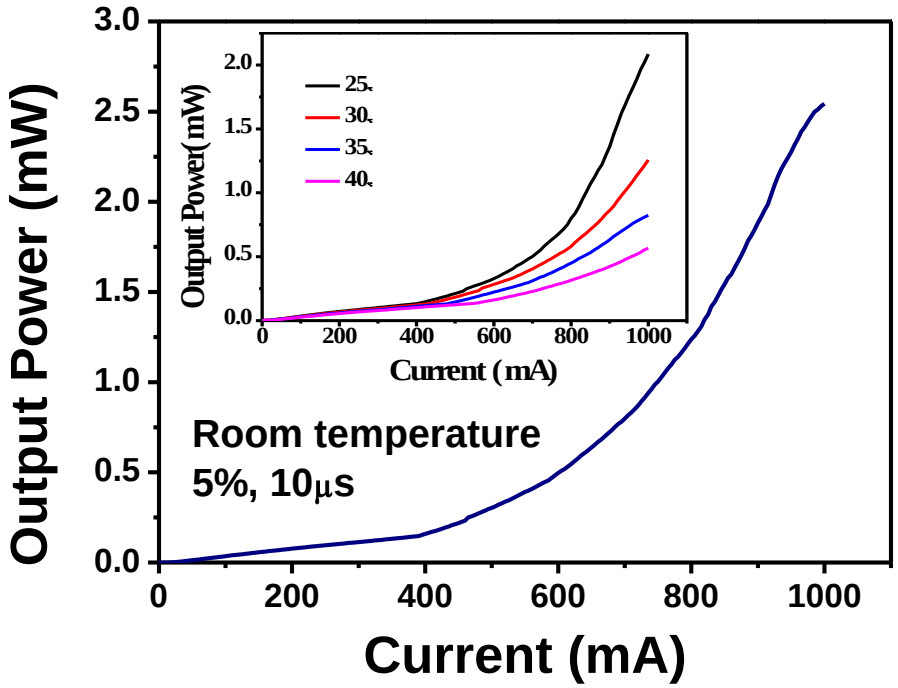

Figure 4.15 L-I characteristic measurements of InAs/GaAs QDs SLD monolithically grown on Si substrate under pulsed mode with temperature range from 20 to 40 ˚C (inset). The output power is normalised to CW.

4.6 Conclusion

The first QD SLD monolithically grown on Si substrate has been achieved under pulsed mode and the maximum power measured is 2.8 mW with injection current 1000 mA. However, the maximum operating temperature is only 40 ˚C and pulsed operation mode restricts the application of our SLD. To improve the performance, a facet polishing and anti-reflection coating could increase the output power. Also during the high temperature condition, the ratio of auger recombination and non-radiative recombination increase significantly appeared because the heteroepitaxy growth of GaAs on Si and thermal crack, the solutions can be applied p-doped to increase the resistance of thermal.

We found out after the injection current over than 900 mA the FWHM decrease to 111 nm and this can be solved by using chirped QDs [12], QDs intermixing [13] or hybrid QW/QDs structure [14]. By using InAlAs/GaAs SLSs DFL, the threading dislocation density has been significantly reduced to 10^6 cm^{-2} levels. Compare with the bonding method, monolithically

growth still need to solve the issue of thermal crack, which happened on III–V material on Si substrate.

To implement SLD on the optoelectronic integration, the function of amplifier is the next stage to be optimised and improved. Currently semiconductor optical amplifier (SOA) could use bonding technique to integrate with laser source but cannot be monolithically grown. SLD will be the key to solve the problem of Si based optical amplifier for the next stage.

Reference

1. T. H. Ko, D. C. Adler, J. G. Fujimoto, D. Mamedov, V. Prokhorov, V. Shidlovski, S. Yakubovich, "Ultrahigh resolution optical coherence tomography imaging with a broadband superluminescent diode light source," *Optics Express*, vol. 12, no. 10) pp. 2112–2119, 2004
2. W. K. Burns, C. L. Chen, R. P. Moeller, "Fiber-optic gyroscopes with broad-band sources," *Journal of Lightwave Technology*, vol. LT-1, no. 1, pp. 98–105, 1983
3. S. M. Chen, K. J. Zhou, Z. Y. Zhang, D. T. D. Childs, M. Hugues, A. J. Ramsay, and R. A. Hogg, "Ultra-broad spontaneous emission and modal gain spectrum from a hybrid quantum well/quantum dot laser structure," *Applied Physics Letters*, vol. 100, no. 4, pp. 041118, 2012
4. Siming Chen, Kejia Zhou, Ziyang Zhang, Jonathan R. Orchard, David T. D. Childs, Maxime Hugues, Osamu Wada and Richard A. Hogg, "Hybrid Quantum Well/Quantum Dot Structure for Broad Spectral Bandwidth Emitters," *IEEE Journal Of Selected Topics in Quantum Electronics*, vol. 19, no. 4, pp. 1900209, 2013
5. Kristian M. Groom, Benjamin J. Stevens, Punima D. L. Greenwood, David T. D. Childs, John S. Roberts, Matthew Lomas, Maxime Hugues, Hifsa Shahid and Richard Hogg, "A platform for GaAs opto-electronic integrated circuits based on GaAs/AlGaAs regrowth upon patterned InGaP," *Proc. SPIE*, vol. *7616*, 2010,
6. A. De Groote, J. D. Peters, M. L. Davenport, M. J. R. Heck, R. Baets, G. Roelkens, and J. E. Bowers, "Heterogeneously integrated III–V-on-silicon multibandgap superluminescent light-emitting diode with 290 nm optical bandwidth," *Optics Letter s*,vol. 39, no. 16, pp. 4784-4787, 2014
7. M. Tang, S. Chen, J. Wu, Q. Jiang, V. G. Dorogan, M. Benamara, Y. I. Mazur, G. J. Salamo, A. Seeds, and H. Liu, "1.3-μm InAs/GaAs quantum-dot lasers monolithically grown on Si

substrates using InAlAs/GaAs defect filter layers," *Optics Express*, vol. 22, no. 10, pp. 11528–11535, 2014

8. Y. Y. Liang, S. Yoon, C. Y. Ngo, W. K. Loke, and E. A. Fitzgerald, "Characteristics of InAs/InGaAs/GaAs QDs on GeOI substrates with single-peak 1.3 μm room-temperature emission," *Journal of Physics D: Applied Physics*, vol. 45, pp. 145103, 2012
9. B. Ilahi, L. Sfaxi, and H. Maaref, "Optical investigation of InGaAs-capped InAs quantum dots: Impact of the strain-driven phase separation and dependence upon post-growth thermal treatment," *Journal of Luminescence*, vol. 127, pp. 741–746, 2007
10. Z. Y. Xu, Z. D. Lu, Z. L. Yuan, X. P. Yang, B. Z. Zheng, J. Z. Xu, W. K. Ge, Y. Wang, J. Wang, L. L. Chang, "Carrier relaxation and thermal activation of localized excitons in self-organized InAs multilayers grown on GaAs substrates," *Physical Review B*, vol. 54, pp. 11528, 1996
11. S. M. Chen, M. C. Tang, Q. Jiang, J. Wu, V. G. Dorogan, M. Benamara, Y. Mazur, G. Salamo, P. Smowton, A. Seeds and H. Liu, "InAs/GaAs quantum-dot superluminescent light-emitting diode monolithically grown on a Si substrate," *ACS Photonics*, vol. 1. No. 7, pp. 638–642, 2014
12. X. Li, P. Jin, Q. An,Z. Wang, X. Lv, H. Wei, J. Wu, and Z. Wang, "Improved Continuous-Wave Performance of Two-Section Quantum-Dot Superluminescent Diodes by Using Epi-Down Mounting Process," *IEEE Photonics Technology Letters*, vol. 24, pp. 1188-1190, 2012
13. Z. Zhang, R. A. Hogg, B. Xu, P. Jin, and Z. G. Wang, "Realization of extremely broadband quantum-dot superluminescent light-emitting diodes by rapid thermal-annealing process," *Optics Letters*, vol. 33, no. 11, pp. 1210-1212, 2008
14. S. Chen, K. Zhou, Z. Zhang, D. T. D. Childs, M. Hugues, A. Ramsay and R. A. Hogg, "Ultra-broad spontaneous emission and modal gain spectrum from a hybrid quantum well/quantum dot laser structure," *Applied Physics Letters*, vol. 100, pp. 041118-041118-3, 2012

Chapter 5

Optimisation of InGaAs/GaAs SLSs DFLs

5.1 Introduction

After we investigated InAlAs/GaAs strain-layer superlattices (SLSs) defects filter layers (DFLs) in chapter 3, significant improvements on threshold current density and operating temperature on laser devices have been achieved due to the higher bonding energy between Al and As atoms. Compare with InGaAs/GaAs SLSs DFLs, InAlAs/GaAs SLSs DFLs is also a choice to be implemented in III–V/Si materials system. However, oxidation is easy to occur in aluminium related semiconductor compounds which is capable to damage the laser devices performance. The concern motives us to focus on the InGaAs/GaAs SLSs DFLs again with detail study. Regards to the previously report by T. Wang, InGaAs/GaAs SLSs DFLs have been proved as a considerable choice in III–V/Si material [1], but it still has a lot of room to be improved. So in the chapter, we are not going to compare different types of DFLs but focus on the optimisation of InGaAs/GaAs SLSs DFLs.

The optimisation processes include three steps,

1. Different GaAs spacer layer growth method;
2. Modify different indium composition in $In_xGa_{1-x}As$ /GaAs SLSs;
3. Verity different GaAs thickness in $In_xGa_{1-x}As$/GaAs SLSs

In this study, we introduce growth method I and II which are examined by atomic force microscopy (AFM), photoluminescence (PL), transmission electron microscopy (TEM) and laser device performances. The indium composition and GaAs thickness in $In_xGa_{1-x}As$/GaAs SLSs are both modified as well.

5.2 MBE Growth

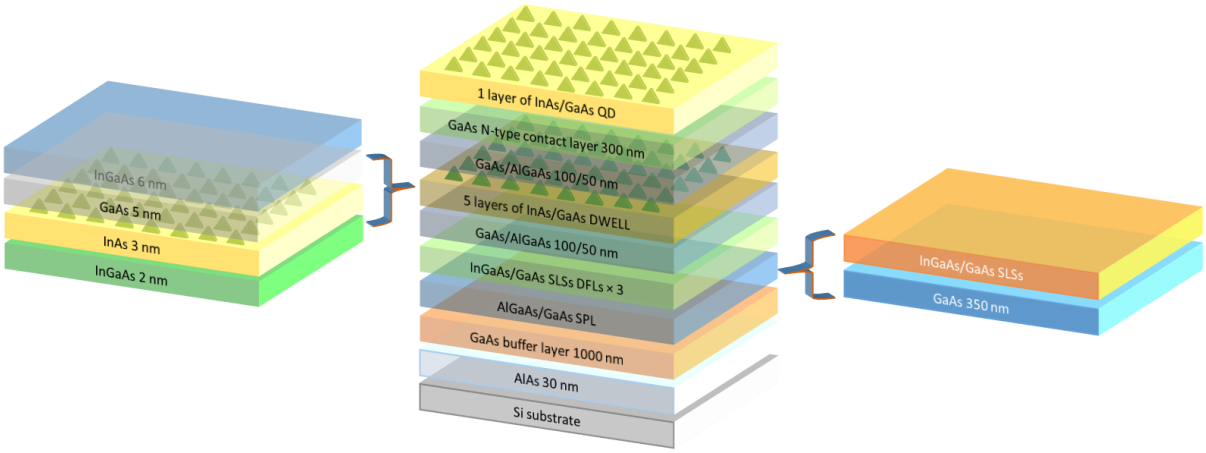

Figure 5.1 Schemtic diagram of InAs/GaAs QDs monolithically grown on Si substrate with 3 sets of InGaAs/GaAs SLSs DFLs. The top layer of InAs/GaAs QDs is for AFM measurements propurse.

The QDs structures were grown by solid-source molecular beam epitaxy (MBE). As shown in the schematic image in Fig. 5.1, 5 layers of InAs/GaAs QDs were monolithically grown on n-doped Si substrate (100) with 4° offcut oriented to <110> by introducing a 1 μm GaAs buffer layer and 3 sets of InGaAs/GaAs SLSs DFLs. Before the growth, oxide desorption of Si substrates was performed at 900 °C for 20 minutes. Then the 1 μm GaAs buffer layer was grown in two steps, 30 nm at low temperature of 380 ˚C and growth rate of 0.1 monolayers/s (ML/s), followed by 970 nm GaAs grown at high temperature at growth rate of 0.7 ML/s. The two-step growth helps to block APDs and part of the threading dislocations, which are caused by the GaAs/Si polar to non-polar growth. To further reduce the threading dislocation density, 3 sets of InGaAs/GaAs SLSs DFLs were grown and each set of DFLs was separated by a 350 nm GaAs spacing layer. 5 period of InGaAs/GaAs SLSs formed one set of DFL. To improve the efficiency of $In_xGa_{1-x}As$/GaAs DFLs, we introduced different growth method for the DFLs. As shown in Fig. 5.2, in the growth method I, GaAs spacing layer was grown during the period of heating up to 610 ˚C after InGaAs/GaAs SLSs growth at 420 ˚C. The difference in growth methods II is that the GaAs spacing layer was grown after heating up to 610 ˚C. It has been proved that low temperature growth of $In_xGa_{1-x}As$/GaAs SLSs could significantly reduce the threading dislocation density [2]. The impact of indium composition and GaAs thickness have

also been studied using x = 16, 18 and 20 for indium compositions and 8, 9 and 10 nm for GaAs thickness.

InAs/GaAs dot-in-well (DWELL) structure forms the active region which consists of 5 layers of InAs/GaAs QDs [3]. Each layer of InAs/GaAs QD is formed by 3 ML of InAs grown on 2 nm of InGaAs. The QDs are formed by S-K growth mode. The growth rate of InAs is 0.1 ML/s with nucleation teamperature 510 °C. 6 nm of InGaAs were used to cap the QDs, followed by 5 nm of GaAs. Between the each layer of InAs/GaAs QDs, 45 nm of GaAs spacer layer were grown at 580 °C [4]. The The DWELL were embedded between two 100-nm GaAs layers grown at 580 °C and 50-nm AlGaAs layers grown at 610 °C. The growth of InAs/GaAs QDs was monitored by refection high-energy electron diffraction (RHEED) where the 3-dimensional islands were observed around 1.7 to 1.8 ML of InAs deposition.

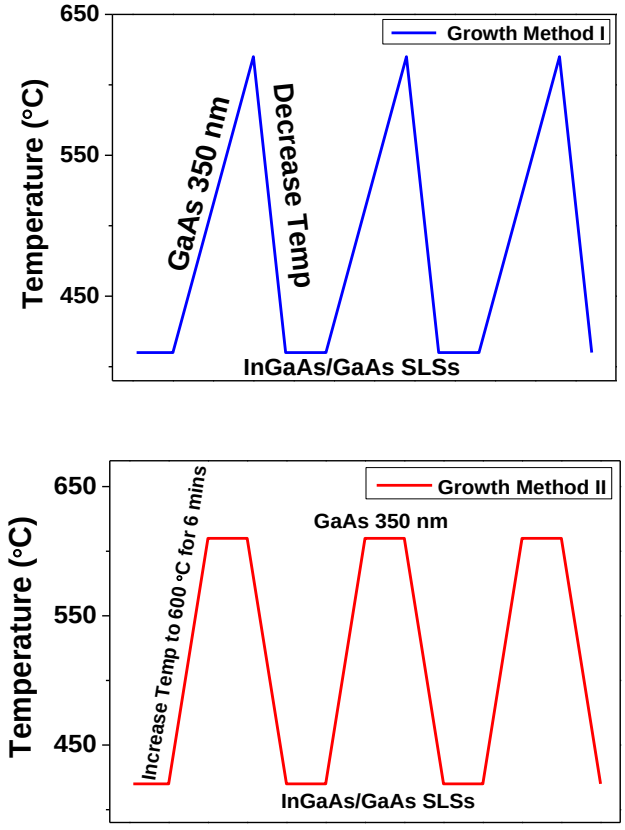

Figure 5. 2 Two different growth methods of DFLs; Growth method I: grow GaAs space layer during the ramp-up of temperature from 420 to 610 ˚C and then cool down to 420 ˚C for InGaAs/GaAs SLSs growth; Growth method II: grow GaAs spacer layer at a stable temperature of 610 ˚C and then cool back to 420 ˚C for InGaAs/GaAs SLSs.

Sample	Growth type	$In_xGa_{1-x}As$	GaAs Thickness	QD density ($\times 10^8$ cm^{-2})	PL peak intensity
A	I	x = 18	10 nm	258	1.2
B	II	x = 18	10 nm	365	4
C	II	x = 16	10 nm	269	2.6
D	II	x = 20	10 nm	268	2.2
E	II	x = 18	9 nm	387	3.9
F	II	x = 18	8 nm	280	2

Table 5.1 The QDs densities and PL peak intensity of different growth types, indium composition and GaAs thickness.

As shown in Table 5.1, 6 samples have been grown. Sample A has go through growth method I, where GaAs spacer layer grow during the heating from 420 °C to 610 °C, indium composition 18 % and GaAs thickness 10 nm. Compare with sample A, Sample B has been experienced growth method II, where GaAs spacer layer grow at stable temperature 610 °C. Sample C and D have adjusted indium composition to 16% and 20 %. Sample E and F have modified the GaAs thickn**es**s in SLSs to 9 nm and 8 nm.

5.3 Atomic Force Microscopy Measurements

Figure 5.3 shows the 1 μm × 1 μm AFM images of samples A to F. It clearly shows that sample B and E have the highest QDs density compare with other four samples which are 365 and 387 × 10^8 cm^{-2} respectively. Sample A and D have the lowest QD density 258 × 10^8 cm^{-2}. The improvement on QDs density from Sample A to Sample B shows growth method II provides better crystal quality. If we compare sample B, C and D, the QDs density shows indium composition 18% provides the best condition of QD growth so as 9 nm and 10 nm of GaAs thickness to 8 nm.

The 5 μm × 5 μm AFM images of samples A to F are presented in figure 5.4. The AFM images with larger scale could tell the morphology of the growth of III–V materials on Si substrate. At this point, sample A to E have similar performance and sample F shows the worst morphology. The white dots are the defects which will increase the non-uniformity of QDs.

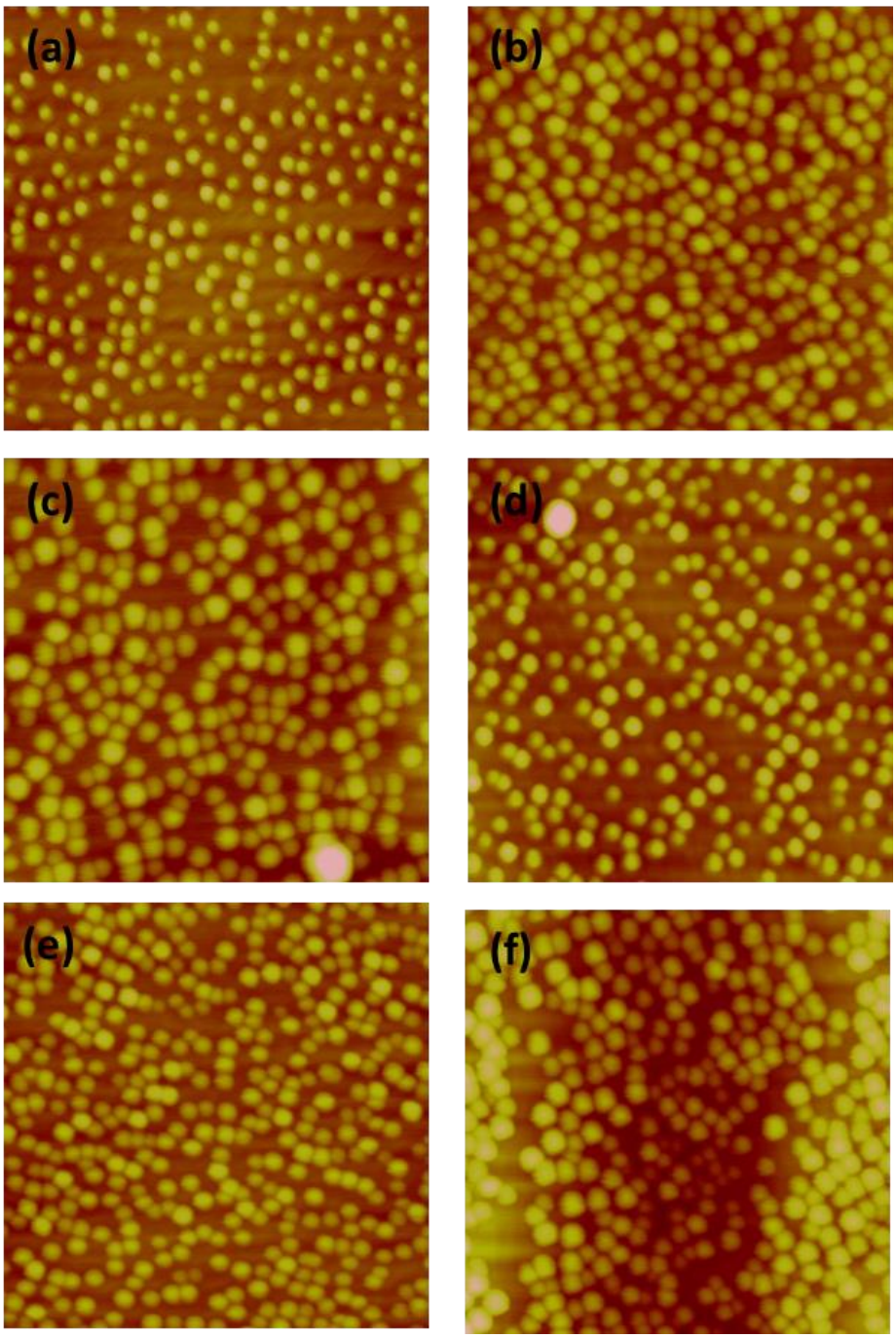

Figure 5.3 1 µm × 1 µm AFM images of InAs/GaAs QDs. Images (a) to (f) are corresponding to sample A to F from table 5.1.

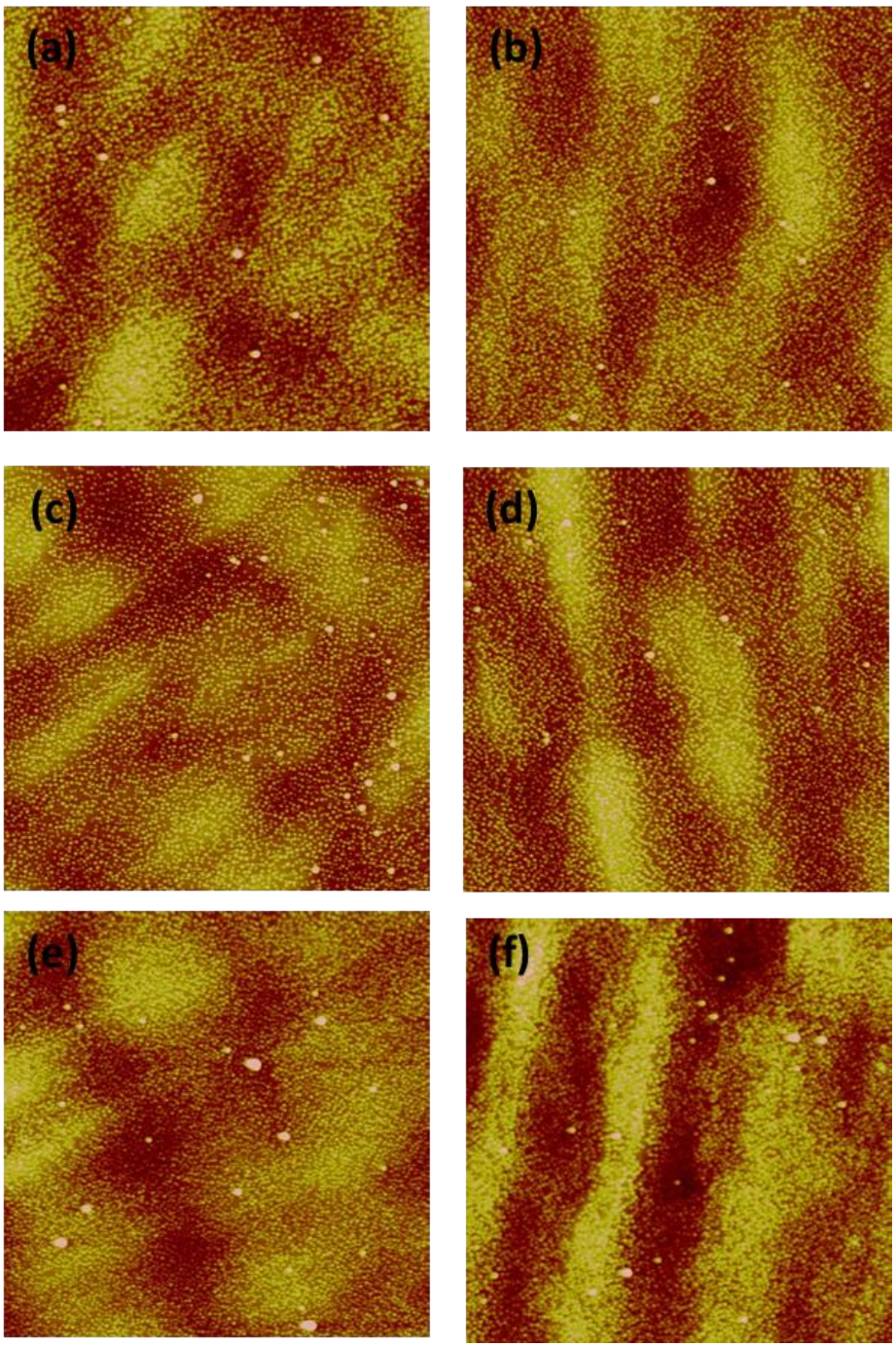

Figure 5.4 5 µm × 5 µm AFM images of InAs/GaAs QDs. Images (a) to (f) are corresponding to sample A to F from table 5.1

5.4 Photoluminescence Measurements

We have used room-temperature PL measurements to compare each sample which were done by using the RPM-2000 PL mapping system. The measurements were undertaken under same condition. Figure 5.5 presents the sample A and B comparison. Sample B has almost three times stronger than sample A at ground state on PL peak intensity. Combine with the AFM

measurements, the stronger PL emission is not only due to the higher density of QDs, but also proves the GaAs high temperature growth (growth method II) improves the crystal quality significantly. At high temperature of GaAs, the threading dislocations will increase the possibility to encounter so that threading dislocations will be eliminated or merged.

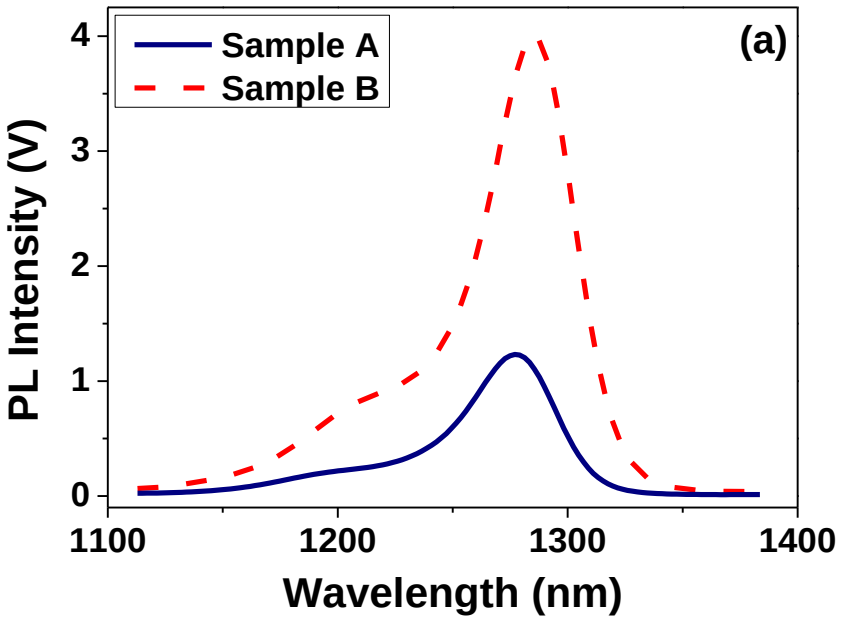

Figure 5.5 Room-temperature PL spectra comparison of growth method I (sample A) against growth method II (sample B).

Figure 5.6 shows the comparison of different indium composition (x) in $In_xGa_{1-x}As$/GaAs SLSs DFLs. Sample B (x= 18%) presents the strongest PL emission on ground state, which is almost double the sample D's. This is due the good balance between the strain and the efficiency of blocking threading dislocations. The higher indium composition will increase the strain in SLSs, and hence it will benefit to blocking threading dislocations. On the other hand, the higher strain could generate extra dislocations itself once the InGaAs thickness is close to the critical thickness of dislocation formation. The balance between strain and blocking threading dislocations is studied here which proves indium composition 18% is the best solution to $In_xGa_{1-x}As$/GaAs SLSs DFLs. Sample C's PL emission is slightly higher than sample D. These are due to the indium composition at 20% could introduce extra threading dislocation which affects the samples luminescence behavior.

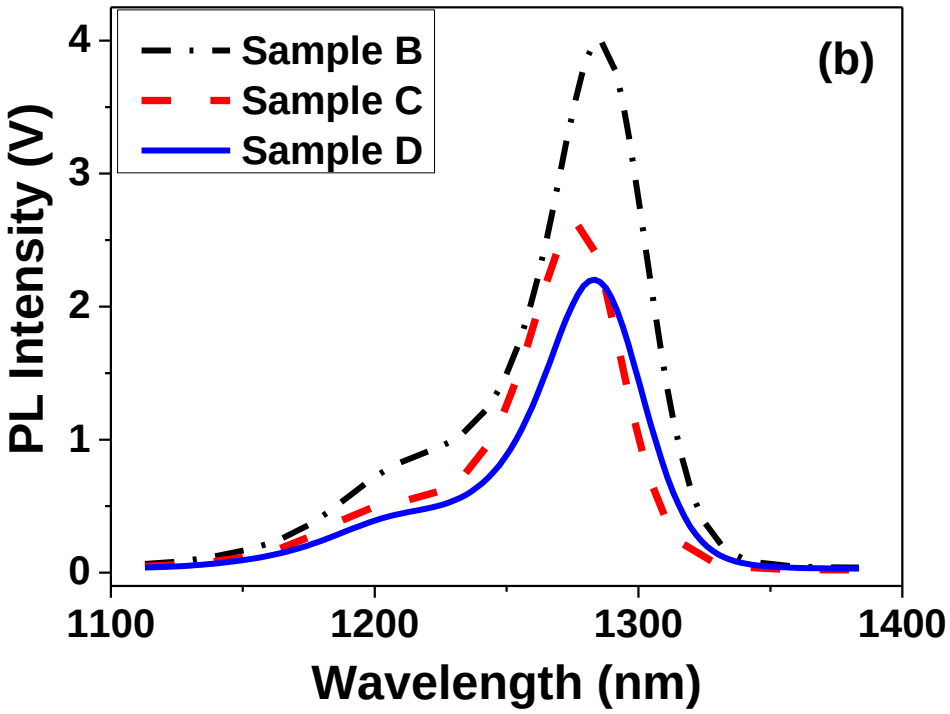

Figure 5.6 Room-temperature PL spectra comparison of indium composition 18% (sample B), 16% (sample C) and 20% (sample D)

Figure 5.7 shows the PL spectrum comparison of GaAs thicknesses 8, 9 and 10 nm. Sample B and E have similar performance only sample E is slightly lower than sample B. The AFM measurements prove these two samples have similar QD density as well. Sample F has almost half lower of PL emission compare with sample B and E. The QD density of sample F is also much lower than sample B and E. 9 nm of GaAs has maximum relax the strain from interface of $In_{0.18}Ga_{0.82}As$ and GaAs. For the 10 nm thickness GaAs, the extra 1 nm of GaAs will not affect the sample identically.

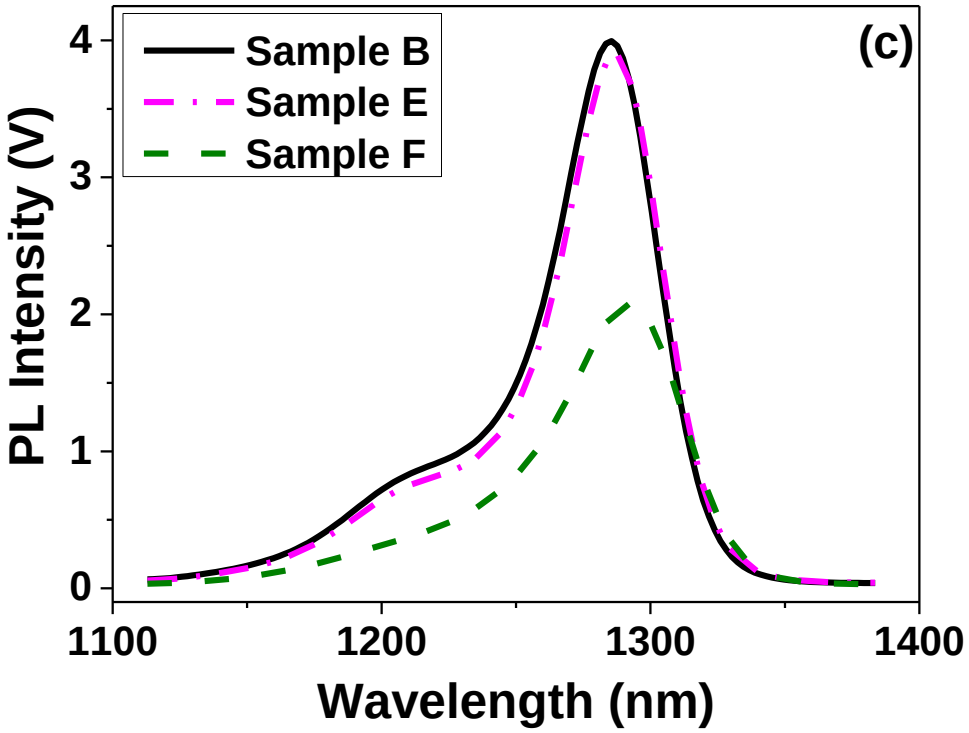

Figure 5.7 Room-temperature PL spectra comparison of GaAs thickness in $In_xGa_{1-x}As$/GaAs SLSs 10 nm (sample B), 9 nm (sample E) and 8 nm (sample F).

As shown in Figure 5.8, sample F has the highest full-width half maximum (FWHM) compare with other 5 samples. The FWHM is calculated by fitting the PL spectrum into two peaks, ground state and excited state. The poor performance on FWHM of sample F is due to QDs growth inhomogenously. The 8 nm of GaAs thickness in InGaAs/GaAs SLSs DFLs affect the QD uniformity negatively. Sample B has the lowest FWHM which is 30.3 meV but sample A, C, D and E are all comparable as well.

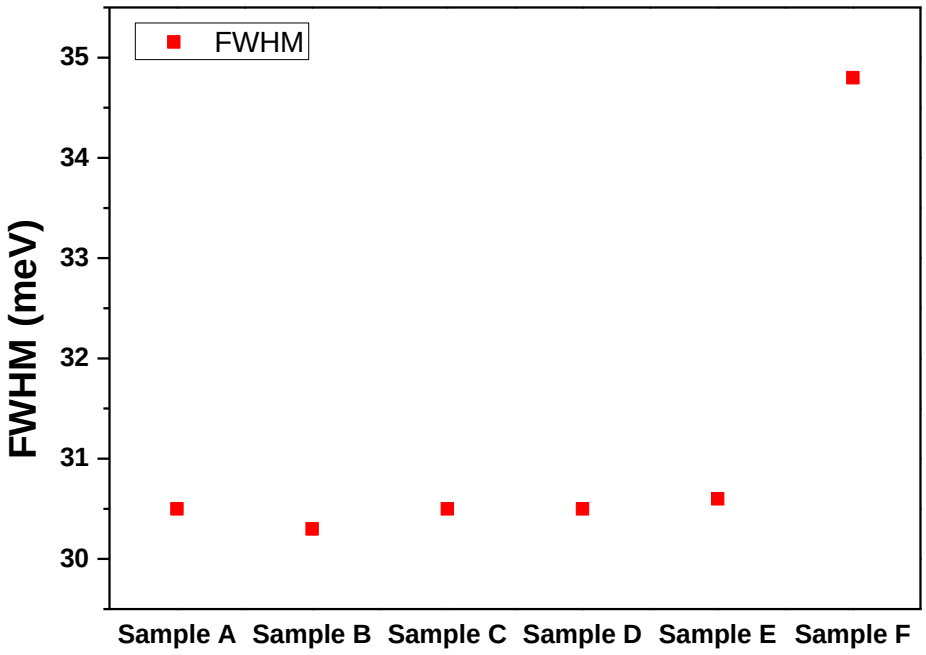

Figure 5.8 Comparison of FWHM for sample A to F.

5.5 Transmission Electron Microscopy Measurements

We have used TEM measurements to examine the crystal quality. Figure 5.9 presents the cross-sectional TEM images of QDs. The QDs have width of around 20 nm and height of around 9 nm due to the InGaAs capping layer. Figure 5.8(b) shows the five layers of InAs/GaAs QDs have visually no threading dislocations go through. Figure 5.10 shows the cross-sectional dark-field and bright-field TEM images of three sets of InGaAs/GaAs SLSs DFLs. The major of threading dislocations were blocked by first set of optimized DFL, and the second and third sets of DFL visually eliminate the rest of threading dislocations. In the bright-field TEM images Figure 5.10(b), huge amount of dislocations at the interface of GaAs/Si however apart of dislocations have been trapped at first 200 nm. Afterwards, we found that dislocations are self-elimination or merged when two dislocations encounter. Moreover, the propagation directions of threading dislocations are bended to parallel with InGaAs/GaAs SLSs when they engage to cross the SLSs. It also shows no dislocations above of the three sets of InGaAs/GaAs SLSs DFLs.

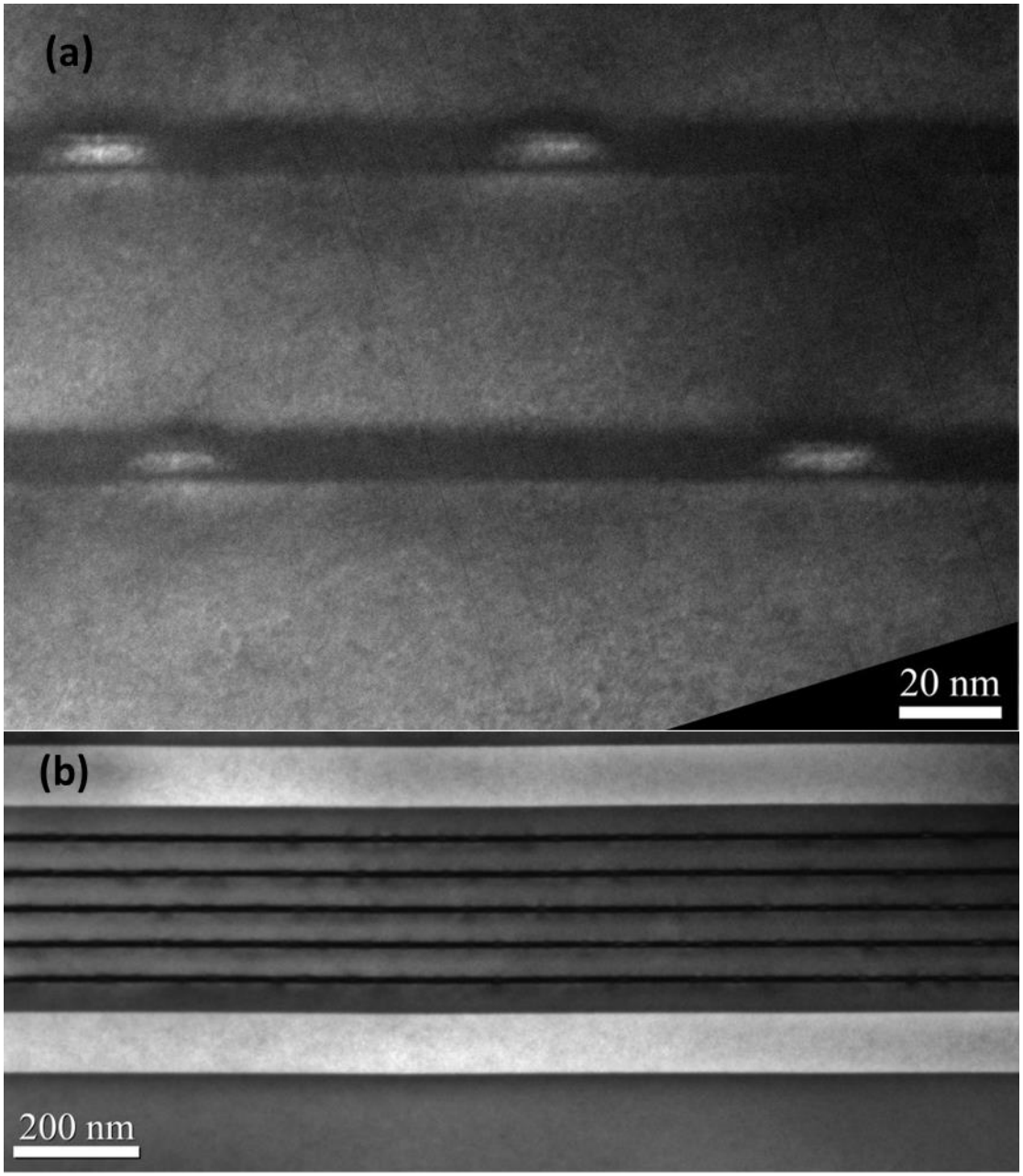

Figure 5.9 Transmission electron microscopy of (a) InAs/GaAs QDs; (b) 5 layers of InAs/GaAs QDs embedded within InGaAs/GaAs quantum well. The TEM image is measured by University of Warwick.

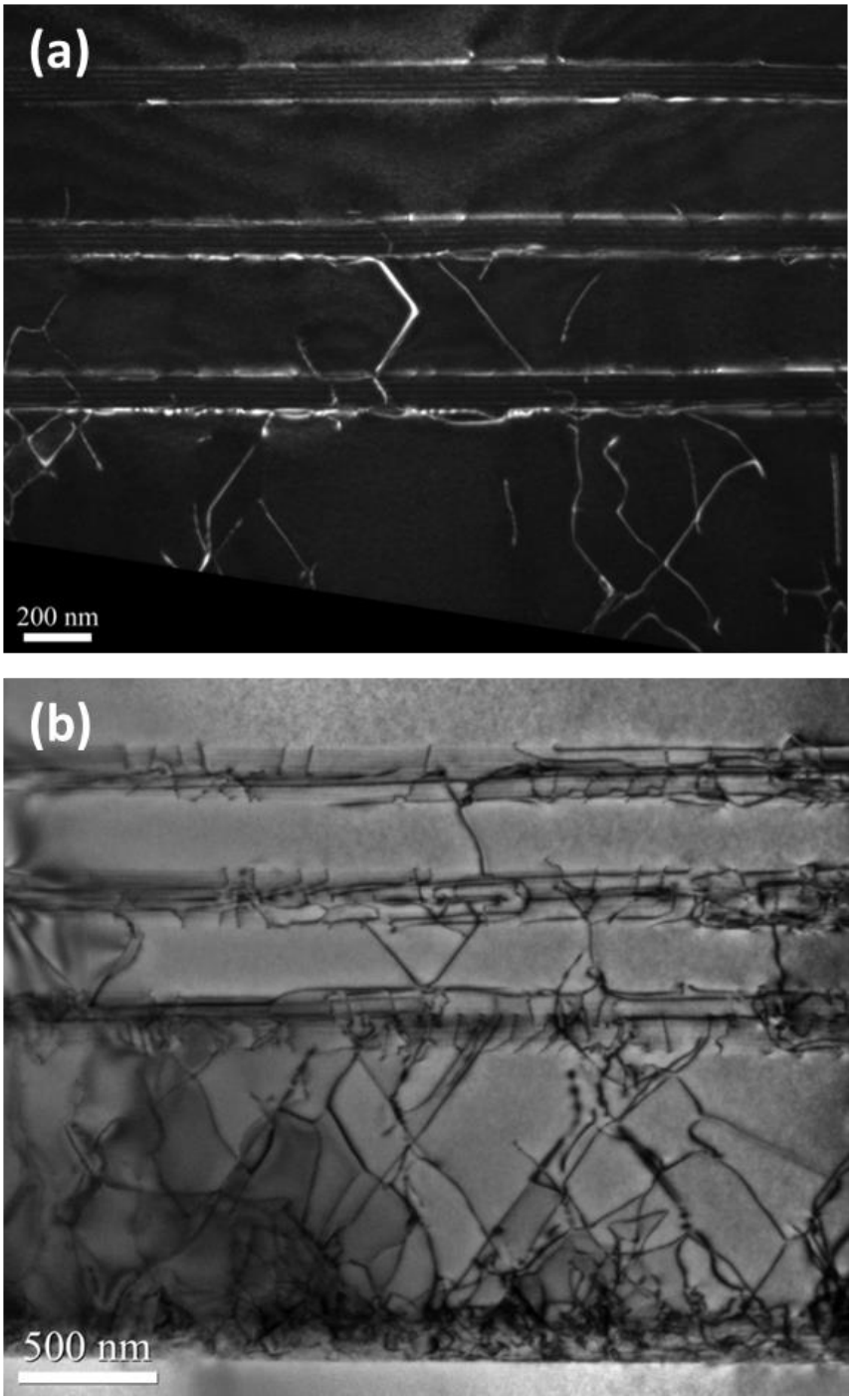

Figure 5.10 (a) dark-field TEM cross-sectioanal TEM iamges of three layers of (b) bright-field TEM cross-sectional Tem images of DFLs on GaAs buffer layer and Si substrate. The TEM image is measured by University of Warwick.

To examine the efficiency of dislocation filtering layers for each type of DFL, we have measured dislocations density above each layer of DFL using TEM measurements. We define

the efficiency of DFL as the fraction of threading dislocations it removes, which can be expressed as [5]

$$Efficiency = 1 - \frac{n(mea)}{n(pre)} \qquad \text{equation 5.1}$$

where $n_{(mea)}$ is the number of dislocations counted just above the DFL and $n_{(pre)}$ is the number of dislocations predicted by the equation of "natural" decrease in ρ_{TD} [6]. The natural decrease in dislocations is based on measurements of dislocations in the GaAs buffer layer on Si substrate. The equation of ρ_{TD} is related to the thickness h, the expression is

$$\rho_{TD} = Ah^{0.5} \qquad \text{equation 5.2}$$

where A is a constant fitted by the counts of threading dislocations at three positions in the GaAs buffer layer: 300, 600 and 900 nm. The efficiencies of each type of DFLs are presented in Fig. 6. The total efficiency of sample A is 92%, significantly lower than sample B's 99%. Samples C and D have total efficiencies of 90% and 91% respectively. At the first layer of DFL, the efficiencies of four samples range from 40% to 50%. After DFL1, samples B, C and D show stronger increase in efficiency compare with the sample A. This is due to the high temperature GaAs spacer layer growth successfully increasing the dislocations motion and hence increasing the opportunities of the elimination of threading dislocations. Therefore, the 18% indium composition and growth method II have been proved to be the most effective in reducing the density of threading dislocations. The reason why sample D has higher total efficiency than sample C is that sample D has higher indium composition of 20% compare with 16% in sample C, which has more strain to stop the threading dislocations from propagating.

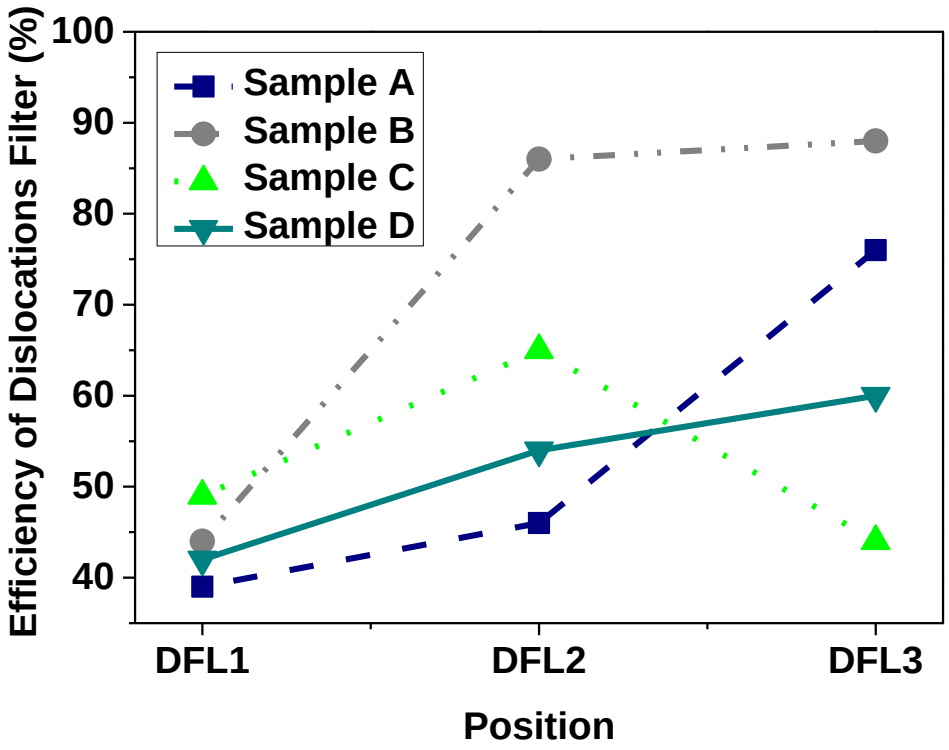

Figure 5. 11 Plot of sample A, B, C and D's efficiency of filtering dislocations at different layer of DFLs.

5.6 Laser Fabrication and Results

To further investigate the effects of $In_xGa_{1-x}As/GaAs$ SLSs DFLs, full laser structures have been grown and processed with different DFLs. The GaAs buffer layer and InAs/GaAs DWELL active region were grown at same condition as previously samples A to F. We have grown two laser samples L1 and L2 that regard to reference and optimised $In_xGa_{1-x}As/GaAs$ SLSs DFLs condition. The reference of $In_xGa_{1-x}As/GaAs$ SLSs DFLs has used growth method I, indium composition 18% and GaAs thickness 10 nm. In contrast, the optimised $In_xGa_{1-x}As/GaAs$ SLSs DFLs have used growth method II, indium composition 18% and GaAs thickness 10 nm The op After 3 sets of DFL, n and p type 1.2 μm thickness of AlGaAs/GaAs cladding layers were grown on the bottom and top of the active region. The GaAs n contact layer was deposited under the n type cladding layer for etch down contacting, and GaAs p contact layer was on the top of devices.

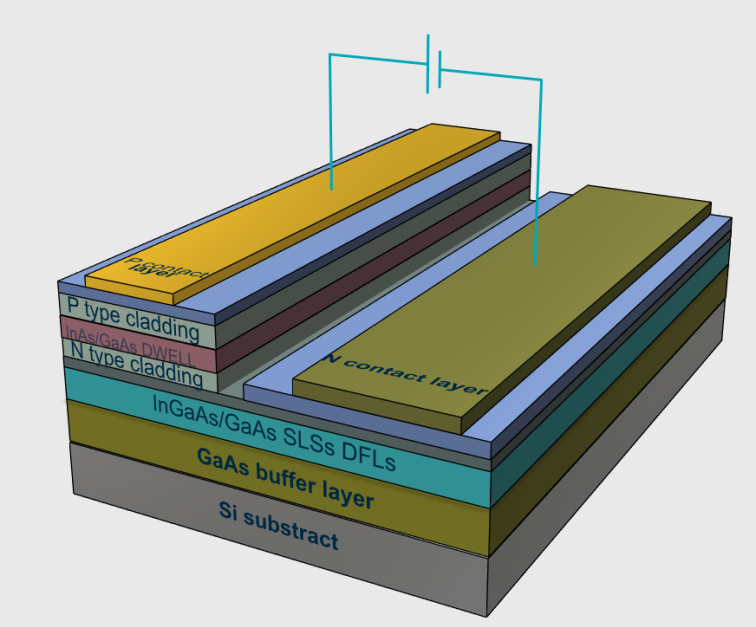

Figure 5.12 Schematic diagram of InAs/GaAs QD laser monolithically grown on Si offcut substrate. The p and n contact layer both face up.

The broad-area laser devices were fabricated as shown in Figure 5.11. 50 μm of width ridges are made by standard lithography and wet etching techniques. We etched down the ridges to 200 nm below the active region which it could improve the carrier confinement. We deposited InGe/Au and Ti/Pt/Au on GaAs n contact and p contact layer respectively. The cavity length of devices is 3-mm length and no facet coating is applied.

Two lasers devices, L1 and L2, have been fabricated, which regards to the reference and optimized DFLs condition, respectively. L1's single facet output power against current density measurements have been presented in Figure 5.13. During the measurements, the laser devices are mounted epi-side up with a sub-mount temperature of 18 ˚C without active cooling. The lasers are electrical pumped by pulsed condition of 1% duty cycle and 1 μs pulse-width. The threshold current density of laser L1 is 174 A/cm^2 at 18 ºC. The maximum operating temperature is 68 ºC.

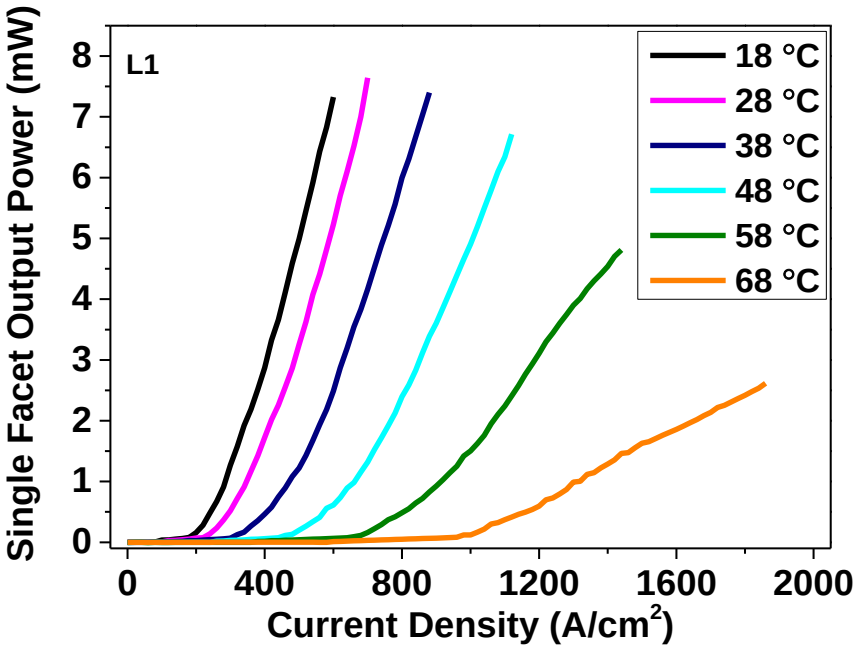

Figure 5.13 Single facet output powers against current density for laser sample L1 under pulsed mode (1% duty cycle and 1µs pulse width)

Laser sample L2 has lower threshold current density compare with L1 as presented in Figure 5.14. At 18 ºC, the threshold current density is 99 A/cm^2. The maximum operating temperature is 88 ºC which is higher than L1. The lasing spectrum of laser sample L2 is presented at Figure 5.15. The laser emission is at 1280 nm which is corresponding to the optimised DFLs condition (sample B).

Figure 5.16 shows the temperature dependence J_{th} of laser sample L1 and L2. L2 shows the stable characteristic temperature T_0, 40.2 K, which is larger than L1, 36.3 K at temperature range 18 to 38 ˚C, 26.3 K at 38 to 68 ˚C. The poor performance of T_0 at higher temperature range is due to the increased ratio of non-radiative recombination centre at high temperature range. L2 shows the better performance on T_0 is due to the lower threading dislocations density compare with L1.

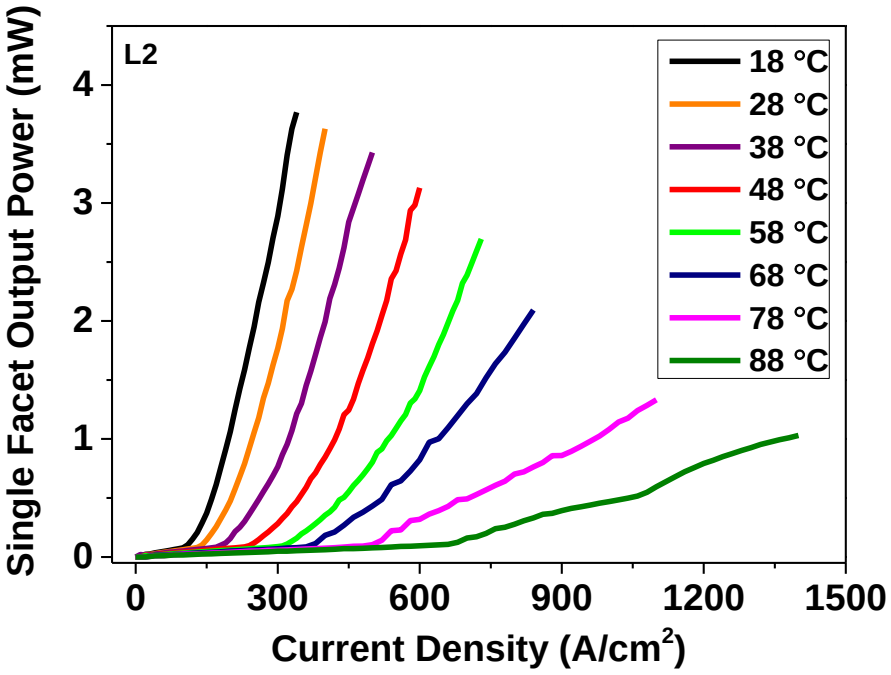

Figure 5.14 Single facet output powers against current density for laser sample L2 under pulsed mode (1% duty cycle and 1μs pulse width)

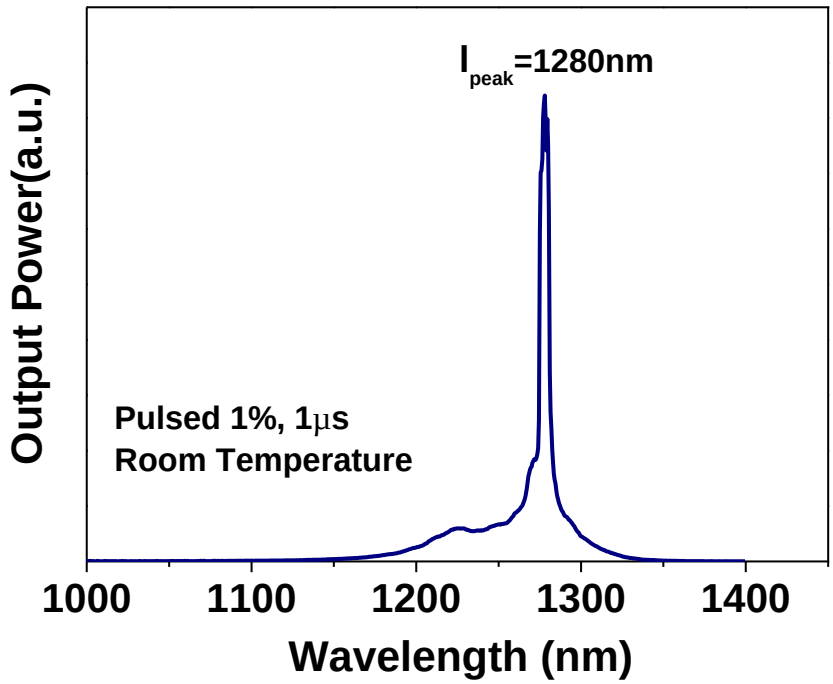

Figure 5.15 Lasing spectrum of sample L2 at room temperature. The emission peak is at 1280 nm with driving current density 105 A/cm^2.

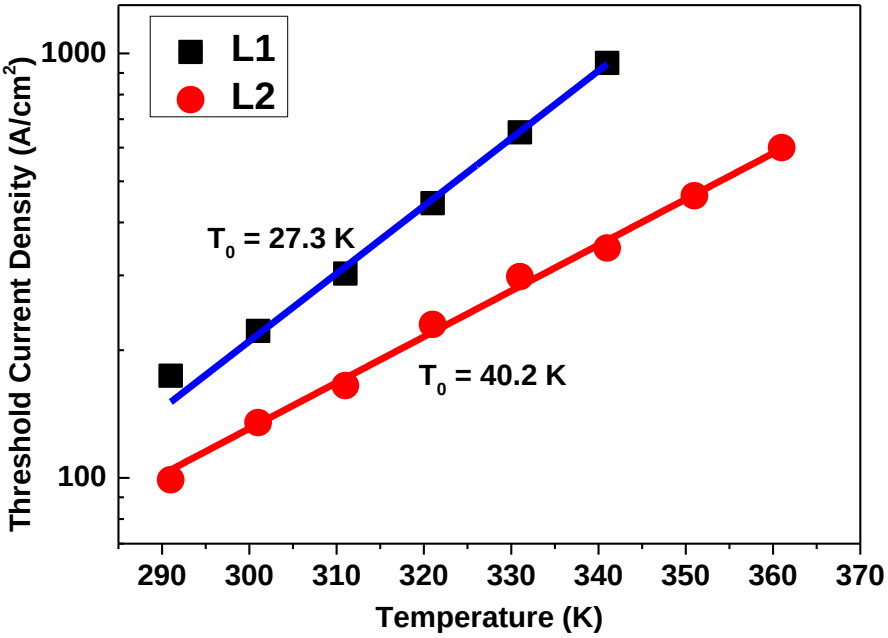

Figure 5.16 Temperature dependence of the threshold current densities under pulse operation of laser sample L1 and L2.

5.7 Conclusion

In conclusion, we have investigated the optimizations of growth of $In_xGa_{1-x}As$/GaAs SLSs DFLs by improving the GaAs spacing layer growth, indium composition and GaAs thickness in $In_xGa_{1-x}As$/GaAs SLSs. The optimizations of DFL are proved by better laser devices performance, which shows growing GaAs spacing layer at high temperature, indium composition 18% and GaAs more than 8 nm in $In_xGa_{1-x}As$/GaAs SLSs are more effective on balancing the strain and blocking threading. The low threshold current density InAs/GaAs QD lasers monolithically grown on Si have been demonstrated by using optimized DFLs. Our studies provide an essential step to improve the InAs/GaAs QDs laser monolithically integrated on Silicon photonics.

Reference

1. Ting Wang, Huiyun Liu, Andrew Lee, Francesca Pozzi, and Alwyn Seeds. "1.3-μm InAs/GaAs quantum-dot lasers monolithically grown on Si substrates." *Optics Express*, vol. 19, no. 12, pp. 11381-11386, 2011

2. Kazuhiko Nozawa, and Yoshiji Horikoshi, "Low threading dislocation density GaAs on Si (100) with InGaAs/GaAs strained-layer superlattice grown by migration-enhanced epitaxy," *Journal of Electronic Materials*, vol. 21, no. 6, 641-645, 1992
3. Liu, H. Y., M. Hopkinson, C. N. Harrison, M. J. Steer, R. Frith, I. R. Sellers, D. J. Mowbray, and M. S. Skolnick, "Optimizing the growth of 1.3 μm InAs/InGaAs dots-in-a-well structure," *Journal of Applied Physics*, vol. 93, no. 5, pp. 2931-2936, 2003
4. H. Y. Liu, I. R. Sellers, T. J. Badcock, D. J. Mowbray, M. S. Skolnick, K. M. Groom, M. Gutierrez, M. Hopkinson, J. S. Ng, J. P. R. David and R. Beanland, "Improved performance of 1.3 mum multilayer InAs quantum-dot lasers using a high-growth-temperature GaAs spacer layer," *Applied Physics Letters*, vol. 85 pp. 704, 2004
5. I. George, F. Becagli, H. Y. Liu, J. Wu, M. Tang, and R. Beanland, "Defect filters in GaAs on Si," *Semiconductor Science and Technology*, vol. 30, no. 11, pp. 114004, 2015
6. A. E. Romanov, W. Pompe, G. Beltz, and J. S. Speck, "Modeling of Threading Dislocation Density Reduction in Heteroepitaxial Layers I. Geometry and Crystallography", *Physica Ptatus Polidi (b)*, vol. 198, no. 2, pp. 599-613, 1996

Chapter 6

Conclusion and Future Work

6.1 Summary of Present Work

In order to improve the performance of InAs/GaAs QDs device based on Si substrates with MBE system growth, we have implemented InAlAs/GaAs SLSs DFL instead of InGaAs/GaAs SLSs DFL, which has been used to demonstrate laser devices with 625 A/cm^2 and maximum operation temperature 45 °C by T. Wang [1]. The new type of DFL significantly reduced the threading dislocation density from ~10^{10} to ~10^6 cm^{-2} based on the measurement of transmission electron microscopy and etch pit density. So the performance of laser diode has been improved with high operation temperature (maximum 85 °C) and low threshold current density (194 A/cm^2) under pulsed mode operation. Before we fabricate the laser device, we compared the photoluminescent intensity, TEM cross-section measurements and AFM surface morphology of samples which grown at same condition but with InAs QDs DFL, InGaAs SML QDs, InAlAs/GaAs SLSs DFL and InGaAs/GaAs SLSs DFL separately. The results shown the InAlAs/GaAs SLSs DFL is an efficient type of DFL in QDs lasers grown on Si substrate. The InAs/GaAs QDs lasers grown on Si substrate are emitting at 1.27 μm at room temperature with output power of around 77 mW at pulsed mode.

The first InAs/GaAs SLDs on Si substrate have been grown and fabricated based on the more random quantum dots size distribution. The great result shows the amplifier potential of SLD on Si for OEIC purpose. The SLDs emits a close-to-Gaussian spectrum around 114-nm bandwidth, with centre at 1255 nm. The measured maximum output power is 2.6 mW at room temperature. To achieve the superluminescense, the devices have been fabricated as two

section, 2-mm length gain and 1-mm length absorption. The shorter cavity length introduces more loss during on the facet and the photons emit through the facet are absorbed.

The InGaAs/GaAs SLSs DFLs optimisations are also carried out in chapter 5. By improving the GaAs spacer layer growth between each set of DFL, the crystal quality is significantly improved. Also the well-balance between indium composition and blocking threading dislocations improve the QDs density, PL emission and efficiency of blocking threading dislocations. The 9 nm and 10 nm of GaAs thickness in InGaAs/GaAs SLSs can improve the relaxation of strain from InGaAs/GaAs SLSs. The optimised DFLs have been applied in laser device which compare with reference laser. The optimised DFLs provide lower threshold current density, higher maximum operating temperature and characteristic temperature into laser.

6.2 Future Work

Although we have successfully demonstrated the low threshold current density for InAs/GaAs quantum dot (QD) lasers and first InAs/GaAs QD superluminescent diode (SLD), which are both monolithically grown on Si substrate by molecular beam epitaxy system, the continues-wave operation is keen to be achieved on Si baser devices especially for 1.3 μm InAs//GaAs QDs laser and SLD. The difficulties on Si platform rather than other III–V materials platform for instance InP, GaAs and GaN, are major due to the thermal cracker caused by the different of thermal expansion coefficient of Si and other III–V material. The ideal solution could be introducing thermal cycle annealing on GaAs buffer layer or use other type of buffer layer like AlAs and GaSb.

InAs/GaAs QDs also have the potential to implement in the longer wavelength light emitting devices (1.5 μm, 2 μm etc.) for telecommunication proposes. To achieve the mid inferred emitting, InAs/GaAs QDs need to be grown on more strain relaxed layer which GaAsSb metamorphic layer could help. Si platform is capable with mid-infrared emitting devices and molecular beam epitaxy has the function to deposit GaAsSb metamorphic layer on GaAs which have been achieved by H. Liu [2] and cap InAs/GaAs QDs with GaAsSb thin layer to extend the QDs emitting wavelength to 1.6 μm also demonstrated by H. Liu [3]. The next step of 1.5 μm wavelength light emitting diode is to immigrate on Si platform from GaAs substrate which could refer to the established technique GaAs grown on Si substrate. The difficulties of longer

wavelength InAs/GaAs QDs on Si platform are similar to 1.3 μm wavelength; the threading dislocations propagating from the GaAs/Si interface destroy the performance of light emitting devices. Also the strain from the lattice mismatch between GaAs and Si could affect the InAs/GaAs QDs size so that the wavelength of photon emitting is dedicated.

In order to significantly reduce the dislocation density from 10^6 to 10^5 cm $^{-2}$ or even lower on Si substrate, same lattice constant material as Si is considered in work. The growth of GaP on Si substrate by MBE system has been achieved by T. J. Grassman [4], which brings the possible of immigration of GaP based light emitting device to Si based. Due to the similar lattice constant between GaP and Si, the GaP buffer layer could have better crystal quality in fewer dislocation and defects. However the major issues of growth of GaP on Si are P atoms could able to destroy the surface of Si substrate. With T. J. Grassman's method of GaP grown on Si (001) has no APD/MF/ST observed based on his report, which inspired and motivated us to work device on GaP/Si.

As we have improved the Si based laser, the optical circuit integration on Si or Si/Ge substrate is keen to achieve. Until now, bonding technique and CMOS has occurred most of results on Si substrate and their results are impressing: AlGaInAs quantum well laser bonding on Silicon-on-insulator (SOI) emitting at 1538 nm with optical pumped [5]; an integration of laser and photodetector with InP/InGaAsP thin film structure bonding on SOI waveguide has been reported by G. Roleken [6]; A superluminescent LED based on InP bonding with silicon waveguide achieved by A. De Groote [7].

Although there are tons of reports on bonding technique, QDs laser monolithically growth on Si integration still has the opportunity to explore its own area, because the high performance of monolithically grown QD lasers has lower threshold current density and higher operation temperature than bonding-lasers [8]. The issues of QDs lasers grown on Si are due to the difficulties of selective growth on Si substrate, SiN or SOI. Double heterosturecture laser AlGaAs/GaAs has been successfully selective growth on Si with SiN defined strip windows [9], which inspired us the possibility of QDs laser selective growth on Si.

As we presented in Figure 6.1, the next project of our growth could be using SiN or SiO_2 waveguide as pattern on the substrate. The first step is to prepare the sample with 2 μm SiO_2

layer on the Si substrate and dioxide the ridge for the laser growth. Then we can grow the GaAs buffer layer and the following laser active region within the SiO_2 waveguide.

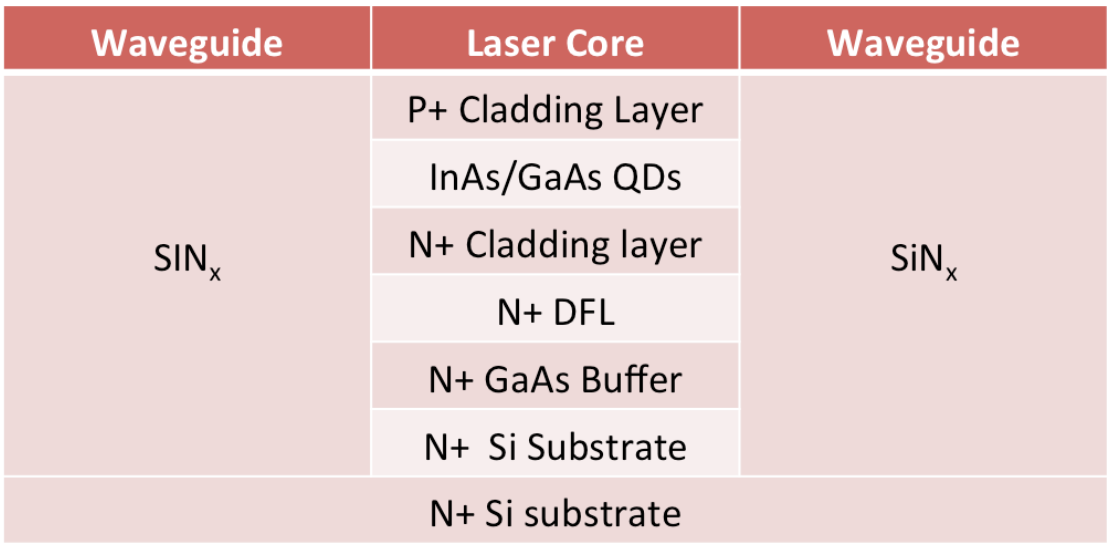

Figure 6.1 Cross-section schematic diagram of InAs/GaAs QDs grow on Si substrate with pattern of SiN_x waveguide.

6.3 Growth Plan

Based on the Grassman and Brenner's study, GaP grown on Si substrate is workable. To grow GaP on Si substrate, migration enhanced epitaxy (MEE) technique needs to be used as the first 20 layers of GaP with Ga prelayer. After the GaP buffer layer, defect filter layer (DFL) will be grown with three repeats because the defects density is lower on GaP buffer layer than GaAs buffer layer. After the growth of three repeats of DFL, 1.3 μm AlGaAs/GaAs cladding layer and 5 layers of InAs/GaAs QDs are grown at optimised condition. The 200 nm GaAs contact layer are grown on the bottom and top of AlGaAs/GaAs cladding layer for etch down propose. The device will be processed as 50-μm ridge and 3-mm cavity length. The shorter ridge is also worth to try.

Reference

1. T. Wang, H. Liu, A. Lee, F. Pozzi, and A. Seeds, "1.3-μm InAs/GaAs quantum-dot lasers monolithically grown on Si substrates", *Optics Express*, vol. 19, no. 12, pp. 11381–11386, 2011

2. H. Y. Liu, Y. Qiu, C. Y. Jin, T. Walther, A. G. Cullis, "1.55μm InAs quantum dots grown on a GaAs substrate using a GaAsSb metamorphic buffer layer", *Applied Physics Letters*, vol. 92, pp. 111906, 2008
3. H. Y. Liu, M. J. Steer, T. J. Badcock, D. J. Mowbray, M. S. Skolnick, F. Suarez, J. S. Ng, M. Hopkinson,and J. P.R. David, "Room-temperature 1.6 μ m light emission from InAs/GaAs quantum dots with a thin GaAsSb cap layer", *Journal of Applied Physics*, vol. 99, pp. 046104, 2006
4. T. J. Grassman, M. R. Brenner, S. Rajagopalan, R. Unocic, R. Dehoff, M. Mills, H. Fraser, and S. A. Ringe, "Control and elimination of nucleation-related defects in GaP/Si(001) heteroepitaxy", *Applied Physics Letters*, vol. 94, pp.232106, 2009
5. Alexander W. Fang, Hyundai Park, Oded Cohen, Richard Jones, Mario J. Paniccia, John E. Bowers, "Electrically pumped hybrid AlGaInAs-silicon evanescent laser", *Optics Express*, vol. 13, no. 23, pp. 9460-9464, 2005
6. G. Roelkens, D. Van Thourhout, R. Baets, R. Nötzel and M. Smit, "Laser emission and photodetection in an InP/InGaAsP layer integrated on and coupled to a Silicon-on-Insulator waveguide circuit", *Optics Express*, vol.14, no. 18, pp. 8154-8159, 2006
7. A. De Groote, J. D. Peters, M. L. Davenport, M. J. R. Heck, R. Baets, G. Roelkens and J. E. Bowers, "Heterogeneously integrated III–V-on-silicon multibandgap superluminescent light-emitting diode with 290 nm optical bandwidth", *Optics Letters*, vol. 39, no. 16, pp. 4784-4787, 2014
8. Mingchu Tang, Siming Chen, Jiang Wu, Qi Jiang, Vitaliy G. Dorogan, Mourad Benamara, Yuriy I. Mazur, Gregory J. Salamo, Alwyn Seeds, Huiyun Liu, "1.3-μm InAs/GaAs quantum-dot lasers monolithically grown on Si substrates using InAlAs/GaAs defect filter layers", *Optics Express*, vol. 22, no. 10, pp. 11528-11535, 2014
9. Henry P. Lee, Xiaoming Liu, Shyh Wang, "Double-heterostructure GaAs/AlGaAs lasers on Si substrates with reduced threshold current and built‐in index guiding by selective-area molecular beam epitaxy", *Applied Physics Letters*, vol. 56, no. 11, pp, 1014, 1990